Faculty of Physics and Astronomy

University of Heidelberg

Diploma thesis

in Physics

submitted by

Bastian Jungnitsch

born in Heidelberg

2008

Negative Refraction in Atomic Two-Component Media

This diploma thesis has been carried out by Bastian Jungnitsch
at the Max-Planck-Institute for Nuclear Physics
under the supervision of
Prof. Christoph H. Keitel

Negative Brechung in atomaren Zwei-Komponenten-Systemen: In der vorliegenden Arbeit soll die Realisierungsmöglichkeit negativer Brechung bei optischen Wellenlängen und geringer Absorption in Gasen, die aus zwei verschiedenen Atomsorten bestehen, untersucht werden. Im Vergleich zu einkomponentigen Systemen erhoffen wir uns davon, dass durch die weniger strengen Voraussetzungen, die erfüllt werden müssen, mögliche Atome für eine experimentelle Realisierung leichter gefunden werden können. In Zwei-Komponenten-Systemen trägt je eine Atomsorte die elektrische bzw. die magnetische Antwort bei. Um einen negativen Brechungsindex zu erhalten, müssen beide Antworten groß sein. Daher optimieren wir die magnetische Suszeptibilität, die typischerweise deutlich kleiner als die elektrische Suszeptibilität ist, in verschiedenen Systemen. Weiterhin untersuchen wir einen Mechanismus, der die magnetische Antwort um einen Faktor α^{-1}, der inversen Feinstrukturkonstante, verstärkt und in sogenannten Closed-Loop-Systemen auftritt. Closed-Loop-Konfigurationen sind dadurch gekennzeichnet, dass die koppelnden Probe- und Kontrollfelder im Levelschema eine geschlossene Schleife bilden. Wir stellen fest, dass die Verstärkung auftritt, da die elektrische Komponente des Probefeldes in den magnetischen Probeübergang streut. Unter Verwendung der bisherigen Ergebnisse berechnen wir dann den Brechungsindex für verschiedene Kombinationen realistischer Levelschemata und gehen auf auftretende Instabilitäten des Probefeldes ein. Wir erhalten für zwei verschiedene Systeme einen Brechungsindex von $n = -6.4$ bzw. $n = -3.7$ bei verschwindender Absorption.

Negative Refraction in Atomic Two-Component Media: In the present thesis we study the feasibility of negative refraction at optical wavelengths and low absorption in gases consisting of two species of atoms. Compared to a single-component system, we expect it to be easier to find candidates for an experimental realization due to less stringent conditions that must be met. The two involved species contribute the electric and the magnetic response, respectively. To obtain a negative refractive index, both responses must be large. Therefore, we optimize the magnetic susceptibility, which typically is considerably smaller than the electric susceptibility, in different systems. Moreover, we investigate a mechanism in so-called closed-loop systems that enhances the magnetic response by a factor of α^{-1}, the inverse fine structure constant. Closed-loop configurations are characterized by the fact that the coupling control and probe fields build up a closed interaction loop in the level scheme. We find that the enhancement occurs, as the electric probe field component scatters into the magnetic probe transition. Using the previous results, we calculate the refractive index for several combinations of two realistic level schemes and address the occurring instabilities of the probe field. We obtain a refractive index of $n = -6.4$ and $n = -3.7$, respectively, at vanishing absorption for two different systems.

During this diploma thesis, a paper was submitted to Physical Review A. It can be found under

> B. Jungnitsch and J. Evers, "Magnetic response enhancement via electrically induced magnetic moments", arXiv:0804.3552

Contents

Chapter 1

Introduction

Refraction of light is one of the physical phenomena that we encounter as part of our everyday life. From glasses to microscopes, from mirages to rainbows, refraction can be found everywhere. Due to its accessible nature, refraction was investigated and explained scientifically in the course of the development of one of the very first branches of physics: geometrical optics.

As one of the most fundamental phenomena of this field, refraction can be described by the index of refraction of the involved materials. These indices — or, more precisely, their real parts — are given by the ratio of the speed of light in vacuum and in the respective material. The law of diffraction which is based on these quantities is commonly attributed to Willebrord Snellius. After some preparatory work by others, he derived the well-known relation $sin(\theta_1)/sin(\theta_2) = n_2/n_1$ between the ratio of the angle of incidence θ_1 and the angle of refraction θ_2 and the indices of refraction n_1 and n_2 of the two involved media at whose borderline the refraction occurs. The work of Snellius is embedded in a vivid time of discovery in geometrical optics and has to be seen in the context of works by Johannes Kepler, René Descartes, Christiaan Huygens, Isaac Newton, Galileo Galilei and Johann Wolfgang von Goethe. In later centuries, geometrical optics gave birth to important branches of physics, such as electrodynamics and astronomy.

In the latter, geometrical optics played a particularly important role in the development of lenses. Whereas glasses have refractive indices in the range of $n = 1...2$, natural materials in general have indices mainly between $n = 1$ and $n = 4$. However, in 1968 scientists realized that a negative index of refraction — or, more precisely, a negative real part of the index of refraction — does not violate any physical laws and therefore is possible, in principle, giving rise to many astonishing and counter-intuitive effects. At this time, Victor Veselago wrote his paper *"The Electrodynamics of Substances with Simultaneously Negative Values of μ and ε"* [1] and opened the road to an exciting new phenomenon: negative refraction.

Due to the lack of natural media that refract negatively, the topic was first neglected some time, until the development of modern photonics and quantum optics lead to the insight that negative refraction is feasible in reality. A first climax was the realization of negatively refracting metamaterials [2, 3] — building on a proposal by Pendry [4] — and negative refraction in photonic crystals [5]. Nowadays, metamaterials are a common tool to demonstrate negative refraction [6, 7, 8, 9]. These artificially built materials consist of tiny LCR circuits that are smaller than the wavelength of the used light, which means that the light sees a homogeneous medium. The LCR circuits can be designed appropriately in order to achieve suitable electric and magnetic responses. Photonic crystals, in contrast, contain structures that have dimensions of the same order as the wavelength of the light. Their permittivity and/or permeability change periodically in space, thus manipulating the speed of light through diffraction.

Also, theoretical and experimental works suggested a variety of applications for the new phenomenon: The perfect lens proposed by Pendry [10] allows for an, in principle, arbitrarily large resolution. It can be build of a slab with an index of refraction of $n = -1$ which cancels the decay of evanescent waves, thus overcoming the physical mechanism that is responsible for the diffraction limit of half the wavelength of the used light. Works by Pendry, Schurig and Smith [11] and Leonhard [12] about the realization of an electromagnetic cloak were followed by an experimental demonstration taking use of negative refraction [13] in which a cylinder was made nearly invisible at a microwave frequency. Negatively refracting materials would help to build antennas shorter than a quarter of the emitted wavelength and electromagnetic wave guides that work at dimensions smaller than the transmitted wavelength. Negative refraction can reduce reflections on surfaces and help to store information optically and at a high density.

What stands behind these interesting applications are the counter-intuitive, surprising properties of negative refraction: As Veselago [1] argues with the help of the two vectorial Maxwell equations, in materials with a negative permittivity ε and a negative permeability μ (for real ε and μ), the wave vector $\vec{k} = n\frac{\omega}{c}\frac{\vec{S}}{|\vec{S}|}$ of the incident light and $\vec{E}$ and $\vec{H}$ form a left-handed system. Here, $\vec{E}$ and $\vec{H}$ are the electric and magnetic field, ω their frequency, c the vacuum speed of light and n the index of refraction. However, the Poynting vector $\vec{S} = \vec{E} \times \vec{H}$ of the incident beam and $\vec{E}$ and $\vec{H}$ form a right-handed system due to the definition of $\vec{S}$. Therefore, interestingly, the energy flow — described by $\vec{S}$ — and the phase motion — as given by $\vec{k}$ — point in opposite directions. Due to $\vec{k} = n\frac{\omega}{c}\frac{\vec{S}}{|\vec{S}|}$, we have to assign a negative value to the index of refraction n.

The fact that $\vec{k}$, $\vec{E}$ and $\vec{H}$ form a left-handed system in negatively refracting materials, whereas in positively refracting media, $\vec{k}$, $\vec{E}$ and $\vec{H}$ build a right-handed system, motivated the name "left-handed materials" in case of a negative refractive index.

Up to date, negative refraction has been realized at both microwave [2, 3, 9] and optical frequencies [14]. However, the production process of metamaterials that work at optical frequencies is a complex technological challenge, due to the required subwavelength feature size of the metamaterials. Also, the losses in such metamaterials are given by the imaginary part of the index of refraction. Since metamaterials are typically passive systems and work close to an electromagnetic resonance, the imaginary part is positive and of the same size as the real part. Thus, the occurring absorption is substantial. However, large losses are a disadvantage when it comes to measuring negative refraction in an experiment and also for the mentioned applications, such as the perfect lens by Pendry.

Therefore, in the recent past, one has also turned to atomic gases for the realization of negative refraction [15, 16, 17, 18]. These are naturally three-dimensional media, in contrast to metamaterials which are often produced in two-dimensional layers. Atomic gases commonly have several electric dipole transitions at optical wavelengths. Also, magnetic dipole transitions at optical frequencies can be found. Moreover, one can use lasers to produce control fields in the atomic gas that can be used to tailor the shape of the response and thus the ratio of real and imaginary part of the refractive index.

However, the relative permeability μ_r and the relative permittivity ε_r are given by

$$\varepsilon_r = \tilde{\chi}_e + 1 \,, \tag{1.1a}$$

$$\mu_r = \tilde{\chi}_m + 1 \,, \tag{1.1b}$$

in terms of the magnetic and the electric susceptibility $\tilde{\chi}_m$ and $\tilde{\chi}_e$ in Fourier space. The susceptibilities, in turn, quantify the magnetic and electric response. Normally, they are of the relative order of magnitude of $\tilde{\chi}_m/\tilde{\chi}_e \approx \alpha^2 \approx \frac{1}{137^2}$. Therefore the magnetic response is suppressed.

Permeability and permittivity contribute to the index of refraction according to [19]

$$n^2 = \varepsilon_r \mu_r \,. \tag{1.2}$$

Since Veselago deduced a negative index of refraction for $\mu_r < 0$ and $\varepsilon_r < 0$ and due to Eqs. (1.1), it is desirable to have both a negative magnetic and electric susceptibility of a large absolute value. This means that we need a large magnetic response. Also, until now, we have only focused on the real part of the, in fact, complex susceptibilities, permittivities and permeabilities. However, as already mentioned, the material should also be as little absorbing as possible. This implies a small imaginary part of the refractive index.

Furthermore, to prepare the road for an experimental realization of negative refraction in atomic gases, one has to find possible candidate atoms. In previous works, the

metastable noble gases Neon, Krypton, Xenon [18] and rare-earths like Dysprosium [17] have been proposed. However, the difficulty in finding suitable candidates is the fact that these candidate atoms must have an electric and a magnetic transition at approximately the same frequency: The resonances should not be further apart from each other than roughly the natural linewidth to provide non-zero responses.

In this thesis, we therefore examine a method which possibly allows us to meet this restrictive requirement much easier. We take two different species of atoms A and B, one of which couples to the magnetic component of the incident probe field, the other one of which couples to the electric component. Therefore, the electrically coupling species yields the electric response, while the magnetically coupling component is responsible for the magnetic response.

Moreover, if we consider media that consist of two components, we can optimize their respective responses independently to achieve negative refraction with low losses. Furthermore, there is also the hope that if the magnetic probe field component only couples to one species, say species A, we can use control fields that interact with atoms of species A in a special way to obtain a larger magnetic response. These control fields are applied to the medium to prepare it and to manipulate its responses in a suitable way. We can apply them in such a way that the control fields build up an interaction loop in the level scheme of medium A together with the magnetic probe field component. This creates a so-called closed-loop scheme. The interaction loop does not contain the electric probe field component, but only control fields. This is in contrast to other schemes in single-component media [18, 17]. As control fields are much stronger than probe fields, one possibly obtains a larger magnetic response in such a closed-loop scheme that only couples to the magnetic probe field component.

1.1 Structure and results of this thesis

For these reasons, we examine the feasibility of negative refraction in atomic two-component media. To do so, this work is divided into the following parts:

In Sec. 2, we study how one can tailor the magnetic response in three-level schemes with the help of incoherent pumping and coherent control fields, in order to optimize the response such that it can be used for negative refraction at low absorption. However, it is possible to optimize permittivity and permeability towards different values which are all candidates for negative refraction. We will choose the way that already Veselago opted for [1] and optimize towards a small imaginary part and a strongly negative real part of both the permittivity and the permeability. This has been done, e.g., by Fleischhauer et al. in [20] for the electric response, but not yet for the magnetic response.

We begin with the theoretical preparation in Sec. 2.1. Thereafter, we consider concrete systems: As an introductory example, we start with the simplest system, the two-level system. However, due to its simplicity, it has two advantages when it comes to negative refraction: First, it might be easier to find two-level systems in reality to use them for an experimental realization of negative refraction in atomic two-component media. Secondly, it will turn out that, for a certain parameter range, media formed by three-level systems are instable and a physical interpretation of the index of refraction in Fourier space is not valid. Two-level systems do not exhibit these instabilities for any set of parameters. These instabilities are closely related to the topic of branch points and will be discussed in Sec. 4.1.4.

Then, as main part of Sec. 2, we will discuss the magnetic responses of three-level systems in different configurations. Namely, these are the so-called upper microwave scheme, the lower microwave scheme, both of which show a ladder configuration of the applied fields, and the lambda system, which is typically used for electromagnetically induced transparency (EIT). We present optimized susceptibilities of all these systems.

In Sec. 3, we will then turn to another aspect of the magnetic response. Since the magnetic response usually is considerably smaller than the electric response, as mentioned by a factor of α^{-2}, we investigate a scheme suggested by Oktel and Müstecaplıoğlu to enhance the magnetic response. They observed an enhancement of the magnetic response by a factor of α^{-1} at a single frequency in a similar way as, in subsequent work [17, 18], others did at all frequencies. A deeper understanding of the mechanism responsible for this enhancement is desirable to take advantage of it. Therefore, we compare two systems, one of which includes a closed interaction loop of coupling and probe fields. This closed-loop system shows the enhancement, while the other, similar system without a closed loop does not. In this way, we can identify the mechanism leading to the enhancement [21]. We find that a scattering process of the electric probe field component into the magnetic probe field component accounts for an enhancement of a factor of α^{-1}. This opens the possibility for further enhancement beyond a factor of α^{-1}.

Finally, we use the closed-loop system of Sec. 3 in a slightly different configuration and optimize its response in Sec. 3.6, analogously to Sec. 2.3.

In Sec. 4, we combine our previous results to investigate several combinations of two systems with respect to the occurrence of negative refraction. To this end, we briefly have to address the issue of how to combine the magnetic and electric response of two different components into the index of refraction (Sec. 4.1.1). Also, Eq. (1.2) has the two solutions

$$n = \pm\sqrt{\varepsilon_r \mu_r}\,. \tag{1.3}$$

Consequently, if we want to calculate the index of refraction, we have to pick the relevant solution of these two and thus the right sign. In Sec. 4.1.2, we give two algorithms to solve this problem. However, applying these algorithms, we encounter continuity problems that will turn out to be related to the occurrence of so-called branch points of the refractive index that meet particular conditions. These branch points are closely connected to the question of stability of the two media and will be investigated in Sec. 4.1.4.

Finally, we calculate the index of refraction for several combinations of configurations in Sec. 4.2 using the optimized susceptibilities of Secs. 2 and 3.6. In a combination of a pair of two-level systems, we obtain negative refraction. For a particular difference between magnetic and electric transition frequency, we reach values of $FOM \approx 8$. Here, FOM denotes the figure of merit which is defined as $FOM = |\mathrm{Re}(n)/\mathrm{Im}(n)|$. For that, the particle densities for each of the two species must be $N_e = N_m = 10^{21}\, m^{-3}$.

Compared to this, previous works that use media consisting of one single species of atoms needed densities of approximately $N \approx 10^{22}...10^{23}\, m^{-3}$ [17, 18].

For a combination of upper microwave (magnetic species) and two-level system (electric species), we obtain instabilities for the optimized parameters of Sec. 2.3.1. However, for other parameters, namely for a nitrogen-like upper microwave system, we find two frequencies of vanishing absorption at negative refraction, with refractive indices of $n = -3.7$ and $n = -2.0$. For that, the particle density for the magnetic species must be $N_m = 10^{23}\, m^{-3}$ and the density for the electric species $N_e = 10^{21}\, m^{-3}$.

Finally, we consider a combination of a magnetically coupling closed-loop system of Sec. 3.6 and an electrically coupling two-level system. We find a set of parameters of a stable system for which we obtain zero absorption at two different frequencies of negative refraction and thus, the FOM diverges. While the imaginary part is zero due to the vanishing absorption, the index of refraction reaches $n = -6.4$ and $n = -2.5$. For this, the particle densities have to be $N_e = 1.5 \cdot 10^{20}\, m^{-3}$ and $N_m = 10^{23}\, m^{-3}$ for the two different atomic components. This system seems to be more suitable for an experiment than the upper microwave system due to a real part of a stronger negative value at the point of zero absorption.

In Sec. 5, we summarize our results and give an outlook on future tasks in the field of negative refraction in atomic media. In doing so, we also suggest possible candidates for an experimental realization.

1.2 Notation remarks

In the following, we will use the following rules for the notation:

- For indices that cover different ranges of values, different letters will be used.
- Summation indices that refer to different levels will be named with Roman letters. Summation indices that refer to different transitions will be denoted by Greek letters. E.g., ϱ_{ij} refers to the density matrix element which belongs to the transition between *levels* $|i\rangle \rightarrow |j\rangle$, whereas $\sum_{\alpha=1}^{3}$ sums over three *transitions*.
- Also, all formulas will be given in SI units. Therefore, the vacuum permeability [permittivity] μ_0 [ε_0] is not unity. Thus, we have to distinguish between *relative* permeability [permittivity] μ_r [ε_r] and *absolute* permeability [permittivity] μ [ε], which can be obtained by multiplying the relative quantities with the vacuum permeability [permittivity] μ_0 [ε_0]. However, for simplicity, we will call ε_r and μ_r permittivity and permeability in the following, leaving out the term "relative".

Chapter 2

Tailoring the magnetic response

To achieve negative refraction in a two-component medium, we proceed as follows. The medium that consists of two species of atoms is prepared by electromagnetic control fields, i.e. by possibly strong lasers that we shine onto the gas. Then, we probe the properties of the medium, in particular the refractive index, by another, weak probe laser. One species of atoms will couple to the magnetic component of this probe field, the other one to the electric component. Thus, the magnetically coupling species will cause a magnetic response and the electrically coupling species an electric response. These responses are described by magnetic and electric susceptibility, respectively, or the (relative) permittivity ε_r and permeability μ_r which are connected to the susceptibilities by Eqs. (1.1) (see also [19]).

It is possible to have a single species of atoms that couples to both the magnetic and the electric component. This can also lead to negative refraction as proposed by Pendry [22]. In such a case so-called chirality terms occur that describe the electric response to the magnetic field and vice versa. However, this has been done in [17, 18] and we aim for the mentioned approach of two components coupling to electric and magnetic field separately. Note that, although we use these two components separately, they are still part of the same laser field and connected with each other by the Maxwell equations. We are interested in the responses, and therefore the susceptibilities, at the probe field frequency.

We will achieve negative refraction at low losses through tailoring the magnetic and electric responses of our two-component medium such that we obtain a strongly negative real part of the index of refraction and a small imaginary part at the same frequency, since a small imaginary part of the index of refraction implies low absorption. However, since the square of the index of refraction is given by Eq. (1.2), there exist the two solutions of Eq. (1.3) for the index of refraction itself which we denote by

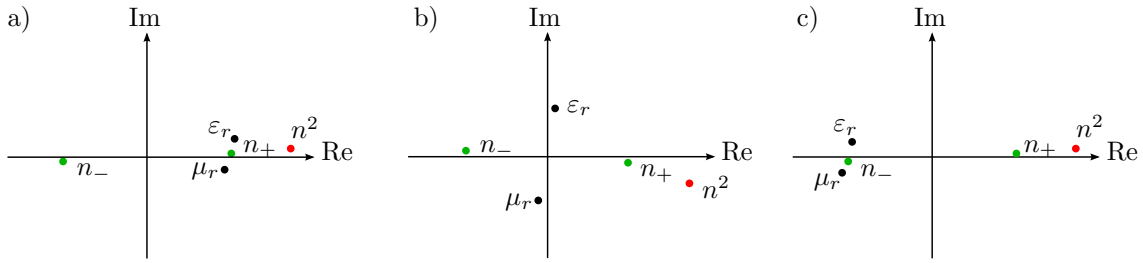

Figure 2.1: Three sets of exemplary values of permittivity μ_r and permeability ε_r to achieve negative refraction with low losses. Here, $n_- = -\sqrt{\mu_r \varepsilon_r}$ and $n_+ = +\sqrt{\mu_r \varepsilon_r}$ are the two possible solutions of Eq. (1.2). In the following, we will consider the case depicted in c).

$$n_- = -\sqrt{\varepsilon_r \mu_r}\,, \tag{2.1a}$$
$$n_+ = \sqrt{\varepsilon_r \mu_r}\,, \tag{2.1b}$$

Here, one of the two signs yields the retarded solution of the index of refraction, the other one the advanced solution. Since only the retarded solution is causal and therefore physical, we have to pick the right sign in order to obtain the physical solution of the index of refraction. Still, it is not a priori obvious which sign has to be chosen. This issue will be addressed in Sec. 4.1.2. For now, we visualize the permittivity ε_r, the permeability μ_r, the square of the index of refraction and the two solutions for the index of refraction n_- and n_+ in the complex plane at a single frequency (see Fig. 2.1).

Solutions for the refractive index that lie close to the real axes have a small imaginary part. Also, if one solution, say n_-, lies close to the real axis, the other one — n_+ — also does and one of the two has a negative real part. Therefore, as one can see by Eq. (2.1), in principle permittivities $\varepsilon_r = |\varepsilon_r| e^{i\phi_\varepsilon}, \phi_\varepsilon \in (-\pi, \pi]$ and permeabilities $\mu_r = |\mu_r| e^{i\phi_\mu}, \phi_\mu \in (-\pi, \pi]$ whose polar angles ϕ_ε and ϕ_μ add up to $-2\pi, 0, 2\pi$ are interesting. In particular, this is the case if $|\phi_\varepsilon| \approx \pi$ and $|\phi_\mu| \approx \pi$, which means that the imaginary parts of permittivity and permeability are small and the real parts are negative (see Fig. 2.1 c)). This is also the situation that Veselago examined in [1]. Considering a real permittivity and a real permeability, he deduced that the index of refraction has to be assigned a negative value if the permittivity and the permeability are negative.

Motivated by this, in the following we use coherent control fields and incoherent pumping to prepare the medium in such a way that the response to the incident magnetic probe field component — the permeability — has a small imaginary part and a negative real part. According to Eqs. (1.1), this also implies a negative real

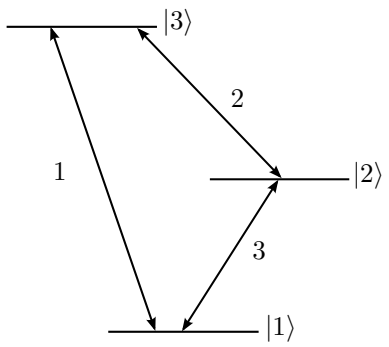

Figure 2.2: The above image illustrates the labelling we are going to use for the investigation of several three-level systems with respect to their suitability for the magnetic contribution in a negatively refracting two-component system.

part and a small imaginary part of the magnetic susceptibility. The permittivity should be optimized in the same way. Since this has already been done in [17, 18], we focus on the magnetic part here. Later on, these optimized susceptibilities will help us to achieve negative refraction with low losses.

2.1 Theoretical preparation

2.1.1 The general model

In this chapter, we will consider systems that consist of three energy levels labelled $|1\rangle, |2\rangle$ and $|3\rangle$ with increasing energy (see Fig. 2.2). The three transitions are also labelled from 1 to 3, in the order also shown in Fig. 2.2. This being the general structure of our system, we investigate different configurations of three-level systems in the following subsections. Therefore, we will apply several electromagnetic fields: one probe field, one or two coherent control fields and sometimes also fields that pump incoherently.

Of course, we also include incoherent decays on the transitions, the rate of which depends on their multipolarity and their character as magnetic or electric transitions. As already mentioned, we also apply incoherent pumping in one direction on some transitions. This can be seen as inverted incoherent decay and can be realized in an experiment in two ways: Incoherent pumping in one direction, namely to a higher energy level $|e\rangle$, can be achieved by coherent pumping — with a laser — to an auxiliary energy level $|a\rangle$ at even higher energy than $|e\rangle$ which then decays incoherently to level $|e\rangle$. On the other hand, if one destroys the coherence of laser light by putting a hazy glass plate between laser and medium, one can realize incoherent

pumping in both directions.

Also, coherent pumping between a ground state $|g\rangle$ and an excited state $|e\rangle$ causes Rabi oscillations. This means that the populations are shifted from one state to the other and back. Incoherent decay, however, damps these oscillations and creates a steady state in the long-time limit in which the populations do not change anymore. The steady state is also the situation for which we will solve our equations of motion later on.

Further parameters are the detunings of the coherent control fields with respect to the transitions they couple to.

2.1.2 The magnetic response

Let us now come to the magnetic susceptibility χ_m or, more precisely, its Fourier transform $\tilde{\chi}_m$. This is the quantity that we want to calculate, since it gives the magnetic response to the magnetic field. It is connected to the permeability μ_r via Eq.(1.1b) and the sign of its imaginary part provides information about the absorptive behavior of the associated system.

As a sidenote, let us mention that the absorptive behavior is originally given by the imaginary part of the index of refraction and not the magnetic susceptibility. Still, an expansion of the index of refraction n in the imaginary part of the magnetic susceptibility $\tilde{\chi}_m$ shows that, for small imaginary parts of the susceptibility, the sign of $\mathrm{Im}(n)$ is given by the sign of $\mathrm{Im}(\tilde{\chi}_m)$. Here, $\tilde{\chi}_m$ denotes the magnetic susceptibility in Fourier space, while the electric susceptibility is assumed to be equal to one.

To start, we define the linear magnetic susceptibility by

$$\begin{aligned} \vec{M}(\vec{r},t) &= \int_{-\infty}^{\infty} \chi_m(\tau)\, \vec{H}(\vec{r},t-\tau)\, d\tau \\ &= \int_{-\infty}^{\infty} \frac{1}{\mu_0}\, \chi_m(\tau)\, \vec{B}(\vec{r},t-\tau)\, d\tau \end{aligned} \tag{2.2}$$

as the linear response coefficient that connects the incident magnetic field $\vec{H}$ and the magnetization $\vec{M}$ caused by the magnetic field. Both the magnetization and the magnetic field are considered at position $\vec{r}$ and time t. We used the relation $\vec{B} = \mu_0 \vec{H}$ here, since both $\vec{B}$ and $\vec{H}$ are external fields. Note that $\chi_m(t) \equiv 0$ for $t < 0$ due to causality in Eq. (2.2), since magnetic fields at a certain point in time cannot influence the magnetization at an earlier point in time.

There are several things to note when using Eq. (2.2): First, we only take into account the linear response to the magnetic field. Terms of higher order in the magnetic probe field component than the linear one can be neglected, as the incident probe field is typically weak.

Also, the magnetization in Eq. (2.2) is only given as response to the magnetic field. However, the electric field can also contribute to the magnetic response [17, 18] which gives rise to so-called chirality terms in Eq. (2.2). Nevertheless, in the systems we examine in this chapter, we do not need the chirality term, since we focus on systems that couple only to the magnetic probe field component and not to the electric part. By contrast, in Sec. 3, we will consider systems that couple to both probe field components. In these systems, chirality terms will play an important role and finally lead to an enhancement of the magnetic response.

In general, the magnetic susceptibility is a tensor. However, we work in a homogeneous, isotropic medium. Also, the electric probe field component which in principle could introduce another axis and therefore a chiral character does not couple to the medium considered here. For this reason, the susceptibilities reduce to scalars.

In particular, we write our total magnetic field as

$$\vec{B}(\vec{r},t) = \vec{B}_p(\vec{r})e^{i\phi}e^{-i\omega_p t} + \sum_{\lambda=1}^{o} \vec{B}_\lambda(\vec{r})e^{i\psi_\lambda}e^{-i\omega_{c,\lambda}t} + \text{ c.c. }, \tag{2.3}$$

where the subindex p refers to the probe field, while λ and c,λ ($\lambda \in \{1, ...0\}$) refer to the different control fields. Here, o is the number of applied control fields. However, we will only use two control fields at most in a later section, namely in Sec. 4.2.3.

Further, $\vec{B}_p(\vec{r}) = \mathcal{B}_p\vec{b}_p e^{i\vec{k}_p\vec{r}}$, where $\mathcal{B}_p$ is the electric field amplitude, $\vec{b}_p$ the unit polarization vector of the electric component of the probe field, $\vec{k}_p$ is the probe field's wave vector, ω_p its frequency and ϕ its absolute phase.

Analogously, $\vec{B}_\lambda(\vec{r}) = \mathcal{B}_\lambda\vec{b}_\lambda e^{i\vec{k}_\lambda\vec{r}}$, where $\mathcal{B}_\lambda$ ($\lambda \in \{1, ...o\}$) is the amplitude of the respective control field and $\vec{b}_\lambda$ its unit polarization vector. $\vec{k}_\lambda$ is the wave vector of the control field labelled λ, $\omega_{c,\lambda}$ its frequency and ψ_λ its total phase.

As a side note, let us mention that the unit polarization vector of the magnetic probe field component is related to the unit polarization vector $\vec{e}_p$ of the electric probe field component by $\vec{b}_p = \vec{\kappa} \times \vec{e}_p$ where $\vec{\kappa}$ is the unit vector in the direction of the wave vector, $\vec{\kappa} = \vec{k}_p/k_p$. This relation can easily be seen by one of the Maxwell equations in Fourier space, namely

$$\vec{B} = \frac{\vec{k}}{\omega} \times \vec{E} \tag{2.4}$$

and the fact that in SI system

$$|\vec{E}| = c|\vec{B}| \,. \tag{2.5}$$

For definitiveness, we will from now on consider a σ^+-polarized electric probe field that propagates in positive z-direction. This means that $\vec{\kappa} = \vec{z}$ and the unit polarization vector of the electric field becomes $\vec{e}_p = \frac{1}{\sqrt{2}}(\vec{x} + i\vec{y})$. $\vec{x}, \vec{y}$ and $\vec{z}$ are the orthonormal basis vectors of our Cartesian coordinate system. Therefore, we obtain a simple relation between the unit vectors of the two probe field components:

$$\vec{b}_p = \vec{z} \times (\vec{x} + i\vec{y})/\sqrt{2} = \begin{pmatrix} 0 \\ 0 \\ 1 \end{pmatrix} \times \frac{1}{\sqrt{2}} \begin{pmatrix} 1 \\ i \\ 0 \end{pmatrix} = -\frac{i}{\sqrt{2}} \begin{pmatrix} 1 \\ i \\ 0 \end{pmatrix} = -i\vec{e}_p \tag{2.6}$$

Let us now proceed with the derivation of an expression for the magnetic susceptibility. Plugging Eq. (2.3) into Eq. (2.2), we can write

$$\vec{M}(\vec{r}, t) = \frac{1}{\mu_0}\tilde{\chi}_m(\omega_p)\vec{B}_p(\vec{r})e^{i(\phi - \omega_p t)} + \frac{1}{\mu_0}\tilde{\chi}_m(\omega_c)\vec{B}_c(\vec{r})e^{i(\psi - \omega_c t)} + c.c. \,. \tag{2.7}$$

Here, $\tilde{\chi}_m$ is the Fourier transform of χ_m, i.e.

$$\tilde{\chi}_m(\omega) = \int_{-\infty}^{\infty} \chi_m(\tau)e^{i\omega\tau}d\tau \tag{2.8}$$

Besides the classical definition as linear response to the magnetic field, the magnetization can also be calculated in a quantum mechanical way: It is given by $\vec{M} = \mathrm{N}\vec{m}$, where N is the particle density and $\vec{m}$ the mean magnetic moment per atom [23]. We can express the mean magnetic moment as $\vec{m} = \mathrm{Tr}(\varrho\vec{\mu})$, where Tr(A) denotes the trace of matrix A, ϱ is the density matrix operator of the examined system and $\vec{\mu}$ is the magnetic dipole operator. Explicitly, we have

$$\begin{aligned} \vec{M} &= \mathrm{N}\,\mathrm{Tr}(\varrho\vec{\mu}) \\ &= \mathrm{N}\sum_{i \to j} (\varrho_{ij}\vec{\mu}_{ji} + c.c.) \end{aligned} \tag{2.9}$$

The involved sum includes all transitions $i \to j\,(i, j \in \{1, 2, 3\})$ of the system that are dipole allowed. It only sums over each pair (i,j) once - which is why the complex conjugated part appears. Moreover, $\varrho_{ij} = \langle i|\varrho|j\rangle$ and $\vec{\mu}_{ij} = \langle i|\vec{\mu}|j\rangle$ are the matrix

elements of the density matrix and the magnetic dipole moment in the atomic energy eigenstate basis $|i\rangle$ ($i \in \{1, 2, 3\}$).

Of course, the sum does not contain diagonal elements and no electric dipole transitions, since $\vec{\mu}_{ij}$ vanishes for i = j and for electric dipole transitions.

Now, we equal Eqs. (2.9) and (2.7) and obtain

$$\frac{1}{\mu_0}\tilde{\chi}_m(\omega_p)\vec{B}_p(\vec{r})e^{i(\phi-\omega_p t)} + \frac{1}{\mu_0}\tilde{\chi}_m(\omega_c)\vec{B}_c(\vec{r})e^{i(\psi-\omega_c t)} + c.c. = \mathrm{N}\sum_{i\to j}(\varrho_{ij}\vec{\mu}_{ji} + c.c.) \tag{2.10}$$

We are interested in the response at the probe field frequency and therefore in $\tilde{\chi}_m(\omega_p)$. To obtain it, we need to know which part of the right hand side of Eq. (2.10) oscillates in phase with $e^{-i\omega_p t}$ to do a comparison of coefficients. This can be easily found out by transforming the density matrix elements ϱ_{ij} into an appropriate frame in which the Hamiltonian and therefore the transformed density matrix elements $\tilde{\varrho}_{ij}$ are time-independent. In the systems we consider in this section, such a Hamiltonian can always be found — in contrast to Sec. 3. Moreover, the transformed, time-independent coherence $\tilde{\varrho}_{i_0 j_0}$ of the probe transition $|j_0\rangle \to |i_0\rangle$, $i_0 > j_0$, is the only matrix element which transforms according to (cp. Eqs. (2.25))

$$\tilde{\varrho}_{i_0 j_0} = e^{i\omega_p t}\varrho_{i_0 j_0}\,. \tag{2.11}$$

If we now write Eq. (2.10) in terms of the transformed coherences so that the time dependence becomes explicit and then take the coefficients of $e^{-i\omega_p t}$, we obtain

$$\frac{1}{\mu_0}\tilde{\chi}_m(\omega_p)\vec{B}_p(\vec{r})e^{i\phi} = \mathrm{N}\tilde{\varrho}_{i_0 j_0}\vec{\mu}_{j_0 i_0}\,. \tag{2.12}$$

In order to solve this equation for $\tilde{\chi}_m(\omega_p)$, we expand $\tilde{\varrho}_{i_0 j_0}$ in the following way:

$$\tilde{\varrho}_{i_0 j_0} = \tilde{\varrho}^{(0)}_{i_0 j_0} + \tilde{\varrho}^{(1)}_{i_0 j_0}\Omega_{i_0 j_0} \tag{2.13}$$

where we defined the Rabi frequency of the probe transition

$$\Omega_{i_0 j_0} = e^{i\phi}\vec{B}_p(\vec{r})\,\vec{\mu}_{i_0 j_0}/\hbar\,, \tag{2.14}$$

which gives us the coupling strength of the magnetic probe field to the magnetic probe transition. When we derive equations of motion for the density matrix elements in Sec. 2.1.3 to obtain $\tilde{\varrho}_{i_0 j_0}$, it will become clear that $\tilde{\varrho}_{i_0 j_0}$ depends on $\Omega_{i_0 j_0}$

and can therefore be expanded in it. Also, when solving the equations of motion, one sees that $\tilde{\varrho}^{(0)}_{i_0 j_0}$ vanishes and therefore

$$\tilde{\varrho}_{i_0 j_0} = \tilde{\varrho}^{(1)}_{i_0 j_0} \Omega_{i_0 j_0} \, . \tag{2.15}$$

As already mentioned, we only consider the responses up to linear order in the probe field. Therefore, we neglected terms of second or higher order in $\Omega_{i_0 j_0}$ in Eqs. (2.13) and (2.15).

We now multiply Eq. (2.12) with $\vec{b}^*_p$ from the left. Using Eqs. (2.15) and (2.14), we thus obtain

$$\frac{1}{\mu_0}\tilde{\chi}_m(\omega_p)\vec{b}^*_p\vec{B}_p(\vec{r})e^{i\phi} = \mathrm{N}\tilde{\varrho}^{(1)}_{i_0 j_0} e^{i\phi}/\hbar \left(\vec{B}_p(\vec{r})\, \vec{\mu}_{i_0 j_0}\right)\left(\vec{b}^*_p \vec{\mu}_{j_0 i_0}\right) \tag{2.16}$$

Using the definition of $\vec{B}_p(\vec{r})$ and the fact that $\vec{b}^*_p\vec{b}_p = 1$, we rewrite this equation.

$$\frac{1}{\mu_0}\tilde{\chi}_m(\omega_p)\mathcal{B}_p e^{i\vec{k}_p\vec{r}}e^{i\phi} = \mathrm{N}\tilde{\varrho}^{(1)}_{i_0 j_0}\mathcal{B}_p e^{i\vec{k}_p\vec{r}}e^{i\phi}/\hbar \left(\vec{b}_p\, \vec{\mu}_{i_0 j_0}\right)\left(\vec{b}^*_p \vec{\mu}_{j_0 i_0}\right) \tag{2.17}$$

Solving for the magnetic susceptibility yields

$$\tilde{\chi}_m(\omega_p) = \frac{\mathrm{N}\mu_0}{\hbar}|\mu_{i_0 j_0}|^2 \tilde{\varrho}^{(1)}_{i_0 j_0} \tag{2.18}$$

where $\mu_{i_0 j_0} = \vec{b}_p\, \vec{\mu}_{i_0 j_0}$.

2.1.3 The equations of motion

According to Eq. (2.18), we need the coherence $\tilde{\varrho}_{i_0 j_0}$ of the probe transition $|j_0\rangle \rightarrow |i_0\rangle$ in a system oscillating in phase with the probe field — or, more precisely and more general, the very part of the sum in Eq. (2.10) that oscillates in phase with the probe field — in order to obtain the magnetic susceptibility. In other words, we need the density matrix elements.

Therefore, we have to solve the equations of motion for the density matrix ϱ, i.e. the master equation, given here in Lindblad form [24]:

$$\begin{aligned}\frac{\partial \varrho}{\partial t} = & - \frac{i}{\hbar}\left[H, \varrho\right] - \sum_{\alpha=1}^{3}\frac{\gamma_\alpha}{2}\left(\left[\varrho S^+_\alpha, S^-_\alpha\right] + \left[S^+_\alpha, S^-_\alpha \varrho\right]\right) \\ & - \sum_{\alpha=1}^{3}\frac{r_\alpha}{2}\left(\left[\varrho S^-_\alpha, S^+_\alpha\right] + \left[S^-_\alpha, S^+_\alpha \varrho\right]\right) \, .\end{aligned} \tag{2.19}$$

We used the rotating wave and Born-Markov approximations and included incoherent pump rates r_α here. Also, quantum inference induced by incoherent cross coupling between the atomic transitions does not have to be included here, since the transitions of our system are not resonant with respect to each other. The number of photons in the vacuum field modes at the involved transition frequencies is set to zero. The latter is reasonable, since for optical transitions in the atom, the vacuum field can be described by $T = 0$.

Here, the α denote different transitions, i.e. the sums range over all transitions in the atom. Therefore, $\alpha \in \{1, 2, 3\}$ in a three-level system. γ_α is the incoherent decay rate on the transition labelled by α, r_α denotes an incoherent pump rate on the same transition. The S_α^+ are the transition operators of transition α and $S_\alpha^- = (S_\alpha^+)^\dagger$. E.g. if $\alpha = 1$ denotes the transition $|1\rangle \rightarrow |3\rangle$ — as is the case in our schemes according to Fig. 2.2 — then $S_1^+ = |3\rangle\langle 1|$ and $S_1^- = |1\rangle\langle 3|$.

Finally, the Hamiltonian H which determines the unitary part of Eq. (2.19) is given by

$$H = H_0 + H_I \,, \tag{2.20}$$

where, in rotating wave and dipole approximation,

$$H_0 = \sum_{i=1}^{3} \hbar\omega_i \,, \tag{2.21a}$$

$$H_I = -\hbar \left(\Omega_{21} e^{-i\omega_p t} \underbrace{|2\rangle\langle 1|}_{S_3^+} + \Omega_{32} e^{-i\omega_c t} \underbrace{|3\rangle\langle 2|}_{S_2^+} + H.c.\right) . \tag{2.21b}$$

For a better readability, we gave up total generality here and wrote down the Hamiltonian of a special system, namely the upper microwave system in Sec. 2.3.1 as seen in Fig. 2.3. Therefore, the probe transition now is $|1\rangle \rightarrow |2\rangle$, i.e. $i_0 = 2$ and $j_0 = 1$. Also, we only have one control field which couples to transition $|2\rangle \rightarrow |3\rangle$ and whose frequency we simply denoted by ω_c.

When considering another system, one only has to change the indices for the probe transition and the transition to which the control field couples. A second control field would only require the introduction of another term in the sum of Eq. (2.21b) analogously to the first control field term.

The $\omega_i, i \in \{1, 2, 3\}$, are the eigenfrequencies of the atomic states, while the Rabi frequencies that determine the coupling strength of the involved fields to the respective transitions are defined as

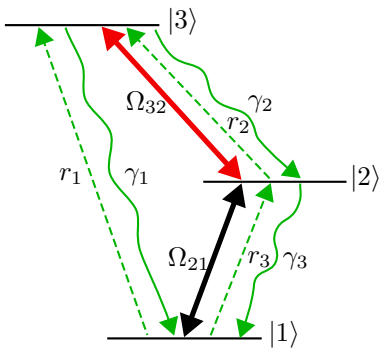

Figure 2.3: The upper microwave scheme includes a control field Ω_{32} (red, two arrowheads) coupling to transition $|2\rangle \rightarrow |3\rangle$, a probe field Ω_{21} (black, two arrowheads) coupling to the magnetic probe transition $|1\rangle \rightarrow |2\rangle$, incoherent decay rates $\gamma_\alpha, \alpha \in \{1,2,3\}$ (wiggly green arrows) and incoherent pump rates $r_\alpha, \alpha \in \{1,2,3\}$ (straight, dashed green arrows) on each transition.

$$\Omega_{21} = e^{i\phi}\vec{B}_p(\vec{r})\,\vec{\mu}_{21}/\hbar\,, \tag{2.22a}$$

$$\Omega_{32} = e^{i\psi}\vec{B}_c(\vec{r})\,\vec{\mu}_{32}/\hbar\,. \tag{2.22b}$$

Here, we assumed transition $|2\rangle \rightarrow |3\rangle$ to be a magnetic dipole transition with magnetic dipole moment $\vec{\mu}_{32}$. Therefore, the magnetic component of the control field couples to it.

If transition $|2\rangle \rightarrow |3\rangle$ was an electric dipole transition, one would have to replace $\vec{B}_c$ by the corresponding part $\vec{E}_c$ of the electric component of the control field and $\vec{\mu}_{32}$ by an electric dipole moment, usually denoted by $\vec{d}_{32}$.

In order to dispose of the time-dependence of the Hamiltonian in Eqs. (2.21) is, we transform the Hamiltonian according to

$$V = e^{\frac{i}{\hbar}(H_0+X)t}(H_I - X)e^{-\frac{i}{\hbar}(H_0+X)t}\,, \tag{2.23}$$

where $X = \sum_{i=1}^{3} x_i|i\rangle\langle i|$. If one chooses $x_1 = \Delta_3 = \omega_2 - \omega_1 - \omega_p$, $x_2 = 0$ and $x_3 = -\Delta_2 = \omega_2 - \omega_3 + \omega_c$, the Hamiltonian becomes time-independent. Here Δ_3 and Δ_2 are the detunings of the fields that are applied to transitions 3 and 2, respectively.

Accordingly, in the upper microwave system, the transformed density matrix elements $\tilde{\varrho}_{ij}$ are given as

$$\tilde{\varrho}_{ij} = e^{i(\omega_i - \omega_j + x_i - x_j)t} \varrho_{ij} \; . \tag{2.24}$$

In particular,

$$\begin{aligned}
\tilde{\varrho}_{21} &= e^{i\omega_p t} \varrho_{21} \; , && \text{(2.25a)} \\
\tilde{\varrho}_{32} &= e^{i\omega_c t} \varrho_{32} \; , && \text{(2.25b)} \\
\tilde{\varrho}_{31} &= e^{i(\omega_p + \omega_c)t} \varrho_{31} \; , && \text{(2.25c)}
\end{aligned}$$

where the $\tilde{\varrho}_{ij}$ are now time-independent. One can see that the coherence of the probe transition ϱ_{21} is the only one oscillating at the probe field frequency and therefore the only one that has to be taken into account when calculating the response.

The transformed density matrix obeys

$$\begin{aligned}
\frac{\partial \tilde{\varrho}}{\partial t} = & - \frac{i}{\hbar} [V, \tilde{\varrho}] - \sum_{\alpha=1}^{3} \frac{\gamma_\alpha}{2} \left(\left[\tilde{\varrho} S_\alpha^+, S_\alpha^- \right] + \left[S_\alpha^+, S_\alpha^- \tilde{\varrho} \right] \right) \\
& - \sum_{\alpha=1}^{3} \frac{r_\alpha}{2} \left(\left[\tilde{\varrho} S_\alpha^-, S_\alpha^+ \right] + \left[S_\alpha^-, S_\alpha^+ \tilde{\varrho} \right] \right) && \text{(2.26)}
\end{aligned}$$

or, explicitly,

$$\begin{aligned}
\frac{\partial}{\partial t} \tilde{\varrho}_{11} = & - (r_1 + r_3) \tilde{\varrho}_{11} + \gamma_3 \tilde{\varrho}_{22} + \gamma_1 \tilde{\varrho}_{33} + i\Omega_{12} \tilde{\varrho}_{21} \\
& - i\Omega_{21} \tilde{\varrho}_{12} \; , && \text{(2.27a)} \\
\frac{\partial}{\partial t} \tilde{\varrho}_{21} = & - \left[\frac{1}{2} (r_1 + r_2 + r_3 + \gamma_3) + i\Delta_3 \right] \tilde{\varrho}_{21} + i\Omega_{23} \tilde{\varrho}_{31} \\
& + i\Omega_{21} (\tilde{\varrho}_{11} - \tilde{\varrho}_{22}) \; , && \text{(2.27b)} \\
\frac{\partial}{\partial t} \tilde{\varrho}_{22} = & - (\gamma_3 + r_2) \tilde{\varrho}_{22} + \gamma_2 \tilde{\varrho}_{33} + r_3 \tilde{\varrho}_{11} - i\Omega_{12} \tilde{\varrho}_{21} \\
& + i\Omega_{21} \tilde{\varrho}_{12} - i\Omega_{32} \tilde{\varrho}_{23} + i\Omega_{23} \tilde{\varrho}_{32} \; , && \text{(2.27c)} \\
\frac{\partial}{\partial t} \tilde{\varrho}_{31} = & - \left[\frac{1}{2} (r_1 + r_3 + \gamma_1 + \gamma_2) + i (\Delta_2 + \Delta_3) \right] \tilde{\varrho}_{31} \\
& + i\Omega_{32} \tilde{\varrho}_{21} - i\Omega_{21} \tilde{\varrho}_{32} \; , && \text{(2.27d)} \\
\frac{\partial}{\partial t} \tilde{\varrho}_{32} = & - \left[\frac{1}{2} (r_2 + \gamma_1 + \gamma_2 + \gamma_3) + i\Delta_2 \right] \tilde{\varrho}_{32} \\
& - i\Omega_{12} \tilde{\varrho}_{31} - i\Omega_{32} (\tilde{\varrho}_{33} - \tilde{\varrho}_{22}) \; , && \text{(2.27e)} \\
\tilde{\varrho}_{33} = & \, 1 - \tilde{\varrho}_{11} - \tilde{\varrho}_{22} \; . && \text{(2.27f)}
\end{aligned}$$

If one then plugs Eq. (2.27f) into the other Eqs. (2.27), one obtains a system of equations of the form

$$\frac{\partial}{\partial t}\tilde{R} = M\tilde{R} + \Sigma\,, \tag{2.28}$$

where we defined

$$\tilde{R} = (\tilde{\varrho}_{11}, \tilde{\varrho}_{12}, \tilde{\varrho}_{13}, \tilde{\varrho}_{21}, \tilde{\varrho}_{22}, \tilde{\varrho}_{23}, \tilde{\varrho}_{31}, \tilde{\varrho}_{32})^T\,. \tag{2.29}$$

M is a matrix and Σ a vector that can be determined by the equations of motion.

We solve Eq. (2.28) for $\tilde{R}$ in the long time limit and therefore assume that the density matrix elements become constant after some time. Indeed, this is the case after Rabi oscillations have been damped away. This damping takes place on a timescale that corresponds to the reciprocals of the involved incoherent decay rates. Therefore, we set $\frac{\partial}{\partial t}\tilde{R} = 0$ and solve Eq. (2.28) as

$$\tilde{R} = -M^{-1}\Sigma\,. \tag{2.30}$$

Note that in this solution we neglect terms that are of higher than first order in the probe field Rabi frequency which is small due to the weak probe field. The fourth component of Eq. (2.30) now yields the solution for the coherence $\tilde{\varrho}_{21} = \tilde{\varrho}_{i_0 j_0}$ of the probe transition. With Eq. (2.18), one can then calculate the magnetic susceptibility which determines the permeability according to Eq. (1.1b) and consequently also the index of refraction.

2.2 Two-level system

Although we considered three-level systems in the previous derivation, we would like to briefly include the two level system here. Of course, the two level system has been investigated thoroughly (e.g., see [23]) and its derivation much simpler than the previous one. One can also obtain its equations of motion by simply setting $\Omega_{32} = \Omega_{23} = 0$ and $r_1 = r_2 = 0$ in the presented upper microwave system. The simplicity of two-level systems should make it easier to realize them in experiment compared to more complicated multi-level systems. Also, two level systems will turn out to have another advantage: They do not exhibit any branch points for arbitrary parameters. What this means will be examined in detail in Sec. 4.1.4. For now, let us simply state that this implies that there are no absolute instabilities in the medium for any choice of parameters. These are points in space at which the electric field grows infinitely large.

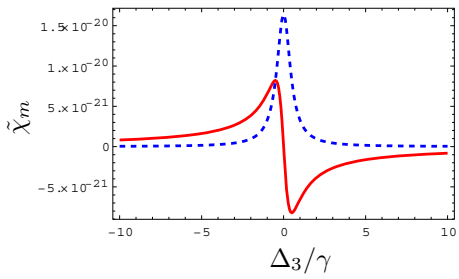

Figure 2.4: The above figure shows the typical structure of the magnetic susceptibility of a two-level system. The real part is plotted as a red line, the imaginary part as a blue dashed line.

The probe transition's coherence is given by

$$\tilde{\varrho}_{21} = \Omega_{21} \frac{2i\left(\tilde{\varrho}_{11}^{(0)} - \tilde{\varrho}_{22}^{(0)}\right)}{r + \gamma + 2i\Delta} \tag{2.31}$$

in terms of the populations in zeroth order of the probe field Rabi frequency

$$\tilde{\varrho}_{11}^{(0)} = \frac{\gamma}{r+\gamma}\,, \tag{2.32}$$

$$\tilde{\varrho}_{22}^{(0)} = \frac{r}{r+\gamma}\,. \tag{2.33}$$

Here, $|2\rangle$ is the excited state, $|1\rangle$ the ground state, r the incoherent pump rate $|1\rangle \rightarrow |2\rangle$, γ the decay rate and Ω_{21} the probe field Rabi frequency.

2.3 Three-level systems

With Eq. (2.18) and the given method to derive the equations of motion and to solve these for the coherence of the probe transition, we will now calculate the magnetic susceptibility and thus the magnetic response of several three level systems. Since our final goal is to use them for lossless negative refraction, we will put special emphasis on parameters that allow for small or vanishing imaginary part of the magnetic susceptibility.

In the following, we will express all parameters as multiples of the decay rate of the probe transition. E.g. for a probe transition labelled 3, the detuning of the probe transition Δ_3 will be expressed as $\Delta_3 = \delta\gamma_3$. As one can see at Eq. (2.18), we also

need $|\mu_{i_0 j_0}|$, the magnetic dipole moment of the probe transition $|j_0\rangle \rightarrow |i_0\rangle$. We assume one-photon radiative decay. Therefore, we can use the relation [26]

$$|\mu_{i_0 j_0}| = \sqrt{\gamma_\alpha \frac{3\pi\hbar c^3}{e^2 \mu_0 \left(\omega_{i_0} - \omega_{j_0}\right)^3}}\,, \tag{2.34}$$

where ω_{i_0} and ω_{j_0} are the eigenfrequencies of states $|\omega_{i_0}\rangle$ and $|\omega_{j_0}\rangle$ and γ_α, $\alpha \in \{1,2,3\}$, is the decay rate on the probe transition $|j_0\rangle \rightarrow |i_0\rangle$. E.g., this could refer to the decay rate γ_3 of the probe transition $|1\rangle \rightarrow |2\rangle$ which is labelled 3. $\hbar$ is the Planck constant, e the elementary charge and μ_0 the vacuum permeability.

For all schemes, we will split the section in three parts: In the first and the second, we will use typical parameters. Since we have three transitions in total, while the probe transition is always magnetic, the other transitions can either both be electric dipole transitions too (part 1) or magnetic dipole transitions (part 2). Any other combination of transitions would violate the parity rules for magnetic transitions which occur between states of the same parity and for electric transitions which occur between states of different parity. As an example, the third part introduces a real system, namely nitrogen, and shows how one has to modify the ideal parameters to achieve similar results in the real system. As mentioned in Sec. 5.2, there are also other possible real systems, such as oxygen, magnesium, carbon and phosphorus.

We will give all results for a particle density of $N = 1\ m^{-3}$, since the magnetic susceptibility scales linearly with the particle density. Moreover, the frequency of the probe transition will assumed to be optical: We choose it in such a way that the corresponding wavelength is $\lambda = 2\pi\frac{c}{\omega_{i_0} - \omega_{j_0}} = 600\,\text{nm}$. Only in the case of a nitrogen-like system, we will choose $\lambda = 520.1705\,\text{nm}$.

2.3.1 Upper microwave scheme

First, we solve the equations of motion (2.27) explicitly for the upper microwave scheme shown in Fig. 2.3, which includes one control field with Rabi frequency Ω_{32} coupling to the transition $|2\rangle \rightarrow |3\rangle$ and one probe field with Rabi frequency Ω_{21} coupling to the magnetic probe transition $|1\rangle \rightarrow |2\rangle$. To first order in the probe field Rabi frequency Ω_{21}, we obtain

$$\tilde{\varrho}_{21} = -\Omega_{21} \frac{2i\left[4\left(\tilde{\varrho}_{33}^{(0)} - \tilde{\varrho}_{22}^{(0)}\right)|\Omega_{23}|^2 + \left(\tilde{\varrho}_{22}^{(0)} - \tilde{\varrho}_{11}^{(0)}\right)\left(r_2 + \gamma_{123} + 2i\Delta_2\right)B_0\right]}{\left(r_2 + \gamma_{123} + 2i\Delta_2\right)\left[4|\Omega_{23}|^2 + \left(r_{123} + \gamma_3 + 2i\Delta_3\right)B_0\right]}\,, \tag{2.35}$$

where

$$B_0 = r_{13} + \gamma_{12} + 2i\Delta_2 + 2i\Delta_3 \,. \tag{2.36}$$

Moreover,

$$\tilde{\varrho}_{11}^{(0)} = \frac{4|\Omega_{23}|^2\gamma_{13}\left(r_2+\gamma_{123}\right)+\left(r_2\gamma_1+\gamma_{12}\gamma_3\right)B_1}{B_3+B_2B_1}\,, \tag{2.37}$$

$$\tilde{\varrho}_{22}^{(0)} = \frac{4|\Omega_{23}|^2 r_{13}\left(r_2+\gamma_{123}\right)+\left(r_1\gamma_2+\gamma_{12}r_3\right)B_1}{B_3+B_2B_1}\,, \tag{2.38}$$

$$\tilde{\varrho}_{33}^{(0)} = \frac{4|\Omega_{23}|^2 r_{13}\left(r_2+\gamma_{123}\right)+\left(r_1\gamma_3+r_2r_{13}\right)B_1}{B_3+B_2B_1}\,, \tag{2.39}$$

are the populations of the three levels in zeroth order of the probe field. Here, quantities that are indexed with multiple digits are defined to be the sum of the corresponding single-indexed quantities, e.g. $\gamma_{123} = \gamma_1 + \gamma_2 + \gamma_3$ or $r_{23} = r_2 + r_3$. Also, we defined

$$B_1 = r_2^2 + \gamma_1^2 + \gamma_2^2 + \gamma_3^2 + 2\gamma_2\gamma_3 + 2\gamma_1\gamma_{23} + 2r_2\gamma_{123} + 4\Delta_2^2\,, \tag{2.40}$$

$$B_2 = r_2\left(r_3+\gamma_1\right) + \gamma_{12}\left(r_3+\gamma_3\right) + r_1\left(r_2+\gamma_{23}\right)\,, \tag{2.41}$$

$$B_3 = 4|\Omega_{32}|^2\left(2r_{13}+\gamma_{13}\right)\left(r_2+\gamma_{123}\right)\,. \tag{2.42}$$

Electric transitions

We now assume transitions $|1\rangle \to |3\rangle$ and $|2\rangle \to |3\rangle$ which are labelled 1 and 2 to be electric dipole transitions. We express the decay rates in units of the decay rate $\gamma_3 = \gamma$ of the probe transition. Typical decay rates for electric dipole transitions are then given by $\gamma_1 = \alpha^{-2}\gamma$ and $\gamma_2 = \alpha^{-2}\gamma$.

The factor of α^{-2} can be seen as follows. The absolute value of the electric dipole moment d_{ij} of a radiative electric dipole transition $|j\rangle \to |i\rangle$ labelled α is given by

$$d = |d_{ij}| = \sqrt{\gamma_\alpha \frac{3\pi\varepsilon_0\hbar c^3}{e^2\left(\omega_i-\omega_j\right)^3}}\,, \tag{2.43}$$

where the quantities have the same meaning as in the analogous Eq. (2.34). Also, in an atom, the absolute values of a typical magnetic transition dipole moment μ and a typical electric dipole moment d are given by

$$\mu \sim \mu_B \sim e a_0 \alpha c\,, \tag{2.44a}$$

$$d \sim e a_0\,, \tag{2.44b}$$

parametrically, where μ_B is the Bohr magneton, e the elementary charge, a_0 the Bohr radius and c the vacuum speed of light (in SI units). With this parametric estimation and Eqs. (2.34) and (2.43), the factor α^{-2} that relates electric and magnetic dipole decay rates, is obtained.

In Fig. 2.5 c) - g), we show magnetic susceptibilities of the given system that have a negative real part and a vanishing imaginary part at a particular frequency. This was the goal of our optimization. The diagrams are to be understood as follows: As red line, we always plotted the real part of the magnetic susceptibility, as dashed, blue line, we plotted the imaginary part. To tailor our response, we started from Fig. 2.5 a) with the default parameters $|\Omega_{32}| = \gamma$, $r_1 = r_2 = r_3 = 0$, $\Delta_2 = 0$ and the decay rates given above.

From the default parameters in Fig. 2.5 a), we always change a single parameter in each step, denoted by the arrows. These are $|\Omega_{32}| = 5\alpha^{-2}\gamma$ in b), which gives us a Rabi splitting in the response on the frequency scale of the electric decay rates, and $r_3 = \alpha^{-2}\gamma$ in c), which introduces gain, i.e. negative values for the imaginary part, in a certain frequency range. Now, we can adapt the shape of the susceptibility to our wishes by changing the control field detuning Δ_2. E.g. in e), for $\Delta_2 = \alpha^{-2}\gamma$, we have a root of the imaginary part which lies very close to the minimum of the real part. However, the imaginary part is quite steep and only close to zero in a very small range (close to zero with respect to the real part). In contrast, in f), for $\Delta_2 = -3\alpha^{-2}\gamma$, we have a wider range of frequencies with small imaginary part around $\Delta_3 = 0$, but the root of the imaginary part is further away from the minimum of the real part. The real part minimum, however, coincides with an imaginary part of approximately the same size. This changes for the choice of $\Delta_2 = -\alpha^{-2}\gamma$ in g), where the minimum of the real part and a root of the imaginary part nearly coincide.

Also, another possibility is to set $r_1 = 2\alpha^{-2}\gamma$, $r_2 = 7\alpha^{-2}\gamma$ to go from Fig. 2.5 b) to d) which also has a root of the imaginary part and, at the same frequency, a negative real part.

Magnetic transitions

In a similar way, one can obtain suitable susceptibilities if $|1\rangle \rightarrow |3\rangle$ and $|2\rangle \rightarrow |3\rangle$ are magnetic dipole transitions. However, one has to adapt the values of the control field Rabi frequency, the incoherent pump rate and the control field detuning to the scale of magnetic dipole transitions. E.g., the control field Rabi frequency is now chosen to be $|\Omega_{32}| = 5\gamma$ without a factor α^{-1}. One then obtains Fig. 2.6 a) - d) with different parameter sets. These results are very similar to the previous case of electric transitions and correspond to Fig. 2.5 c), e) - g). Also, Fig. 2.6 e) has been obtained analogously to Fig. 2.5 d) and has similar parameters, only scaled by approximately a factor of α^{-2}.

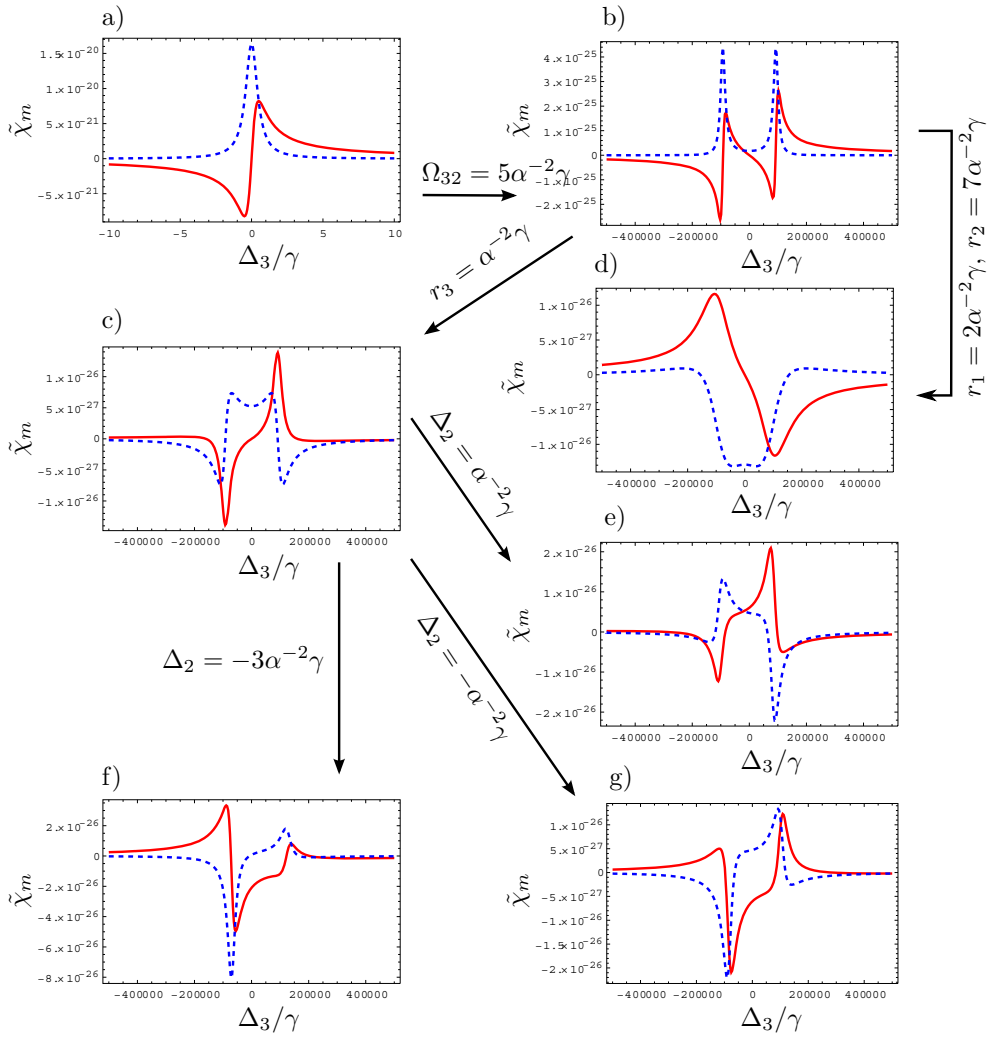

Figure 2.5: The above figures show the different steps to tailor the magnetic susceptibility in such a way that the imaginary part is small and the real part is negative. Figure a) shows the real (red, line) and the imaginary (blue, dashed) part of the susceptibility for the parameter set from which we start: $\gamma_1 = \alpha^{-2}\gamma$, $\gamma_2 = \alpha^{-2}\gamma$, $\gamma_3 = \gamma$, i.e. the transitions labelled 1 and 2 are electric dipole transitions, further $|\Omega_{32}| = \gamma$, $r_1 = r_2 = r_3 = 0$ and $\Delta_2 = 0$. Starting from a), we change only a single parameter in each step, which are: b) $|\Omega_{32}| = 5\alpha^{-2}\gamma$, c) $r_3 = \alpha^{-2}\gamma$. In Figs. e), f) and g), the parameters of c) have been used, but for non-zero values for the control field detuning Δ_2, respectively: e) $\Delta_2 = \alpha^{-2}\gamma$, f) $\Delta_2 = -3\alpha^{-2}\gamma$, g) $\Delta_2 = -\alpha^{-2}\gamma$. Also, from b) we can set $r_1 = 2\alpha^{-2}\gamma$, $r_2 = 7\alpha^{-2}\gamma$ to achieve d).

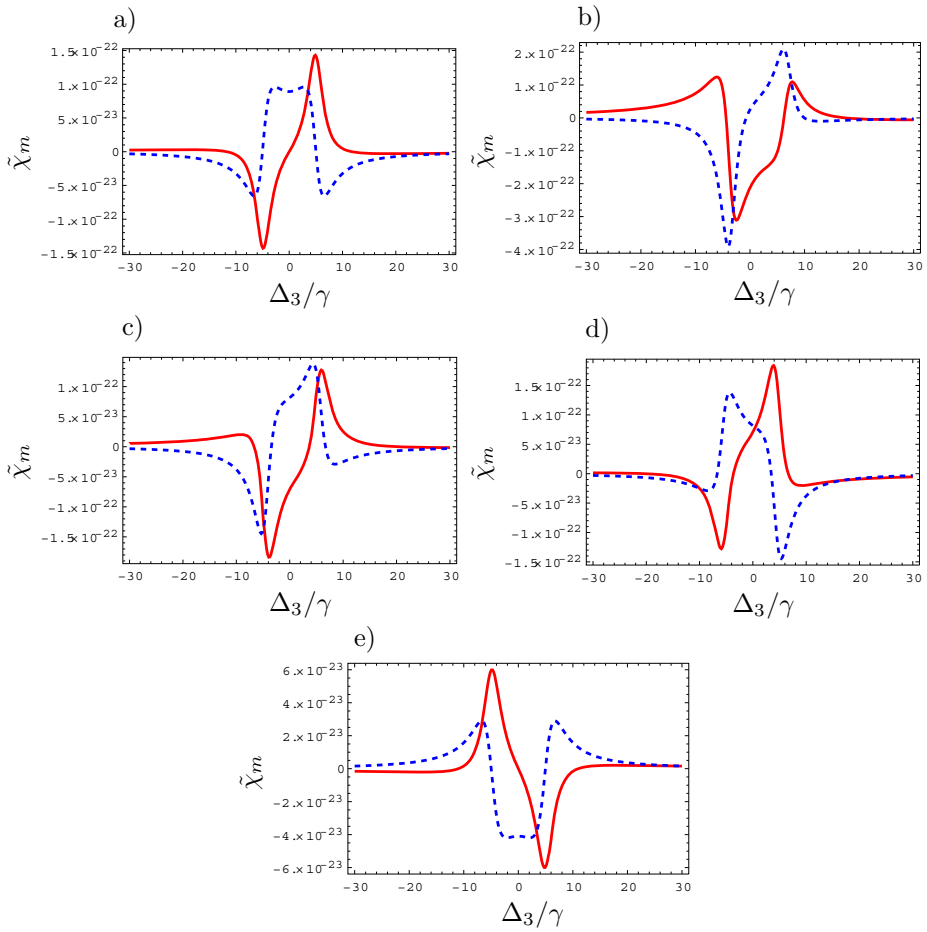

Figure 2.6: We plotted the magnetic susceptibility for the upper microwave scheme for different control field detunings Δ_2 and assumed the two non-probe transitions to be magnetic dipole transitions. The parameters common to plots a) - d) are $\gamma_1 = \gamma$, $\gamma_2 = \gamma$, $\gamma_3 = \gamma$, $|\Omega_{32}| = 5\gamma$, $r_3 = 2\gamma$ and $r_1 = r_2 = 0$. The respective values for the control field detuning are a) $\Delta_2 = 0$, b) $\Delta_2 = -3\gamma$, c) $\Delta_2 = -\gamma$ and d) $\Delta_2 = \gamma$. In e), we chose $\gamma_1 = \gamma$, $\gamma_2 = \gamma$, $\gamma_3 = \gamma$, $|\Omega_{32}| = 5\gamma$, $\Delta_2 = 0$, $r_1 = 2\gamma$, $r_2 = \gamma$ and $r_3 = 0$.

Nitrogen

Let us now consider a real three-level system. The following states of atomic nitrogen, which are the three lowest-lying ones energy-wise, built up a three-level system [27]:

$$|1\rangle = 2s^2 2p^3\ {}^4S^\circ_{3/2}\,, \tag{2.45}$$
$$|2\rangle = 2s^2 2p^3\ {}^2D^\circ_{5/2}\,, \tag{2.46}$$
$$|3\rangle = 2s^2 2p^3\ {}^2D^\circ_{3/2}\,. \tag{2.47}$$

The absolute decay rates are

$$\gamma_1 = \underbrace{1.90 \cdot 10^{-5} s^{-1}}_{M1} + \underbrace{3.60 \cdot 10^{-6} s^{-1}}_{E2}\,, \tag{2.48a}$$
$$\gamma_2 = \underbrace{1.07 \cdot 10^{-8} s^{-1}}_{M1} + \underbrace{3.20 \cdot 10^{-21} s^{-1}}_{E2}\,, \tag{2.48b}$$
$$\gamma_3 = \underbrace{2.45 \cdot 10^{-7} s^{-1}}_{M1} + \underbrace{5.52 \cdot 10^{-6} s^{-1}}_{E2}\,. \tag{2.48c}$$

and the vacuum Ritz wavelength (calculated from the difference of the inverse wave numbers of the $|2\rangle$ and $|1\rangle$) of the probe transition is

$$\lambda = 520.1705\,\mathrm{nm}\,. \tag{2.49}$$

In Fig. 2.7, we plotted the magnetic susceptibility for different parameters. First, we use the following values for nitrogen $\gamma_1 = 3.92\gamma$, $\gamma_2 = 1.86 \cdot 10^{-3}\gamma$, $\gamma_3 = \gamma$ for the decay rates and $\lambda = 520.17\,\mathrm{nm}$ for the probe transitions wavelength in all plots. The other parameters are given by: a) $|\Omega_{32}| = 10\gamma$, $\Delta_2 = 0$, $r_3 = 5\gamma$, $r_1 = r_2 = 0$, b) $|\Omega_{32}| = 10\gamma$, $\Delta_2 = -5\gamma$, $r_3 = 5\gamma$, $r_1 = r_2 = 0$, c) $|\Omega_{32}| = 10\gamma$, $\Delta_2 = -\gamma$, $r_3 = 5\gamma$, $r_1 = r_2 = 0$, d) $|\Omega_{32}| = 10\gamma$, $\Delta_2 = \gamma$, $r_3 = 5\gamma$, $r_1 = r_2 = 0$ and e) $|\Omega_{32}| = 10\gamma$, $\Delta_2 = 10\gamma$, $r_1 = 6\gamma$, $r_2 = r_3 = 0$.

Note that we used the mentioned decay rates, i.e. the sums of Eq. (2.48), and plugged them into the probe transition coherence $\tilde{\varrho}_{21}$. However, to calculate the magnetic moment of the probe transition according to Eq. (2.34), we inserted only the M1 part of γ_3 given in Eq. (2.48) for γ_α, since the E2 part is not connected to the magnetic moment. Taking the sums of the decay rates as given in Eq. (2.48) for the coherence includes a possible error source: The two decay rates, M1 and E2, do not necessarily simply add up due to interference between the two contributions. However, this interference is difficult to quantify. Therefore, we use the straightforward sums, which will still give us the right order of magnitude, since the M1- and the E2-values differ by approximately an order of magnitude.

Note that the distinction between the part of the decay rate that contributes to the magnetic moment (M1) and the total decay rate is not necessary when $|2\rangle \rightarrow |3\rangle$

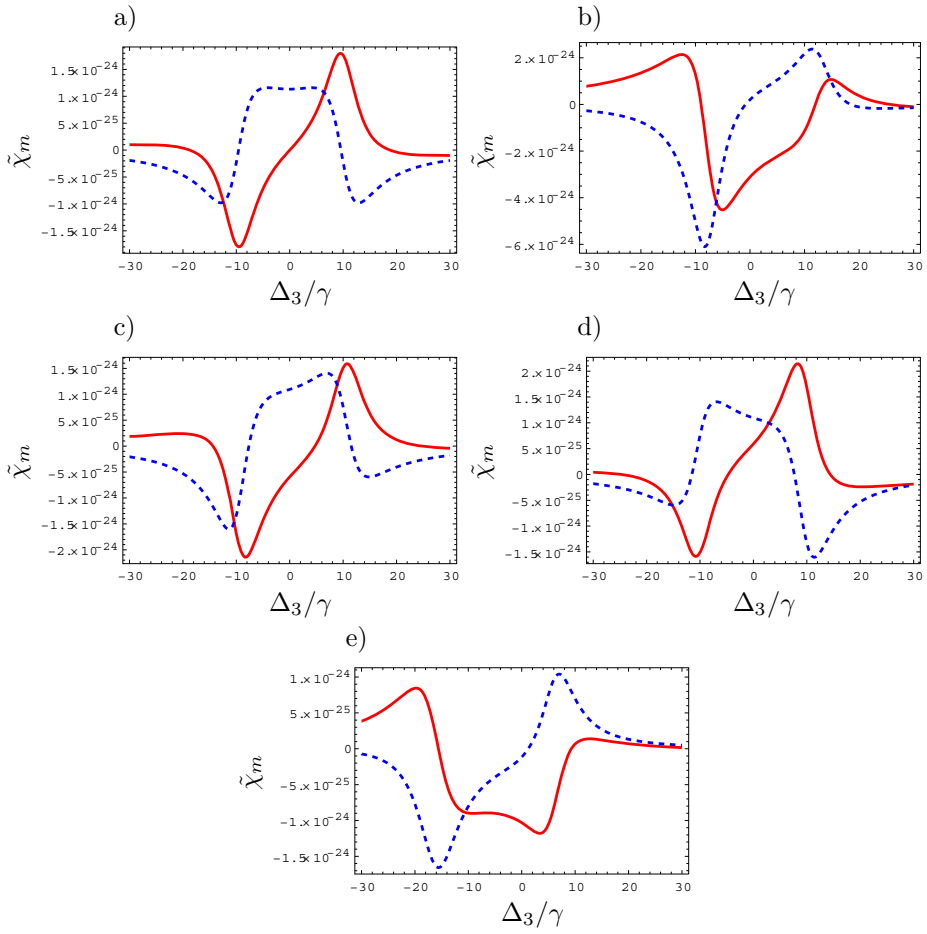

Figure 2.7: Here, we show the magnetic susceptibility of nitrogen in upper microwave configuration. We used the nitrogen parameters [27] $\gamma_1 = 3.92\gamma$, $\gamma_2 = 1.86 \cdot 10^{-3}\gamma$, $\gamma_3 = \gamma$ and $\lambda = 520.1705\,\text{nm}$ for the probe transitions wavelength in all plots. The other parameters are: a) $|\Omega_{32}| = 10\gamma$, $\Delta_2 = 0$, $r_3 = 5\gamma$, $r_1 = r_2 = 0$, b) $|\Omega_{32}| = 10\gamma$, $\Delta_2 = -5\gamma$, $r_3 = 5\gamma$, $r_1 = r_2 = 0$, c) $|\Omega_{32}| = 10\gamma$, $\Delta_2 = -\gamma$, $r_3 = 5\gamma$, $r_1 = r_2 = 0$, d) $|\Omega_{32}| = 10\gamma$, $\Delta_2 = \gamma$, $r_3 = 5\gamma$, $r_1 = r_2 = 0$ and e) $|\Omega_{32}| = 10\gamma$, $\Delta_2 = 10\gamma$, $r_1 = 6\gamma$, $r_2 = r_3 = 0$.

is the probe transition, which is the case in the lower microwave and the lambda scheme. There, the E2 part of γ_2 is negligible compared to the M1 part, since it is 13 orders of magnitude smaller.

The plots a) - d) in Fig. 2.7 correspond to the plots with the same label in Fig. 2.6 and to c), e) - g) in Fig. 2.5. Due to the different decay rates, one simply has to adjust the other parameters, i.e. the incoherent pump rates, the control field Rabi frequency and the control field detuning to achieve similar shapes in the nitrogen

system. The plot e) in Fig. 2.7 is similar to Fig. 2.6 e) and to Fig. 2.5 d) but for the non-zero detuning Δ_2 and the vanishing pump rate r_2.

Summary

In Figs. 2.5, 2.6 and 2.7 we achieved similar shapes for the magnetic susceptibility for analogous parameters. Each time, we arrived at optimized susceptibilities by increasing the control field Rabi frequency until two peaks appear in the imaginary part of the magnetic susceptibility due to Rabi splitting. The scale on which this happens is given by the incoherent decay rate on the transition of the control field. Then, one can change between absorptive and amplifying behavior by increasing r_3.

Another way to optimize the susceptibility was to turn on r_1 (together with the control field) — and possibly r_2 — instead of r_3. This has been done in Figs. 2.5 d), 2.6 e) and 2.7 e).

When increasing r_1, one introduces more and more gain on the probe transition. For particular system parameters, there is a value of r_1 for which the susceptibility vanishes for all frequencies. This is the case for $\gamma_1 = \gamma_2 = \gamma_3 = \gamma$, $r_2 = r_3 = 0$ and $r_1 = 2\gamma_2 = 2\gamma_3$. In this case, the population pumped by r_1 to $|3\rangle$ immediately decays to the ground level through the two decay channels - i.e. directly or via level $|2\rangle$ - at the same rate as it is pumped to level $|3\rangle$. Therefore, all populations in zeroth order of the probe field are equal and according to Eq. (2.35) the coherence $\tilde{\varrho}_{21}$ and thus the magnetic susceptibility vanishes for all frequencies. However, switching on r_2 causes the magnetic susceptibility to be non-zero again (see fig. 2.6 e)).

For any other case, the magnetic susceptibility has a suitable shape for values of r_1 and r_3, respectively, that lie between values that yield a negative imaginary part at all frequencies and values that yield a positive imaginary part at all frequencies. In other words, we exploit the fact that the absorptive behavior of the system changes with r_1 and r_3. At these particular values for r_1 and r_3, respectively, we have a negative imaginary part at some frequencies, and at other frequencies we have a positive imaginary part. Therefore, the imaginary part has a root. From this shape, one can achieve suitable susceptibilities by introducing an asymmetry through a change of the control field detuning Δ_2.

For simplicity, in the following we will refer to shapes as in Fig. 2.5 c) as M-shapes due to the form of the imaginary part. Consequently, Fig. 2.6 e) can be said to have a W-shape.

2.3.2 Lower microwave scheme

Again, we begin with solving the equations of motion explicitly for the lower microwave scheme shown in Fig. 2.8. Neglecting second and higher order terms in the probe field Rabi frequency Ω_{32}, we obtain for the coherence of the probe transition

$$\tilde{\varrho}_{32} = -\Omega_{32}\frac{2i\left[4\left(\tilde{\varrho}_{22}^{(0)}-\tilde{\varrho}_{11}^{(0)}\right)|\Omega_{12}|^2+\left(\tilde{\varrho}_{33}^{(0)}-\tilde{\varrho}_{22}^{(0)}\right)(\gamma_3+r_{123}+2i\Delta_3)\,C_0\right]}{(r_{123}+\gamma_3+2i\Delta_3)\left[4|\Omega_{12}|^2+(\gamma_{123}+r_2+2i\Delta_2)\,C_0\right]}\,, \quad (2.50)$$

where

$$C_0 = r_{13}+\gamma_{12}+2i\Delta_2+2i\Delta_3\,. \quad (2.51)$$

Also,

$$\tilde{\varrho}_{11}^{(0)} = \frac{4|\Omega_{12}|^2\gamma_{12}\,(\gamma_3+r_{123})+(r_2\gamma_1+\gamma_{12}\gamma_3)\,C_1}{C_3+C_2C_1}\,, \quad (2.52)$$

$$\tilde{\varrho}_{22}^{(0)} = \frac{4|\Omega_{12}|^2\gamma_{12}\,(\gamma_3+r_{123})+(r_1\gamma_2+\gamma_{12}r_3)\,C_1}{C_3+C_2C_1}\,, \quad (2.53)$$

$$\tilde{\varrho}_{33}^{(0)} = \frac{4|\Omega_{12}|^2 r_{12}\,(\gamma_3+r_{123})+[r_2r_3+r_1\,(r_2+\gamma_3)]\,C_1}{C_3+C_2C_1}\,, \quad (2.54)$$

are the populations of the three levels in zeroth order of the probe field. Again, we have chosen to abbreviate sums of quantities that differ only by the index, e.g. $\gamma_{123}=\gamma_1+\gamma_2+\gamma_3$ or $r_{23}=r_2+r_3$. Moreover, we defined

$$C_1 = \gamma_3^2+r_1^2+r_2^2+r_3^2+2\gamma_3r_{123}+2r_3r_{12}+2r_1r_2+4\Delta_3^2\,, \quad (2.55)$$

$$C_2 = r_2\,(r_3+\gamma_1)+\gamma_{12}\,(r_3+\gamma_3)+r_1\,(r_2+\gamma_{23})\,, \quad (2.56)$$

$$C_3 = 4|\Omega_{12}|^2\,(2\gamma_{12}+r_{12})\,(\gamma_3+r_{123})\,. \quad (2.57)$$

Electric transitions

In the lower microwave scheme, it is possible to obtain shapes of the susceptibility that are very similar to the ones in the upper microwave system of the previous chapter. Only the meanings of transitions $|1\rangle \rightarrow |2\rangle$, labelled 3, and $|2\rangle \rightarrow |3\rangle$, labelled 2, have been switched: The transition labelled 2 now is the probe transition,

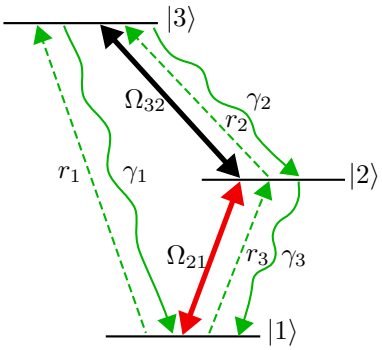

Figure 2.8: The lower microwave scheme includes a control field Ω_{21} (red, two arrowheads) coupling to transition $|1\rangle \rightarrow |2\rangle$, a probe field Ω_{32} (black, two arrowheads) coupling to the magnetic probe transition $|2\rangle \rightarrow |3\rangle$, incoherent decay rates $\gamma_\alpha, \alpha \in \{1,2,3\}$ (wiggly green arrows) and incoherent pump rates $r_\alpha, \alpha \in \{1,2,3\}$ (straight, dashed green arrows) on each transition.

while transition 3 couples to the control field. Therefore, it is possible to obtain M-shapes as in the upper microwave system by choosing an appropriate value for r_2 — instead of r_3 in the upper microwave system. Also, as before, one can also obtain good results by setting r_1 to an appropriate, non-zero value.

For $\gamma_1 = \gamma_3 = \alpha^{-2}\gamma$, $\gamma_2 = \gamma$, i.e. only electric transitions, $\Delta_3 = 0$ and $|\Omega_{21}| = 5\alpha^{-2}\gamma$ and appropriate values for r_1 and r_2, we obtain the probe transition coherences shown in Fig. 2.9.

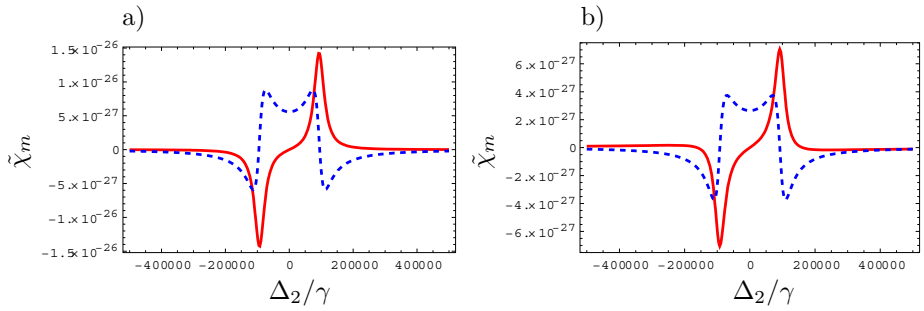

Figure 2.9: We plotted the relevant coherences for two sets of parameters in the lower microwave system: In both cases, we have $\gamma_1 = \gamma_3 = \alpha^{-2}\gamma$, $\gamma_2 = \gamma$, $\Delta_3 = 0$ and $|\Omega_{21}| = 5\alpha^{-2}\gamma$. In a), the pump rates are $r_1 = r_3 = 0$ and $r_2 = \alpha^{-2}\gamma$, in b) $r_2 = r_3 = 0$ and $r_1 = 2\alpha^{-2}\gamma$.

Magnetic transitions

Also for $\gamma_1 = \gamma_3 = \gamma_2 = \gamma$, we obtain suitable M-shapes in a similar way as before, i.e. by setting r_1 and r_2 to the right value. However, since for $r_1 = 2\gamma$ our susceptibility vanishes for the same reasons as explained in Sec. 2.3.1, one then has to set $r_3 = \gamma$ again to achieve the desired susceptibility.

The resulting shapes of the probe transition coherence are shown in Fig. 2.10. We chose $|\Omega_{21}| = 5\gamma$ and suitable values for the incoherent pump rates (see caption).

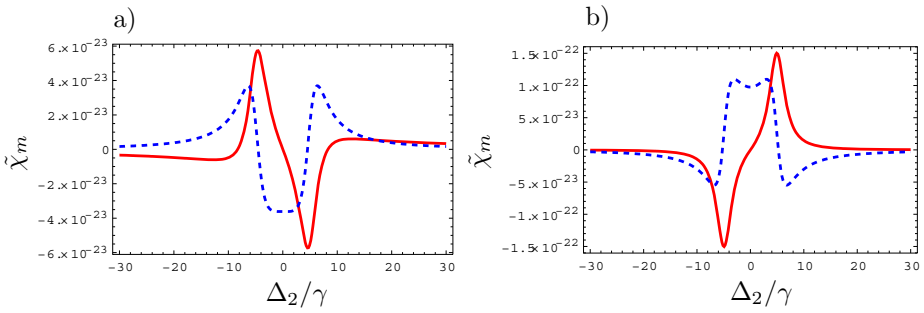

Figure 2.10: We plotted the relevant coherences for two sets of parameters in the lower microwave system: In both cases, we have $\gamma_1 = \gamma_2 = \gamma_3 = \gamma$, $\Delta_3 = 0$ and $|\Omega_{21}| = 5\gamma$. In a), the pump rates are $r_2 = 0$, $r_1 = 2\gamma$ and $r_3 = \gamma$, in b) $r_1 = r_3 = 0$ and $r_2 = 2\gamma$.

Nitrogen

Again, we examine the corresponding results in the real three-level system nitrogen. Here, it is less adequate to call it a "lower microwave system", since the microwave transition is $|2\rangle \rightarrow |3\rangle$. However, the control and the probe field can be applied in the same way as in the previous lower microwave systems and therefore we will stick to the term "lower microwave system".

Although we use the same decay rates as in the upper microwave configuration for nitrogen, we now normalize all parameters to the decay rate of the probe transition $|2\rangle \rightarrow |3\rangle$, i.e. $\gamma_2 = \gamma$. Therefore, we have $\gamma_1 = 2.11 \cdot 10^3 \gamma$ and $\gamma_3 = 5.39 \cdot 10^2 \gamma$. Since the probe field now couples to transition $|2\rangle \rightarrow |3\rangle$, the probe transition wavelength is $\lambda = 1147.71\,\mu\text{m}$ [27]. In the plots of Fig. 2.11, we used $\Delta_3 = 0$ and $|\Omega_{21}| = 5 \cdot 10^3 \gamma$. In a), the incoherent pump rates were set to $r_1 = 2 \cdot 10^3 \gamma$ and $r_2 = r_3 = 0$. In b), we chose $r_2 = 2 \cdot 10^3 \gamma$ and $r_1 = r_3 = 0$.

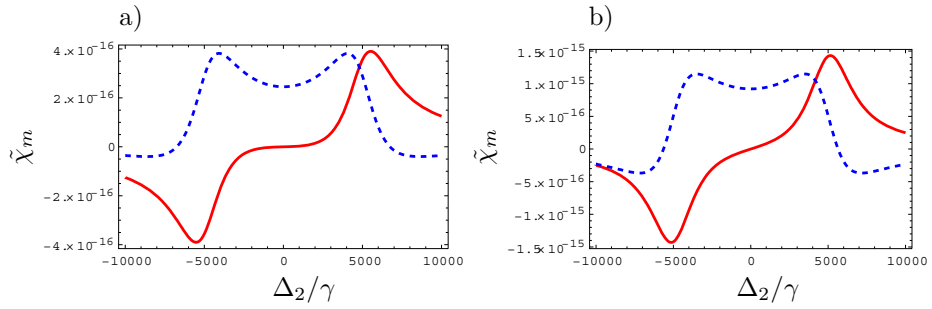

Figure 2.11: We show two suitable susceptibilities for nitrogen in lower microwave configuration. The parameters are $\gamma_2 = \gamma$, $\gamma_1 = 2.11 \cdot 10^3\gamma$, $\gamma_3 = 5.39 \cdot 10^2\gamma$, $\lambda = 1147.71$ µm, $\Delta_3 = 0$, $|\Omega_{21}| = 5 \cdot 10^3\gamma$ and $r_1 = 2 \cdot 10^3\gamma$, $r_2 = r_3 = 0$ in a) and $r_2 = 2 \cdot 10^3\gamma$, $r_1 = r_3 = 0$ in b).

2.3.3 Lambda system

Let us now consider the lambda system shown in Fig. 2.12. For the coherence of the probe transition, we find

$$\tilde{\varrho}_{32} = -\Omega_{32}\frac{2i\left[-4\left(\tilde{\varrho}_{33}^{(0)} - \tilde{\varrho}_{11}^{(0)}\right)|\Omega_{13}|^2 + \left(\tilde{\varrho}_{33}^{(0)} - \tilde{\varrho}_{22}^{(0)}\right)(\gamma_{12} + r_{13} - 2i\Delta_1)\,D_0\right]}{(r_{13} + \gamma_{12} - 2i\Delta_1)\left[4|\Omega_{13}|^2 + (\gamma_{123} + r_2 + 2i\Delta_2)\,D_0\right]}\,, \tag{2.58}$$

where

$$D_0 = r_{123} + \gamma_3 - 2i\Delta_1 + 2i\Delta_2\,. \tag{2.59}$$

Moreover,

$$\tilde{\varrho}_{11}^{(0)} = \frac{4|\Omega_{13}|^2(\gamma_3 + r_2)(\gamma_{12} + r_{13}) + (r_2\gamma_1 + \gamma_{12}\gamma_3)\,D_1}{D_3 + D_2D_1}\,, \tag{2.60}$$

$$\tilde{\varrho}_{22}^{(0)} = \frac{4|\Omega_{13}|^2(\gamma_2 + r_3)(\gamma_{12} + r_{13}) + (r_1\gamma_2 + \gamma_{12}r_3)\,D_1}{D_3 + D_2D_1}\,, \tag{2.61}$$

$$\tilde{\varrho}_{33}^{(0)} = \frac{4|\Omega_{13}|^2(\gamma_3 + r_2)(\gamma_{12} + r_{13}) + [r_2r_3 + r_1(r_2 + \gamma_3)]\,D_1}{D_3 + D_2D_1}\,, \tag{2.62}$$

are the populations of the three levels in zeroth order of the probe field. Here, quantities that are indexed with multiple digits are defined to be the sum of the corresponding single-indexed quantities, e.g. $\gamma_{123} = \gamma_1 + \gamma_2 + \gamma_3$ or $r_{23} = r_2 + r_3$. Also, we defined

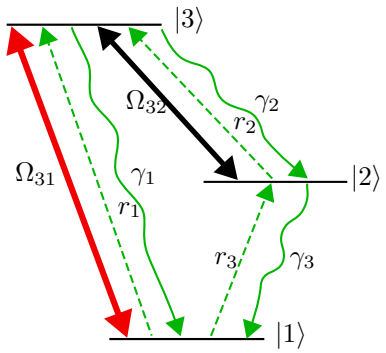

Figure 2.12: The lambda scheme includes a control field Ω_{31} (red, two arrowheads) coupling to transition $|1\rangle \rightarrow |3\rangle$, a probe field Ω_{32} (black, two arrowheads) coupling to the magnetic probe transition $|2\rangle \rightarrow |3\rangle$, incoherent decay rates $\gamma_\alpha, \alpha \in \{1,2,3\}$ (wiggly green arrows) and incoherent pump rates $r_\alpha, \alpha \in \{1,2,3\}$ (straight, dashed green arrows) on each transition.

$$D_1 = \gamma_1^2 + \gamma_2^2 + r_1^2 + r_3^2 + 2\gamma_1\gamma_2 + 2\gamma_{12}r_{13} + 2r_1r_3 + 4\Delta_1^2 \,, \tag{2.63}$$

$$D_2 = r_2\left(r_3 + \gamma_1\right) + \gamma_{12}\left(r_3 + \gamma_3\right) + r_1\left(r_2 + \gamma_{23}\right) \,, \tag{2.64}$$

$$D_3 = 4|\Omega_{13}|^2\left(\gamma_{12} + r_{13}\right)\left(2r_2 + r_3 + 2\gamma_3 + \gamma_2\right) \,. \tag{2.65}$$

Electric transitions

First, we assume transitions $|1\rangle \rightarrow |3\rangle$ and $|1\rangle \rightarrow |2\rangle$ to be electric dipole transitions, i.e. $\gamma_1 = \alpha^{-2}\gamma$ and $\gamma_3 = \alpha^{-2}\gamma$. As before, the probe transition $|2\rangle \rightarrow |3\rangle$ is magnetic and therefore $\gamma_2 = \gamma$.

Fig. 2.13 a) shows the magnetic susceptibility for $\Delta_1 = 0$, $r_1 = r_2 = r_3 = 0$ and $|\Omega_{31}| = 5\alpha^{-2}\gamma$. One can see that the system is amplifying, since, on one hand, the control field shifts population to level $|3\rangle$ and, on the other hand, the population on $|2\rangle$ quickly decays to the ground level due to $r_3 = 0$. This causes a population inversion between the two levels of the probe transition and therefore amplification.

Switching on the pump rates r_1 and r_2, respectively, washes out the Rabi splitting due to the control field, but does not introduce gain, as can be seen in Figs. 2.13 c) and d). However, turning on the pump rate r_3 decreases the population inversion between $|2\rangle$ and $|3\rangle$ and therefore leads to more and more absorption on the probe transition. For a certain value, $r_3 = \alpha^{-2}\gamma$, we obtain the desired W-shape of the imaginary part of the magnetic susceptibility.

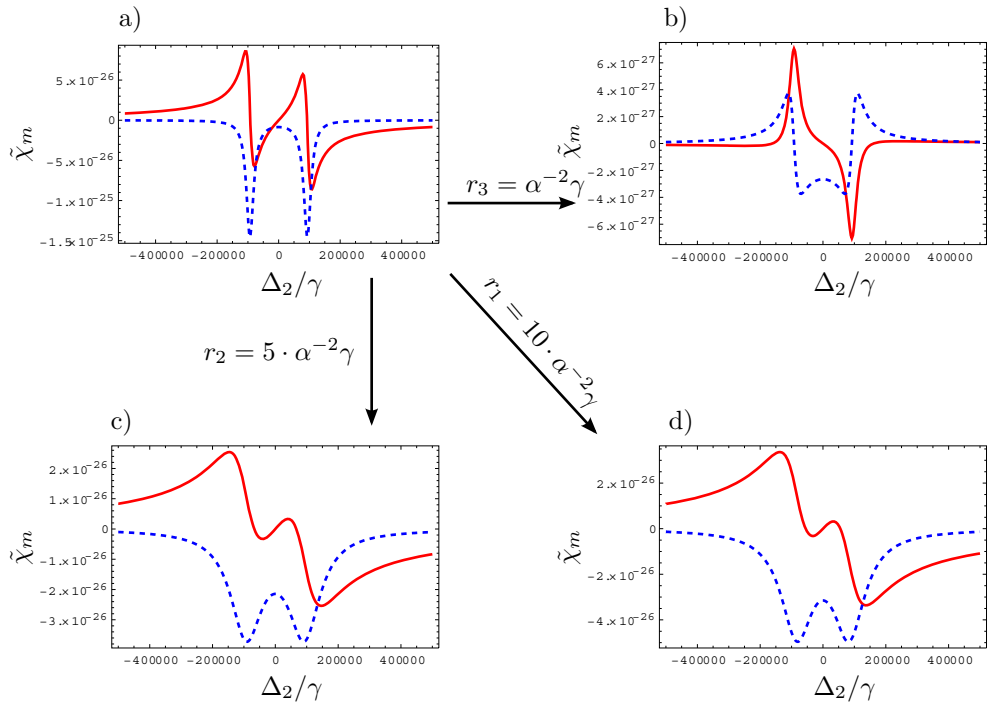

Figure 2.13: We choose the parameters $\gamma_1 = \alpha^{-2}\gamma$, $\gamma_3 = \alpha^{-2}\gamma$, $\gamma_2 = \gamma$, $\Delta_1 = 0$, $r_1 = r_2 = r_3 = 0$ and $|\Omega_{31}| = 5\alpha^{-2}\gamma$ for a lambda-type system. For vanishing incoherent pump rates, we obtain the magnetic susceptibility in a). A sign change of the imaginary part of the susceptibility can be accomplished by increasing r_3 and for $r_3 = \alpha^{-2}\gamma$, we have b). c) and d) show the susceptibility for cases in which another incoherent pump rate is non-zero, namely $r_2 = \alpha^{-2}\gamma$ and $r_1 = 10\alpha^{-2}\gamma$, respectively.

Magnetic transitions

If we assume only magnetic transitions, i.e. $\gamma_1 = \gamma_2 = \gamma_3 = \gamma$, we obtain the plots of Fig. 2.13. All subplots are drawn with the parameters $|\Omega_{31}| = 5\gamma$ and $\Delta_1 = 0$. a) shows $r_1 = r_2 = r_3 = 0$, whereas in the other subplots we chose one pump rate to be non-zero, in particular $r_3 = \gamma/2$ in b), $r_2 = 5\gamma$ in c) and $r_1 = 3\gamma$ in d).

For the parameters chosen in a), i.e. for equal decay rates and zero pump rates, we obtain a negative imaginary part for small probe field detunings. Increasing r_3 yields absorption (see b)), since $|2\rangle$ has a higher population then. Increasing r_2 yields a higher population on $|3\rangle$ and therefore amplification. In cases a) and d), we obtain M- and W-shapes, respectively.

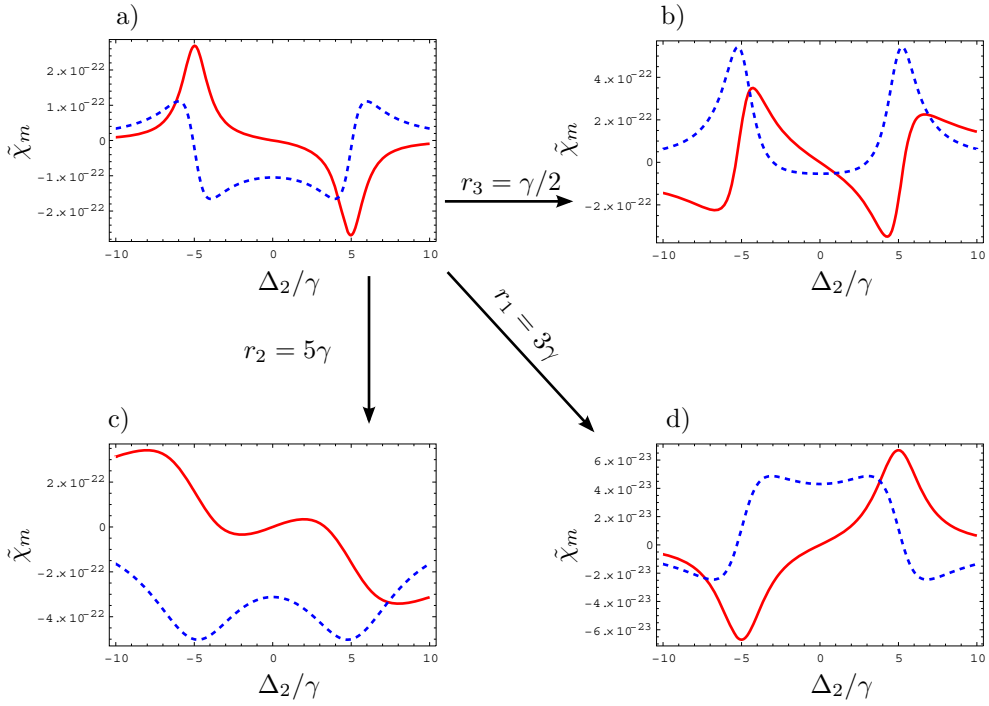

Figure 2.14: In the shown plots for the magnetic susceptibility for the lambda system, we assumed $\gamma_1 = \gamma_2 = \gamma_3 = \gamma$, $|\Omega_{31}| = 5\gamma$ and $\Delta_1 = 0$. In a), we have $r_1 = r_2 = r_3 = 0$, whereas the other subplots show the cases of one non-zero pump rate, namely $r_3 = \gamma/2$ in a), $r_2 = 5\gamma$ in b) and $r_1 = 3\gamma$ in c).

Nitrogen

To examine nitrogen in lambda configuration, we have to use exactly the same parameters as for the lower microwave configuration. They are $\gamma_2 = \gamma$, $\gamma_1 = 2.11 \cdot 10^3\gamma$, $\gamma_3 = 5.39 \cdot 10^2\gamma$ and $\lambda = 1147.71$ µm. Setting $\Delta_3 = 0$, $|\Omega_{13}| = 5 \cdot 10^3\gamma$, $r_3 = 5 \cdot 10^2\gamma$ and $r_1 = r_2 = 0$ yields the magnetic susceptibility plotted in Fig. 2.15. A choice of another (or no) incoherent pump rate being non-zero instead does not yield similar shapes, since r_3 is the only pump rate that can introduce gain. Also, for all pump rates being zero the system is amplifying.

2.4 Conclusion

In all examined systems, it was possible to achieve a shape for the magnetic susceptibility for which, at a certain frequency, the imaginary part vanished and the real part became negative. This form is one candidate for negative refraction. Also,

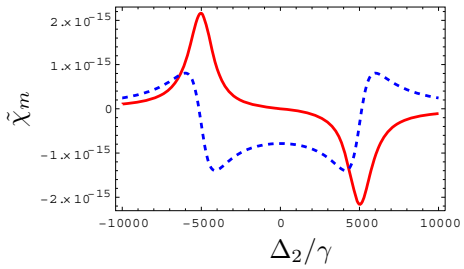

Figure 2.15: We show the magnetic susceptibilities for nitrogen in lambda configuration for the following parameters: $\gamma_2 = \gamma$, $\gamma_1 = 2.11 \cdot 10^3\gamma$, $\gamma_3 = 5.39 \cdot 10^2\gamma$ and $\lambda = 1147.71$ µm, moreover $\Delta_3 = 0$, $|\Omega_{13}| = 5 \cdot 10^3\gamma$, $r_3 = 5 \cdot 10^2\gamma$ and $r_1 = r_2 = 0$.

the shape of the magnetic susceptibility looked similar in the various systems. It was created by a Rabi splitting and the use of an incoherent pump rate that could change the absorptive behavior of the system.

In all considered systems, we obtained by far the largest absolute value of the magnetic suceptibility for the nitrogen-like lower microwave and the nitrogen-like lambda system. However, this is due to the fact that, in these systems, the probe transition had a wavelength in the microwave range instead of an optical wavelength. Therefore, the square of the magnetic dipole moment $\mu_{i_0 j_0}$ in Eq. (2.18) was larger by a factor of approximately 10^10 (see Eq. (2.34). Since we are interested in negative refraction at optical frequencies, these two systems will not be considered further.

Apart from these, the absolute value of the susceptibility is the largest for the systems with only magnetic transitions. The lambda system, the upper and the lower microwave system showed magnetic susceptibilities of roughly the same magnitude ($|\tilde{\chi}_m| \approx 10^{-22}...10^{-23}$) for these types of transitions. The nitrogen-like upper microwave system yielded absolute values of $|\tilde{\chi}_m| \approx 10^{-24}$. A calculation of the susceptibility of the nitrogen-like lower microwave and the nitrogen-like lambda system for an optical probe transition frequency instead of the microwave frequency results in values $|\tilde{\chi}_m| \approx 10^{-25}$. This is nearly the same order of magnitude as the upper microwave system with nitrogen parameters. Finally, the three considered systems with electric transitions besides the probe transition show susceptibilities with $|\tilde{\chi}_m| \approx 10^{-26}...10^{-27}$.

In Sec. 3.6 we will see that these orders of magnitude are also valid for the so-called closed-loop system considered there, except for the nitrogen-like system for which we obtain $|\tilde{\chi}_m| \approx 10^{-22}...10^{-23}$ there.

Since the actual shape of the susceptibilities in the different system was very similar and the magnitude of the susceptibilities differed mainly between the different types of transitions and not the different types of field configurations, this seems to imply

that the values of the decay rates play a more important role for the size of the susceptibility than the actual configuration of probe and control fields. In our systems, the more similar the decay rates are, the larger the susceptibilities become. E.g., in the case of equal decay rates — $\gamma_1 = \gamma_2 = \gamma_3$, we obtain the biggest susceptibility. This can possibly be explained by the fact that, in our systems, we have a magnetic probe transition, i.e. a probe transition with a small decay rate. If the other transitions now have a much larger decay rate, the population will mostly decay through these other transitions and the response on the probe transition will be smaller.

For these reasons, a system with only magnetic dipole transitions yields the best results in our calculations. Also, the nitrogen-like system is a real, existing system and also has a reasonably big magnetic susceptibility. Therefore, in Sec. 4.2.2, we will consider an upper microwave system with only magnetic transitions and an upper microwave system with nitrogen parameters for the magnetically coupling species.

In Sec. 4.2.3, this examination will be completed by the nitrogen-like closed-loop system of Sec. 3.6 which also yields — as we will see — comparably high absolute values for the magnetic susceptibility.

Chapter 3

Enhancement of the magnetic response

3.1 Introduction

Until now, focused on optimizing the magnetic susceptibility and thus the permeability towards the values depicted in Fig. 2.1 c), i.e. a small imaginary part and a negative real part. Here, "small" has to be seen with respect to the absolute value of the real part. However, not only the ratio between imaginary and real part of the magnetic response is of importance, but it is also crucial that we obtain both a magnetic and an electric response of considerable size at the probe field frequency. This is hampered by the fact that usually the coupling of the magnetic component of a probe laser field to a magnetic dipole transition is strongly suppressed when compared to the coupling of the electric probe field component to an electric dipole transition. A simple order-of-magnitude estimate shows that the suppression factor is proportional to two powers of the finestructure constant, $\alpha^2 \sim 137^{-2}$.

Therefore, it is desirable to enhance the magnetic response. In the literature, a number of schemes that allow to achieve a high positive index of refraction with small absorption have been proposed. They are based on a suitable modification of the electric response of the medium (see, e.g., [20]). The enhancement, however, is typically too small such that a direct transfer of these ideas to magnetic transitions is not straightforward. Thus, the schemes suggested so far for negative refraction rely on a different mechanism that is related to an enhancement via chirality [22, 15, 17, 18]. The medium is such that the magnetic response is not only determined by the magnetic probe field component, but by both the electric and the magnetic component and analogously for the electric response. A first interpretation for the case of atomic systems has been given in [15], in which a magnetic dipole moment induced by electric fields was derived, but the coupling of the magnetic probe field

component to the atomic system was not considered. Also, it focuses on a certain resonance case for the applied fields and the employed level structure. Thus, the system considered there only allows for enhancement at a single frequency, while an enhancement at a range of probe field frequencies was reported in subsequent work [17, 18]. Thus better insight is desirable, not least since it might lead to further enhancement of the magnetic response which would significantly simplify the theoretical and experimental study of negative refraction in atomic gases.

Motivated by this, here we study in detail the enhancement mechanism that is at the heart of current schemes to achieve negative refraction in atomic gases. For this, we revisit the three-level system studied in [15], where one transition is driven by a coherent control field and the other two transitions couple to the magnetic and electric component of a probe field (see Fig. 3.1). In contrast to previous studies, we apply a time-dependent analysis of the medium response that enables us to directly identify the various physical processes contributing to the medium response. These results are compared to a reference system that is obtained by replacing the coherent driving field by an incoherent pumping field. We find that the enhancement of the magnetic response occurs, since the used level scheme is a so-called closed-loop medium. In such systems, the laser fields applied are such that they form a closed interaction loop. We identify a scattering of the coupling field and of the electric probe field into the magnetic probe field component as the mechanism responsible for the enhancement of the response and provide conditions for this process to take place. It is found that the so-called multiphoton resonance condition must be fulfilled for the enhancement to be present. In the studied three-level system, the condition is satisfied only at a single probe field frequency. But in larger level schemes, the laser fields can be applied in such a way that the enhancement works at arbitrary frequencies of the probe field.

This section is organized as follows: In Sec. 3.2, we present our model systems and derive the equations of motion as well as expressions for the medium response coefficients. In Sec. 3.3, we solve the equations of motion, both in the time-dependent case for the closed-loop configuration, for the time-independent case at multiphoton resonance and in the incoherently pumped reference system. Using these results, in Sec. 3.4 we compare the different systems, identify the enhancement mechanism and finally quantify it. Sec. 3.5 discusses and summarizes these results. Then, in Sec. 3.6, we investigate a system that can be obtained from the considered closed-loop system by replacing the electric probe field component by an electric control field. We optimize this system towards a small imaginary part and a negative real part of the index of refraction at a certain frequency to use it as one part of a negatively refracting system in Sec. 4.

3.2 Theoretical considerations

3.2.1 Model

We start by writing down the applied electromagnetic fields that we show in Fig. 3.1. In contrast to the derivation of Sec. 2.1, we now also have to take into account the electric probe field component, as it also couples to our systems. Since we treat both systems semi-classically, we have

$$\begin{aligned}\vec{E}(\vec{r},t) = \quad & \vec{E}_p(\vec{r})e^{i\phi}e^{-i\omega_p t} + \vec{E}_c(\vec{r})e^{i\psi}e^{-i\omega_c t} \\ & + \text{c.c.}\,, \qquad (3.1a)\\ \vec{B}(\vec{r},t) = \quad & \vec{B}_p(\vec{r})e^{i\phi}e^{-i\omega_p t} + \vec{B}_c(\vec{r})e^{i\psi}e^{-i\omega_c t} \\ & + \text{c.c.}\,, \qquad (3.1b)\end{aligned}$$

where the subindex p [c] refers to the probe [control] field.

We use the same notation as in Sec. 2.1 here, namely $\vec{E}_p(\vec{r}) = \mathcal{E}_p\vec{e}_p e^{i\vec{k}_p\vec{r}}$, where $\mathcal{E}_p$ is the electric field amplitude, $\vec{e}_p$ the unit polarization vector of the electric component of the probe field, $\vec{k}_p$ is the probe field's wave vector, ω_p its frequency and ϕ its absolute phase. Analogously, we have defined $\vec{E}_c(\vec{r}) = \mathcal{E}_c\vec{e}_c e^{i\vec{k}_c\vec{r}}$. Here, we chose the same notation as for the electric probe field component, but with an index c and a total phase ψ. The magnetic probe field component is defined analogously as $\vec{B}_p(\vec{r}) = \mathcal{B}_p\vec{b}_p e^{i\vec{k}_p\vec{r}}$. Note that the magnetic probe field component unit polarization vector and its electric counterpart are connected via $\vec{b}_p = \vec{\kappa}\times\vec{e}_p$ due to the Maxwell equations with unit propagation direction vector $\vec{\kappa} = \vec{k}_p/k_p$.

In rotating-wave and dipole approximation, we arrive at the Hamiltonian

$$\begin{aligned}H =& H_0 + H_I\,, \qquad (3.2a)\\ H_0 =& \sum_{j=1}^{3}\hbar\omega_j|j\rangle\langle j|\,, \qquad (3.2b)\\ H_I =& -\hbar\,\left(\Omega_{21}e^{-i\omega_p t}|2\rangle\langle 1| + \Omega_{32}e^{-i\omega_p t}|3\rangle\langle 2|\right.\\ & \left. + \Omega_{31}e^{-i\omega_c t}|3\rangle\langle 1| + \text{H.c.}\right)\,. \qquad (3.2c)\end{aligned}$$

Note that in the rotating wave approximation, the magnetic control field component can be neglected, because it does not couple near-resonantly to a magnetic transition. In Eqs. (3.2), the energy of state $|i\rangle$ is $\hbar\omega_i$ ($i \in \{1,2,3\}$) and, analogously to Sec. 2.1, the Rabi frequencies are defined as

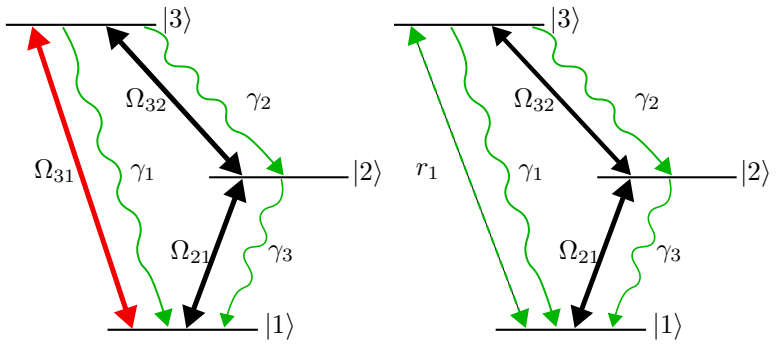

Figure 3.1: a) The three-level system driven by coherent fields in loop configuration. The probe field components are denoted by black solid double arrows, the coupling field by red solid double arrows. Spontaneous emission is indicated by the wiggly green arrows. The transition $|1\rangle \rightarrow |2\rangle$ couples to the magnetic component, while transition $|2\rangle \rightarrow |3\rangle$ couples to the electric component of the same probe field. b) Reference system obtained by replacing the coherent control field by an incoherent, bi-directional pumping, indicated by the green dashed double arrow.

$$\Omega_{21} = e^{i\phi} \vec{B}_p(\vec{r})\, \vec{\mu}_{21}/\hbar\,, \tag{3.3a}$$

$$\Omega_{32} = e^{i\phi} \vec{E}_p(\vec{r})\, \vec{d}_{32}/\hbar\,, \tag{3.3b}$$

$$\Omega_{31} = e^{i\psi} \vec{E}_c(\vec{r})\, \vec{d}_{31}/\hbar\,. \tag{3.3c}$$

The electric dipole moments are defined as $\vec{d}_{32} = \langle 3|\vec{d}|2\rangle$ and $\vec{d}_{31} = \langle 3|\vec{d}|1\rangle$. Analogously, the magnetic dipole moment is $\vec{\mu}_{21} = \langle 2|\vec{\mu}|1\rangle$, with $\vec{\mu}_{12} = \vec{\mu}^*_{21}$. Here, $\vec{d}$ and $\vec{\mu}$ are the electric and magnetic dipole operator, respectively, and $\vec{d}_{ij} = \vec{d}^*_{ji}$, $\vec{\mu}_{ij} = \vec{\mu}^*_{ji}$, and $\Omega_{ij} = \Omega^*_{ji}$.

3.2.2 Equations of motion

In this section, we derive the equations of motion for a general system that contains both systems of interest shown in Fig. 3.1 as special cases. To this end, we consider a three-level system that — on transition $|1\rangle \rightarrow |2\rangle$ — combines coherent pumping by a control field and bi-directional incoherent pumping. Since this system is a closed-loop system, in general there is no stationary state in the long-time limit and the Hamiltonian necessarily has an intrinsic explicit time dependence [28, 29, 30, 31, 32, 33, 34, 35, 36, 37, 38, 39, 40, 41]. Therefore, we cannot transform into a time-independent system as in Sec. 2.1.3, but still simplify the time dependence. To this end, we apply the transformation

$$V = e^{\frac{i}{\hbar}(H_0+X)t}(H_I - X)e^{-\frac{i}{\hbar}(H_0+X)t}\,, \tag{3.4}$$

where $X = \Delta_1|1\rangle\langle 1| + \Delta_2|2\rangle\langle 2|$. Here, we chose the notations $\Delta_1 = \omega_3 - \omega_1 - \omega_c$ and $\Delta_2 = \omega_3 - \omega_2 - \omega_p$ for the detunings of the electric control and probe field component to the respective transitions they couple to. Consequently, the coherences transform according to

$$\varrho_{21} = e^{-i(\omega_c-\omega_p)t}\tilde{\varrho}_{21}\,, \tag{3.5a}$$
$$\varrho_{32} = e^{-i\omega_p t}\tilde{\varrho}_{32}\,, \tag{3.5b}$$
$$\varrho_{31} = e^{-i\omega_c t}\tilde{\varrho}_{31}\,. \tag{3.5c}$$

By applying this transformation, we arrive at the following equations of motions, if we include spontaneous decay in the Born-Markov approximation:

$$\begin{aligned}
\frac{\partial}{\partial t}\tilde{\varrho}_{11} =& - r_1\tilde{\varrho}_{11} + \gamma_3\tilde{\varrho}_{22} + (\gamma_1 + r_1)\,\tilde{\varrho}_{33} + ie^{-i\Delta t}\Omega_{12}\tilde{\varrho}_{21} \\
& - ie^{i\Delta t}\Omega_{21}\tilde{\varrho}_{12} + i\Omega_{13}\tilde{\varrho}_{31} - i\Omega_{31}\tilde{\varrho}_{13}\,, && (3.6a)\\
\frac{\partial}{\partial t}\tilde{\varrho}_{12} =& - \left[i\,(\Delta - \Delta_3) + \frac{1}{2}\,(r_1 + \gamma_3)\right]\tilde{\varrho}_{12} - i\Omega_{32}\tilde{\varrho}_{13} \\
& - ie^{-i\Delta t}\Omega_{12}\,(\tilde{\varrho}_{11} - \tilde{\varrho}_{22}) + i\Omega_{13}\tilde{\varrho}_{32}\,, && (3.6b)\\
\frac{\partial}{\partial t}\tilde{\varrho}_{13} =& - \left[i\,(\Delta - \Delta_2 - \Delta_3) + \frac{1}{2}\,(2r_1 + \gamma_1 + \gamma_2)\right]\tilde{\varrho}_{13} \\
& - i\Omega_{13}\,(\tilde{\varrho}_{11} - \tilde{\varrho}_{33}) - i\Omega_{23}\tilde{\varrho}_{12} + ie^{-i\Delta t}\Omega_{12}\tilde{\varrho}_{23}\,, && (3.6c)\\
\frac{\partial}{\partial t}\tilde{\varrho}_{22} =& - \gamma_3\tilde{\varrho}_{22} + \gamma_2\tilde{\varrho}_{33} - ie^{-i\Delta t}\Omega_{12}\tilde{\varrho}_{21} \\
& + ie^{i\Delta t}\Omega_{21}\tilde{\varrho}_{12} - i\Omega_{32}\tilde{\varrho}_{23} + i\Omega_{23}\tilde{\varrho}_{32}\,, && (3.6d)\\
\frac{\partial}{\partial t}\tilde{\varrho}_{23} =& - \left[-i\Delta_2 + \frac{1}{2}\,(r_1 + \gamma_1 + \gamma_2 + \gamma_3)\right]\tilde{\varrho}_{23} \\
& - i\Omega_{13}\tilde{\varrho}_{21} + ie^{i\Delta t}\Omega_{21}\tilde{\varrho}_{13} + i\Omega_{23}\,(\tilde{\varrho}_{33} - \tilde{\varrho}_{22})\,, && (3.6e)\\
\tilde{\varrho}_{33} =& 1 - \tilde{\varrho}_{11} - \tilde{\varrho}_{22}\,. && (3.6f)
\end{aligned}$$

Here, $\tilde{\varrho}_{ij}$ $(i, j \in \{1, 2, 3\})$ is the density matrix in the interaction picture obtained by transformation of ϱ_{ij} according to Eq. (3.4). One can see that this transformation simplifies the explicit time dependence on the right hand side of the equations of motion to factors of $e^{\pm i\Delta t}$ in front of the weak magnetic probe field Rabi frequency Ω_{21} or Ω_{12}, respectively. $\gamma_\alpha, \alpha \in \{1, 2, 3\}$ are spontaneous emission rates on the different transitions. Also, we introduced the detuning on the magnetic probe transition $\Delta_3 = \omega_2 - \omega_1 - \omega_p$, as well as the so-called multiphoton detuning

$$\Delta = \Delta_2 + \Delta_3 - \Delta_1\,, \tag{3.7}$$

which for the current system evaluates to

$$\Delta = \omega_c - 2\omega_p \,. \tag{3.8}$$

By setting the incoherent pumping rate $r_1 = 0$ in Eqs. (3.6), we arrive at the equations of motion for the system in Fig. 3.1 a). To obtain the equations of motion for the incoherently pumped system shown in Fig. 3.1 b), one has to set $\Omega_{31} = \Omega_{13} = 0$ and $\Delta = 0$. The latter causes the right-hand side of Eqs. (3.6) to become time-independent.

3.2.3 Electric and magnetic responses

Since our aim is to study the magnetic and electric responses, we require an expression for them in terms of the density matrix elements governed by Eqs. (3.6). We will find such a relation in this subsection, analogously to Sec. 2.1.2. However, this time we need to take into account the electric field, since it also couples to our system. In doing so, it is important to note that electric fields cannot only induce electric polarization, but also magnetization [22, 17]. Similarly, magnetic fields can induce both magnetization and polarization.

For definitiveness, in the following we specialize to a circularly polarized (σ^+) probe field and probe field propagation in z direction, since one then obtains for the probe field polarization vectors $\vec{b}_p = -i\vec{e}_p$, i.e., they are parallel. Therefore, the tensorial structure of the response coefficients in the macroscopic polarization $\vec{P}$ and magnetization $\vec{M}$ simplifies considerably,

$$\begin{aligned} \vec{P}(\vec{r},t) = \quad & \frac{1}{c}\int_{-\infty}^{\infty} \xi_{EH}(\tau)\, \vec{H}(\vec{r},t-\tau)\, d\tau \\ & + \varepsilon_0 \int_{-\infty}^{\infty} \chi_e(\tau)\, \vec{E}(\vec{r},t-\tau)\, d\tau \,, \qquad (3.9a) \\ \vec{M}(\vec{r},t) = \quad & \frac{1}{c\mu_0}\int_{-\infty}^{\infty} \xi_{HE}(\tau)\, \vec{E}(\vec{r},t-\tau)\, d\tau \\ & + \int_{-\infty}^{\infty} \chi_m(\tau)\, \vec{H}(\vec{r},t-\tau)\, d\tau \,, \qquad (3.9b) \end{aligned}$$

and the electric and magnetic susceptibility χ_e and χ_m and the chirality coefficients ξ_{HE} and ξ_{EH} become scalars. While the susceptibilities determine the electric [magnetic] response to the electric [magnetic] probe field component, the chiralities or cross-terms determine the magnetic response to the electric probe field component and vice versa. Here, c is the vacuum speed of light, and μ_0 and ε_0 are the vacuum permeability and permittivity. Note that, with the notation of Eqs. (3.9), the

refractive index in Fourier space is given as [17]

$$n(\omega) = \sqrt{\varepsilon_r(\omega)\mu_r(\omega) - \frac{1}{4}\left[\tilde{\xi}_{EH}(\omega) + \tilde{\xi}_{HE}(\omega)\right]^2} + \frac{i}{2}\left[\tilde{\xi}_{EH}(\omega) - \tilde{\xi}_{HE}(\omega)\right] , \tag{3.10}$$

where

$$\varepsilon_r(\omega) = \tilde{\chi}_e(\omega) + 1 , \tag{3.11a}$$
$$\mu_r(\omega) = \tilde{\chi}_m(\omega) + 1 , \tag{3.11b}$$

are the relative permittivity $\varepsilon_r(\omega)$ and the relative permeability $\mu_r(\omega)$ in Fourier space. As in Sec. 2, we do not write a tilde on top of μ_r and ε_r for a better readibility. Also, $\tilde{\xi}_{EH}(\omega)$, $\tilde{\xi}_{HE}(\omega)$, $\tilde{\chi}_m(\omega)$ and $\tilde{\chi}_e(\omega)$ are the Fourier transformed response coefficients of the corresponding time domain quantities in Eqs. (3.9). They satisfy $\tilde{\chi}_e(\omega)^* = \tilde{\chi}_e(-\omega)$ and similar for the other susceptibilities and the chiralities. For vanishing chirality coefficients, Eq. (3.10) reduces to the well-known relation between the refractive index and the permittivity and permeability for non-chiral media (see Eq. (1.2)).

Let us now continue to find an expression of the response coefficients in terms of the density matrix elements. Plugging Eqs. (3.1) into Eqs. (3.9), we arrive at

$$\vec{P} = \frac{\tilde{\xi}_{EH}(\omega_p)}{c\mu_0}\vec{B}_p(\vec{r})e^{i(\phi-\omega_p t)} + \frac{\tilde{\xi}_{EH}(\omega_c)}{c\mu_0}\vec{B}_c(\vec{r})e^{i(\psi-\omega_c t)} + \varepsilon_0\tilde{\chi}_e(\omega_p)\vec{E}_p(\vec{r})e^{i(\phi-\omega_p t)} + \varepsilon_0\,\tilde{\chi}_e(\omega_c)\vec{E}_c(\vec{r})e^{i(\psi-\omega_c t)} + \text{c.c.} , \tag{3.12a}$$

$$\vec{M} = \frac{\tilde{\xi}_{HE}(\omega_p)}{\mu_0 c}\vec{E}_p(\vec{r})e^{i(\phi-\omega_p t)} + \frac{\tilde{\xi}_{HE}(\omega_c)}{\mu_0 c}\vec{E}_c(\vec{r})e^{i(\psi-\omega_c t)} + \frac{1}{\mu_0}\tilde{\chi}_m(\omega_p)\vec{B}_p(\vec{r})e^{i(\phi-\omega_p t)} + \frac{1}{\mu_0}\tilde{\chi}_m(\omega_c)\vec{B}_c(\vec{r})e^{i(\psi-\omega_c t)} + \text{c.c.} . \tag{3.12b}$$

Here, we have used $\vec{B} = \mu_0\vec{H}$, which holds since $\vec{B}$ is an external field. Note that the Rabi frequencies in the equations of motion contain local fields, whereas Eqs. (3.9) contain external fields [18]. However, local field effects are not considered here and therefore we do not distinguish between external and local fields, as is valid for moderate particle densities.

The polarization and magnetization are also given by (cp. Eq. (2.9))

$$\vec{P} = N\vec{p} \tag{3.13a}$$
$$\vec{M} = N\vec{m} \tag{3.13b}$$

where N is the particle density and $\vec{p}$ and $\vec{m}$ are the mean polarization and magnetization per atom [23]. We can express the mean polarization as $\vec{p} = Tr(\varrho\vec{d})$ and the mean magnetization as $\vec{m} = Tr(\varrho\vec{\mu})$. These traces can be written in terms of the transformed density matrix elements $\tilde{\varrho}_{ij}$ $(i,j \in \{1,2,3\})$ which are given as solutions of the equations of motion (3.6).

We are only interested in the response at the probe field frequency. However, in the closed-loop system, there is an implicit time dependence of the $\tilde{\varrho}_{ij}$ $(i,j \in \{1,2,3\})$, since the transformed Hamiltonian V is still time-dependent. This can also be seen by the time-dependent right-hand side of Eqs. (3.6). Therefore, the transformed coherences of the probe transitions $\tilde{\varrho}_{21}$ and $\tilde{\varrho}_{32}$ also have contributions that are not in phase with the probe field. These contributions will be investigated in detail in Sec. 3.3.1. We now introduce the notation

$$\hat{\varrho}_{21} = e^{i\omega_p t}\varrho_{21} , \tag{3.14a}$$
$$\hat{\varrho}_{32} = e^{i\omega_p t}\varrho_{32} , \tag{3.14b}$$

such that the quantities $\hat{\varrho}_{21}$ and $\hat{\varrho}_{32}$ oscillate at the frequency ω_p of the probe field - apart, of course from the implicit time-dependence they still contain. With Eqs. (3.14) and (3.5), we have

$$\hat{\varrho}_{21} = e^{i\omega_p t}\varrho_{21} = e^{-i(\omega_c - 2\omega_p)t}\tilde{\varrho}_{21} , \tag{3.15a}$$
$$\hat{\varrho}_{32} = e^{i\omega_p t}\varrho_{32} = \tilde{\varrho}_{32} . \tag{3.15b}$$

One can see that at multiphoton resonance $\Delta = 0 \Leftrightarrow \omega_c = \omega_p/2$ (see Eq. (3.8)), the coherences $\hat{\varrho}_{21}$ and $\tilde{\varrho}_{21}$ and, respectively, $\hat{\varrho}_{32}$ and $\tilde{\varrho}_{32}$ coincide. We will investigate the multiphoton resonance case further in Sec. 3.3.1.

In the incoherently pumped system of Fig. 3.1 b), the Hamiltonian is time-independent, and therefore the $\tilde{\varrho}_{ij}$ $(i,j \in \{1,2,3\})$ do not have an implicit time dependence. In order to be consistent with the notation of Eq. (3.14), we write

$$\hat{\varrho}_{21} = \tilde{\varrho}_{21} , \tag{3.16a}$$
$$\hat{\varrho}_{32} = \tilde{\varrho}_{32} . \tag{3.16b}$$

Thus, also in the incoherently pumped system, $\hat{\varrho}_{21}$ and $\hat{\varrho}_{32}$ denote the coherences oscillating in phase with the probe field, since $\tilde{\varrho}_{21}$ and $\tilde{\varrho}_{32}$ oscillate in phase with the probe field according to Eqs. (3.5) with $\Delta = 0$. We now proceed with the evaluation of the response coefficients. Keeping only terms oscillating in phase with the probe

field, we arrive at

$$\tilde{\chi}_e = \frac{N}{\varepsilon_0 \hbar}\, d_{32}^2\, \hat{\varrho}_{32}^{(0,1)}\,, \tag{3.17a}$$

$$\tilde{\chi}_m = \frac{N\mu_0}{\hbar}\, \mu_{21}^2\, \hat{\varrho}_{21}^{(1,0)}\,, \tag{3.17b}$$

$$\tilde{\xi}_{HE} = -i\, \frac{Nc\mu_0}{\hbar}\, d_{32}\, \mu_{21}\, e^{i\Phi} \hat{\varrho}_{21}^{(0,1)}\,, \tag{3.17c}$$

$$\tilde{\xi}_{EH} = i\, \frac{Nc\mu_0}{\hbar}\, d_{32}\, \mu_{21}\, e^{-i\Phi} \hat{\varrho}_{32}^{(1,0)}\,, \tag{3.17d}$$

where the $\hat{\varrho}_{ij}^{(1,0)}$ and $\hat{\varrho}_{ij}^{(0,1)}$ are expansion coefficients in a Taylor series of $\hat{\varrho}_{ij}$ ($i,j \in \{1,2,3\}$) in terms of Ω_{32} and Ω_{21}:

$$\begin{aligned}\hat{\varrho}_{32} = {} & \hat{\varrho}_{32}^{(0,0)} + \hat{\varrho}_{32}^{(0,1)}\Omega_{32} + \hat{\varrho}_{32}^{(1,0)}\Omega_{21} \\ & + O(\Omega_{21}^2, \Omega_{32}^2, \Omega_{21}\Omega_{32})\,,\end{aligned} \tag{3.18a}$$

$$\begin{aligned}\hat{\varrho}_{21} = {} & \hat{\varrho}_{21}^{(0,0)} + \hat{\varrho}_{21}^{(0,1)}\Omega_{32} + \hat{\varrho}_{21}^{(1,0)}\Omega_{21} \\ & + O(\Omega_{21}^2, \Omega_{32}^2, \Omega_{21}\Omega_{32})\,.\end{aligned} \tag{3.18b}$$

In Eqs. (3.18), we call $\hat{\varrho}_{32}^{(0,1)}\Omega_{32}$ and $\hat{\varrho}_{21}^{(1,0)}\Omega_{21}$ the "direct terms", since they correspond to the susceptibilities, while $\hat{\varrho}_{32}^{(1,0)}\Omega_{21}$ and $\hat{\varrho}_{21}^{(0,1)}\Omega_{32}$ are denoted "cross terms" as they give rise to the chiralities. Also, in Eqs. (3.17), we have introduced the relative phase,

$$\Phi = \phi_{32} - \phi_{21}\,, \tag{3.19}$$

between the scalar dipole moments which we write as

$$\vec{d}_{32}\vec{e}_p \;\; = d_{32}\, e^{i\phi_{32}}\,, \tag{3.20a}$$

$$\vec{\mu}_{21}\vec{b}_p \;\; = \mu_{21}\, e^{i\phi_{21}}\,. \tag{3.20b}$$

Eqs. (3.17) are the desired relation between the density matrix elements and the coefficients that determine the magnetic response. These can now be used in Eqs. (3.12) in order to determine the contribution of the various processes to the polarization and magnetization. Keeping only the terms relevant to the probe field response in phase with the probe field frequency, we find

$$\begin{aligned}\vec{P} = {} & \frac{N}{\hbar}\, \vec{e}_p\, e^{i(\vec{k}_p\vec{r}-\omega_p t+\phi)} \Big(d_{32}\mu_{21}\, \mathcal{B}_p\, e^{-i\Phi}\, \hat{\varrho}_{32}^{(1,0)} \\ & + d_{32}^2\, \mathcal{E}_p\, \hat{\varrho}_{32}^{(0,1)} \Big) + \text{c.c.}\,,\end{aligned} \tag{3.21a}$$

$$\begin{aligned}\vec{M} = {} & \frac{N}{\hbar}\, \vec{b}_p\, e^{i(\vec{k}_p\vec{r}-\omega_p t+\phi)} \Big(d_{32}\mu_{21}\, \mathcal{E}_p\, e^{i\Phi}\, \hat{\varrho}_{21}^{(0,1)} \\ & + \mu_{21}^2\, \mathcal{B}_p\, \hat{\varrho}_{21}^{(1,0)} \Big) + \text{c.c.}\,.\end{aligned} \tag{3.21b}$$

3.3 Analytical results

We next solve the time-dependent equations of motion (3.6) for both of our systems. First, we consider the closed-loop system for arbitrary multiphoton detuning Δ and derive an expression for the coherences to first order in the magnetic and electric probe field Rabi frequencies Ω_{21} and Ω_{32}. Then, we consider the special cases $\Delta \neq 0$ and $\Delta = 0$. Finally, we solve the incoherently pumped system.

3.3.1 Closed-loop system

The equations of motion for the closed-loop system are obtained from Eqs. (3.6), if we set $r_1 = 0$. We define the vector $\tilde{R}$ containing all density matrix elements,

$$\tilde{R} = (\tilde{\varrho}_{11}, \tilde{\varrho}_{12}, \tilde{\varrho}_{13}, \tilde{\varrho}_{21}, \tilde{\varrho}_{22}, \tilde{\varrho}_{23}, \tilde{\varrho}_{31}, \tilde{\varrho}_{32})^T \,. \tag{3.22}$$

The equations of motion (3.6) can be rewritten in terms of $\tilde{R}$ as

$$\frac{\partial}{\partial t}\tilde{R} = M\tilde{R} + \Sigma \,. \tag{3.23}$$

Here, we have eliminated $\tilde{\varrho}_{33}$ via the trace condition $\mathrm{Tr}(\tilde{\varrho}) = 1$, which is the reason for the appearance of the constant term Σ in Eq. (3.23). We proceed by splitting both M and $\tilde{R}$ up into terms with different time-dependencies as follows:

$$M = \quad M_0 + M_1\Omega_{21}e^{i\Delta t} + M_{-1}\Omega_{12}e^{-i\Delta t} \,, \tag{3.24}$$

$$\Sigma = \quad \Sigma_0 + \Sigma_1\Omega_{21}e^{i\Delta t} + \Sigma_{-1}\Omega_{12}e^{-i\Delta t} \,, \tag{3.25}$$

where M_k and $\Sigma_k \,, k \in \{-1, 0, 1\}$, are time-independent.

According to Floquet's theorem [25], the solution of $\tilde{R}$ has only contributions oscillating with frequencies that are integer multiples of Δ. Since terms oscillating at higher frequencies are suppressed by powers of the magnetic probe field Rabi frequency $|\Omega_{21}|$, we expand $\tilde{R}$ to first order in this Rabi frequency, and work with the ansatz

$$\tilde{R} = \tilde{R}_0 + \tilde{R}_1\Omega_{21}e^{i\Delta t} + \tilde{R}_{-1}\Omega_{12}e^{-i\Delta t} + O(|\Omega_{12}|^2) \,. \tag{3.26}$$

From Eqs. (3.23-3.26), a comparison of coefficients yields

$$\tilde{R}_0 = \quad -M_0^{-1}\Sigma_0 \,, \tag{3.27a}$$

$$\tilde{R}_1 = \quad -(M_0 - i\Delta)^{-1}(M_1\tilde{R}_0 + \Sigma_1) \,, \tag{3.27b}$$

$$\tilde{R}_{-1} = \quad -(M_0 + i\Delta)^{-1}(M_{-1}\tilde{R}_0 + \Sigma_{-1}) \,. \tag{3.27c}$$

Since the density matrix element $\hat{\varrho}_{21}$ oscillating in phase with the probe field and $\tilde{\varrho}_{21}$ are related as

$$\begin{aligned} \hat{\varrho}_{21} = \quad & e^{-i(\omega_c - 2\omega_p)t}\tilde{\varrho}_{21} \\ = \quad & e^{-i(\omega_c - 2\omega_p)t}\,[\tilde{R}_0]_4 + \,[\tilde{R}_1]_4\Omega_{21} \\ & + e^{-2i(\omega_c - 2\omega_p)t}\,[\tilde{R}_{-1}]_4\Omega_{12} \,, \end{aligned} \tag{3.28}$$

one can determine $[\tilde{R}_1]_4$ as the part of $\hat{\varrho}_{21}$ oscillating in phase with the probe field, where the index 4 denotes the fourth component of $\tilde{R}_1$. Likewise, the relevant part of $\hat{\varrho}_{32}$ can be identified with $[\tilde{R}_0]_8$.

Note that $\tilde{R}_0$, $\tilde{R}_{-1}$ and $\tilde{R}_1$ are independent of Ω_{21}, but do depend on the electric probe field Rabi frequency Ω_{32}, which we did not take into account so far. Since we are only interested in the linear magnetic and electric response, we still have to expand the appropriate components of $\tilde{R}$ in Ω_{32}. We obtain

$$\begin{aligned}\hat{\varrho}_{21} =&[\tilde{R}_1]_4\,\Omega_{21} + [\tilde{R}_0]_4\,e^{-i(\omega_c-2\omega_p)t} \\ &+ O(\Omega_{21}^2, \Omega_{32}^2, \Omega_{21}\Omega_{32})\,, \end{aligned} \tag{3.29a}$$

$$\begin{aligned}\hat{\varrho}_{32} =&[\tilde{R}_{-1}]_8\,e^{-i(\omega_c-2\omega_p)t}\Omega_{12} + [\tilde{R}_0]_8 \\ &+ O(\Omega_{21}^2, \Omega_{32}^2, \Omega_{21}\Omega_{32})\,, \end{aligned} \tag{3.29b}$$

where $[\tilde{R}_0]_4 \propto \Omega_{23}$ and $[\tilde{R}_0]_8 \propto \Omega_{32}$, and higher orders of Ω_{32} have been neglected. With Eqs. (3.27) and (3.29), an explicit evaluation yields

$$\begin{aligned}\hat{\varrho}_{21} =&\frac{2}{B}\left\{ \frac{8\Delta_1^3\gamma_3 + 4i\Delta_1^2\gamma_3\,(2i\Delta_3+\gamma_s) + \Delta_3\,[8|\Omega_{31}|^2\,(\gamma_2-\gamma_3) - 2\Gamma]}{4|\Omega_{31}|^2 + (2\Delta_3 - i\gamma_3)\,(2\Delta_1 - 2\Delta_3 + i\gamma_s)} \right. \\ &\left. + \frac{2\Delta_1\,[-4|\Omega_{31}|^2\,(\gamma_2-2\gamma_3)+\Gamma] - i\,[(4|\Omega_{31}|^2\gamma_2 - \Gamma)\,\gamma_s - 4|\Omega_{31}|^2\gamma_3^2]}{4|\Omega_{31}|^2 + (2\Delta_3 - i\gamma_3)\,(2\Delta_1 - 2\Delta_3 + i\gamma_s)} \right\}\Omega_{21} \\ &- \left\{ \frac{4}{B}\frac{4|\Omega_{31}|^2\,(\gamma_2-\gamma_3) - [2\Delta_1 + i(\gamma_1+\gamma_2)]\,\gamma_3\,(2\Delta_2 + i\gamma_s)}{4|\Omega_{31}|^2 + [2i\,(\Delta_1-\Delta_2)+\gamma_3]\,(-2i\Delta_2+\gamma_s)} \right\} e^{-i\Delta t}\,\Omega_{31}\Omega_{23}\,, \end{aligned} \tag{3.30a}$$

$$\begin{aligned}\hat{\varrho}_{32} =&\left\{ \frac{4}{B}\frac{4|\Omega_{31}|^2\,(\gamma_3-\gamma_2) + [2\Delta_1 + i\,(\gamma_1+\gamma_2)]\,\gamma_3\,(2\Delta_1 - 2\Delta_3 - i\gamma_s)}{4|\Omega_{31}|^2 + (2\Delta_3 + i\gamma_3)\,(2\Delta_1 - 2\Delta_3 - i\gamma_s)} \right\} e^{-i\Delta t}\,\Omega_{31}\Omega_{12} \\ &- \left\{ |\Omega_{31}|^2\frac{8}{B}\frac{[2\,(-\Delta_1+\Delta_2)\,\gamma_2 + i\gamma_3\,(2i\Delta_2 + \gamma_1 + \gamma_3)]}{4|\Omega_{31}|^2 + (-2i\Delta_1 + 2i\Delta_2 + \gamma_3)\,(2i\Delta_2 + \gamma_s)} \right\}\Omega_{32}\,, \end{aligned} \tag{3.30b}$$

where

$$\begin{aligned} B &= 4\Delta_1^2\gamma_3 + \Gamma + 4|\Omega_{31}|^2\,(\gamma_2 + 2\gamma_3)\,, \\ \gamma_s &= \gamma_1 + \gamma_2 + \gamma_3\,, \\ \Gamma &= (\gamma_1+\gamma_2)^2\,\gamma_3\,. \end{aligned}$$

Note that in the fractions of Eq. (3.30), the multiphoton detuning Δ has been replaced using Eq. (3.7). However, Δ still appears in the exponent where it has simply been used as an abbreviation according to Eq. (3.8). Also, the contributions without the explicit time dependence in the exponential factor are the direct terms, while the other parts are cross terms.

Non-zero multiphoton detuning ($\Delta \neq 0$)

In the case of non-zero multiphoton detuning, $\Delta \neq 0 \Leftrightarrow 2\omega_p \neq \omega_c$, only the direct terms in Eqs. (3.30) oscillate in phase with the probe field. Therefore, only these terms contribute to the coherences and thus to the magnetic and electric response. Then, the cross terms in Eqs. (3.18) vanish and so do the chirality coefficients according to Eqs. (3.17), $\tilde{\xi}_{EH} = \tilde{\xi}_{HE} = 0$. This means that the polarization [magnetization] is entirely determined by the electric [magnetic] probe field component. It will turn out in Sec. 3.3.2 that this case is comparable to the incoherently pumped system, in which there are no cross terms either.

Multiphoton resonance ($\Delta = 0$)

We now focus on the case of multiphoton resonance, i.e. $\Delta = 0$ or $\omega_p = \omega_c/2$. Hence, Eqs. (3.6) become time-independent and we can now solve the linear system Eq. (3.23) for a time-independent steady-state solution of $\tilde{R}$ using $\frac{\partial}{\partial t}\tilde{R} = 0$. Now, all terms in Eq. (3.26) contribute, apart from terms that contain Ω_{32} in higher than first order. From Eqs. (3.15) we also find that the simplified relations between the two considered reference frames Eqs. (3.16) hold as in the case of incoherent driving.

We again neglect terms of higher order in the probe field Rabi frequency and arrive at

$$\begin{aligned}\hat{\varrho}_{21} = \quad & -\frac{2i}{C_+ D}\Big\{8i\Delta_2^3\gamma_3 + 4\Delta_2^2\left(4i\Delta_3 - \gamma_s\right)\gamma_3 - \left(4\Delta_3^2\gamma_3 + \Gamma\right)\gamma_s \\ & \qquad + 4|\Omega_{31}|^2\left[\gamma_2\left(\gamma_1+\gamma_2\right) + \left(2i\Delta_3 + \gamma_2\right)\gamma_3 - \gamma_3^2\right] \\ & \qquad + 2i\Delta_2\left[-4|\Omega_{31}|^2\left(\gamma_2 - 2\gamma_3\right) + \Gamma + 4\gamma_3\Delta_3\left(\Delta_3 + i\gamma_s\right)\right]\Big\}\ \Omega_{21} \\ & -\frac{4\Omega_{31}}{C_+ D}\left\{4|\Omega_{31}|^2\left(\gamma_2 - \gamma_3\right) - \left[2\left(\Delta_2 + \Delta_3\right) + i\left(\gamma_1+\gamma_2\right)\right]\gamma_3\left(2\Delta_2 + i\gamma_s\right)\right\}\ \Omega_{23}\,, \end{aligned} \tag{3.32a}$$

$$\begin{aligned}\hat{\varrho}_{32} = \quad & -\frac{4\Omega_{31}}{C_- D}\left\{4|\Omega_{31}|^2\left(\gamma_2 - \gamma_3\right) - \left[2\left(\Delta_2 + \Delta_3\right) + i\left(\gamma_1+\gamma_2\right)\right]\gamma_3\left(2\Delta_2 - i\gamma_s\right)\right\}\ \Omega_{12} \\ & -\frac{8i}{C_- D}|\Omega_{31}|^2\left[2i\Delta_3\gamma_2 + \gamma_3\left(2i\Delta_2 + \gamma_1 + \gamma_3\right)\right]\ \Omega_{32}\,, \end{aligned} \tag{3.32b}$$

where

$$\begin{aligned} C_\pm &= 4|\Omega_{31}|^2 + \left(\pm 2i\Delta_3 + \gamma_3\right)\left(\mp 2i\Delta_2 + \gamma_s\right)\,, \\ D &= 4\left(\Delta_2 + \Delta_3\right)^2\gamma_3 + \Gamma + 4|\Omega_{31}|^2\left(\gamma_2 + 2\gamma_3\right)\,, \\ \Gamma &= \left(\gamma_1 + \gamma_2\right)^2\gamma_3\,, \\ \gamma_s &= \gamma_1 + \gamma_2 + \gamma_3\,. \end{aligned}$$

The control field detuning Δ_1 has been eliminated using the relation $\Delta_1 = \Delta_2 + \Delta_3$ which follows from Eq. (3.7) in the case of $\Delta = 0$.

We see that both the direct terms and the cross terms contribute to the coherences and thus to the magnetic and electric response in this case. Therefore, the chirality coefficients are non-zero in the resonance case $\Delta = 0$, see Eqs. (3.17).

3.3.2 Incoherently pumped system

We now consider the electric and magnetic response in the incoherently pumped system shown in Fig. 3.1(b). It will serve us as a reference in a comparison to the results of the closed-loop system in order to determine the exact origin of the various contributions to the medium response.

In this system, the transformed Hamiltonian is time-independent. Hence, we can solve for the steady-state solution just as in the case of multiphoton resonance in Sec. 3.3.1. The equations of motion follow from Eqs. (3.6) with $\Delta = 0$ and $\Omega_{31} = \Omega_{13} = 0$. Instead of the coherent coupling field, they include an incoherent, bi-directional pump rate r_1 on transition $|1\rangle \rightarrow |3\rangle$.

Using Eqs. (3.16), up to first order in the probe field we find for the coherences in a reference frame oscillating in phase with the probe field:

$$\begin{aligned}\hat{\varrho}_{21} =& \frac{2i[r_1(\gamma_3 - \gamma_2) + (\gamma_1 + \gamma_2)\gamma_3]}{(2i\Delta_3 + r_1 + \gamma_3)[(\gamma_1 + \gamma_2)\gamma_3 + r_1(\gamma_2 + 2\gamma_3)]}\,\Omega_{21} \\ &+ O(\Omega_{21}^2, \Omega_{32}^2, \Omega_{21}\Omega_{32})\,, \qquad (3.34a)\\ \hat{\varrho}_{32} =& \frac{2ir_1(\gamma_2 - \gamma_3)}{(2i\Delta_2 + \gamma_s + r_1)[(\gamma_1 + \gamma_2)\gamma_3 + r_1(\gamma_2 + 2\gamma_3)]}\,\Omega_{32} \\ &+ O(\Omega_{21}^2, \Omega_{32}^2, \Omega_{21}\Omega_{32})\,. \qquad (3.34b)\end{aligned}$$

In this case, the electric [magnetic] probe transition coherence is determined by the electric [magnetic] probe field component, and no cross-terms appear.

3.4 Comparison of the two systems

We will now proceed with a comparison of the two systems. To this end, we will discuss the expansion coefficients $\hat{\varrho}_{32}^{(a,b)}$ and $\hat{\varrho}_{21}^{(a,b)}$, $(a, b \in \{0, 1\})$ in Eqs. (3.18), since they determine the magnetic and electric response according to Eqs. (3.21).

It will turn out that the direct terms are similar in many regards in both systems. These terms describe the establishment of polarization [magnetization] due to the electric [magnetic] probe field component. But crucial differences are found for

the cross terms, which only appear in the closed-loop system for zero multiphoton detuning. These terms characterize the polarization [magnetization] due to the magnetic [electric] probe field component.

3.4.1 The direct terms

From Secs. 3.3.1, 3.3.1 and 3.3.2 it is clear that direct terms appear both in the closed-loop system and in the system with incoherent pumping. In Fig. 3.2, the corresponding expansion coefficients for the two cases are compared. Since transitions $|1\rangle \to |3\rangle$ and $|2\rangle \to |3\rangle$ are electrically dipole-allowed, whereas transition $|1\rangle \to |2\rangle$ is magnetically dipole-allowed, we choose the decay rates as $\gamma_1 = \gamma, \gamma_2 = \gamma, \gamma_3 = \alpha^2\gamma$. For the incoherent case, the pump rate is set to $r_1 = \gamma$, whereas in the closed-loop configuration, the coherent pump field is set to $\Delta_1 = 0, \Omega_{31} = \gamma$. All expansion coefficients are plotted against the respective probe field detunings Δ_2 or Δ_3.

We find that in many respects, the direct terms of both systems behave similarly. Apart from the AC Stark splitting in the closed-loop system, the general structure is comparable and in particular the magnitude of the coefficients is of similar order in both systems.

The similarities become more apparent when considering the dependence of the direct terms on the coherent pump rate Ω_{31} and the incoherent pump rate r_1, as shown in Fig. 3.3. For this figure, the direct terms of the loop system are evaluated at a particular detuning Δ_2 or Δ_3, respectively, at which the absolute value of the imaginary part becomes maximal. At the same point, the real part vanishes. For the incoherently pumped system, the corresponding maxima always occur at $\Delta_3 = 0$ or $\Delta_2 = 0$, respectively. This approach allows to compare the two systems independently of the AC Stark splitting appearing in the closed loop system only. Due to the growing splitting with increasing $|\Omega_{31}|$, a comparison at a fixed detuning would not be meaningful. It can be seen from Fig. 3.3 that both systems show a qualitatively similar dependence on the pumping strength. The shown imaginary part of the coherences characterizes the absorptive behavior of our systems: positive values stand for absorption and negative values for amplification of the magnetic or electric probe field component.

Interestingly, in both systems it is possible to choose the respective pump rate in such a way that $\hat{\varrho}_{21}$ vanishes at all frequencies. This is the case at the roots of the dashed lines in Fig. 3.3. It turns out that at these points, the populations of states $|1\rangle$ and $|2\rangle$ are the same such that the magnetic probe field component can traverse the medium without attenuation and without experiencing diffraction.

For the interpretation of Fig. 3.3, we calculate the coherences in terms of the (zeroth order) populations for arbitrary detuning. In the case of incoherent pumping, we

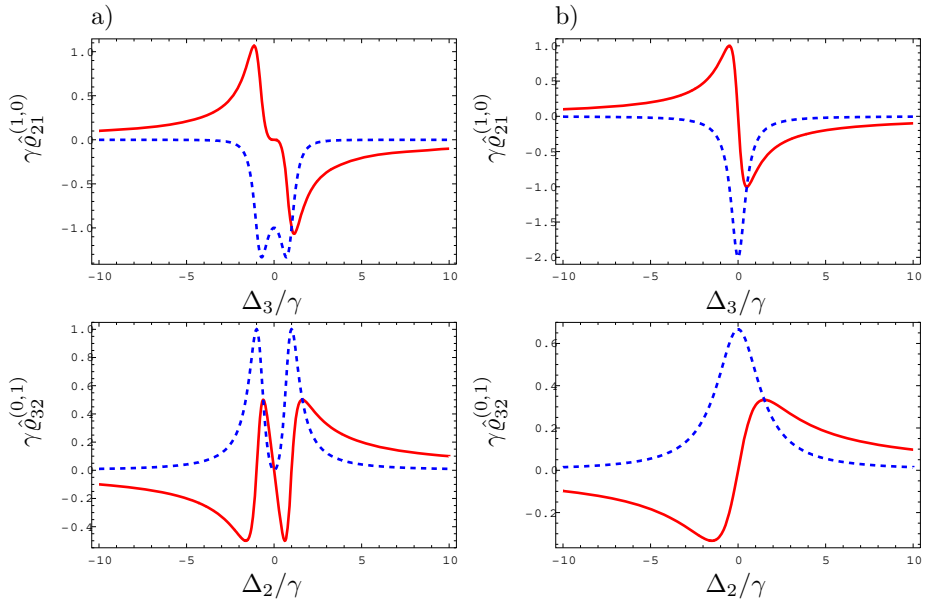

Figure 3.2: Real (red solid curve) and imaginary part (blue dashed curve) of the direct terms in the magnetic and electric susceptibility, respectively. The top row shows $\hat{\varrho}_{21}^{(1,0)}$, the bottom row $\hat{\varrho}_{32}^{(0,1)}$. (a) Closed-loop system and (b) incoherently pumped system as shown in Fig. 3.1.

obtain

$$\hat{\varrho}_{21} = 2\,\Omega_{21}\frac{\hat{\varrho}_{11}^{(0)} - \hat{\varrho}_{22}^{(0)}}{2\Delta_3 - i(r_1+\gamma_3)}\,, \tag{3.35a}$$

$$\hat{\varrho}_{32} = 2\,\Omega_{32}\frac{\hat{\varrho}_{22}^{(0)} - \hat{\varrho}_{33}^{(0)}}{2\Delta_2 - i(r_1+\gamma_1+\gamma_2+\gamma_3)}\,. \tag{3.35b}$$

The zeroth order populations are

$$\hat{\varrho}_{11}^{(0)} = \frac{(r_1+\gamma_1+\gamma_2)\gamma_3}{C}\,, \tag{3.36a}$$

$$\hat{\varrho}_{22}^{(0)} = \frac{r_1\gamma_2}{C}\,, \tag{3.36b}$$

$$\hat{\varrho}_{33}^{(0)} = \frac{r_1\gamma_3}{C}\,, \tag{3.36c}$$

where $C = r_1\gamma_2 + 2r_1\gamma_3 + \gamma_1\gamma_3 + \gamma_2\gamma_3$.

Note that in our system, $\gamma_3 \ll \gamma_2$ due to the different multipolarity of the transitions. Therefore, for small pump rates r_1, from Eqs. (3.36) one finds $\hat{\varrho}_{11}^{(0)} > \hat{\varrho}_{22}^{(0)} > \hat{\varrho}_{33}^{(0)}$. As a result, both probe transitions are absorptive — although for $\hat{\varrho}_{21}$ only in a very small range of r_1 as compared to γ.

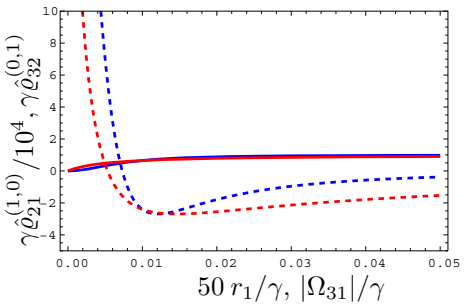

Figure 3.3: Dependence of the expansion coefficients $\hat{\varrho}_{32}^{(0,1)}$ in the closed loop (black solid line) and in the incoherently pumped system (green long dashed line) as well as $\hat{\varrho}_{21}^{(1,0)}$ for the closed-loop (blue dash-dotted) and the incoherently pumped system (red dashed) on the strength of the control field and the incoherent pump rate, respectively. Shown are only the imaginary parts at the maximum of the absolute value of the coefficients. For the incoherent configuration, the maximum of $\hat{\varrho}_{21}^{(1,0)}$ is always at $\Delta_3 = 0$, and the maximum of $\hat{\varrho}_{32}^{(0,1)}$ is at $\Delta_2 = 0$. The coefficients are scaled by γ to obtain a unitless quantity and $\hat{\varrho}_{21}^{(1,0)}$ is scaled by a factor of 10^{-4}. In this figure, negative values indicate amplification, positive values absorption.

For large r_1, Eqs. (3.36) show that $\hat{\varrho}_{11}^{(0)} < \hat{\varrho}_{22}^{(0)}$ and $\hat{\varrho}_{33}^{(0)} < \hat{\varrho}_{22}^{(0)}$. In fact, $\hat{\varrho}_{11}^{(0)} \approx \hat{\varrho}_{33}^{(0)}$ for $r_1 \gg \gamma$. Hence, the magnetic probe transition becomes amplifying, whereas the electric transition maintains its absorptive character. As expected, from Eqs. (3.35), it follows directly that a population inversion causes amplification.

As a side note, we would like to mention the fact that Eqs. (3.35) imply vanishing $\hat{\varrho}_{32}$ for $\gamma_2 = \gamma_3$. This is due to the fact that from Eqs. (3.36), one then finds $\hat{\varrho}_{22}^{(0)} = \hat{\varrho}_{33}^{(0)}$. However, this case is not of relevance for the current analysis, since $\gamma_3 \ll \gamma_2$.

Let us now examine the behavior of the closed-loop system with regard to a change of $|\Omega_{31}|$. In this case, the coherences are given by

$$\hat{\varrho}_{21} = 2\,\Omega_{21}\frac{K_1(\hat{\varrho}_{22}^{(0)} - \hat{\varrho}_{11}^{(0)}) + 4|\Omega_{31}|^2(\hat{\varrho}_{33}^{(0)} - \hat{\varrho}_{11}^{(0)})}{(4|\Omega_{31}|^2 + K_2)K_3}\,, \tag{3.37a}$$

$$\hat{\varrho}_{32} = 2\,\Omega_{32}\frac{K_4(\hat{\varrho}_{33}^{(0)} - \hat{\varrho}_{22}^{(0)}) + 4|\Omega_{31}|^2(\hat{\varrho}_{33}^{(0)} - \hat{\varrho}_{11}^{(0)})}{(4|\Omega_{31}|^2 + K_5)K_3}\,, \tag{3.37b}$$

while the populations obey

$$\hat{\varrho}_{11}^{(0)} = \frac{\gamma_3(K_6 + 4|\Omega_{31}|^2)}{K_7 + 4\gamma_2|\Omega_{31}|^2 + 8\gamma_3|\Omega_{31}|^2}\,, \tag{3.38a}$$

$$\hat{\varrho}_{22}^{(0)} = \frac{4\gamma_2|\Omega_{31}|^2}{K_7 + 4\gamma_2|\Omega_{31}|^2 + 8\gamma_3|\Omega_{31}|^2}\,, \tag{3.38b}$$

$$\hat{\varrho}_{33}^{(0)} = \frac{4\gamma_3|\Omega_{31}|^2}{K_7 + 4\gamma_2|\Omega_{31}|^2 + 8\gamma_3|\Omega_{31}|^2} \tag{3.38c}$$

where the $K_l, (l \in \{1, \dots 7\})$ are coefficients independent of Ω_{31}.

Again, the coherence $\hat{\varrho}_{ij}$ is determined by the difference of the populations of $\hat{\varrho}_{ii}^{(0)}$ and $\hat{\varrho}_{jj}^{(0)}$, $[(i,j) \in \{(2,1),(3,2)]$. For small $|\Omega_{31}|$, the term proportional to $\hat{\varrho}_{33}^{(0)} - \hat{\varrho}_{11}^{(0)}$ can be neglected. For large $|\Omega_{31}|$, this term outweighs the others at first sight. However, for $|\Omega_{31}| \to \infty$ and arbitrary, but fixed detunings, one finds

$$\hat{\varrho}_{11}^{(0)} \to \frac{1}{\frac{\gamma_2}{\gamma_3} + 2}\,, \tag{3.39a}$$

$$\hat{\varrho}_{22}^{(0)} \to \frac{1}{2\frac{\gamma_3}{\gamma_2} + 1}\,, \tag{3.39b}$$

$$\hat{\varrho}_{33}^{(0)} \to \frac{1}{\frac{\gamma_2}{\gamma_3} + 2}\,. \tag{3.39c}$$

Therefore, $\hat{\varrho}_{11}^{(0)} - \hat{\varrho}_{33}^{(0)} \to 0$ such that also in this case, $\hat{\varrho}_{ij}$ is determined by $\hat{\varrho}_{ii}^{(0)} - \hat{\varrho}_{jj}^{(0)}$.

Eqs. (3.39) also imply that for a strong control field, both probe transitions show opposite absorptive behavior (see Fig. 3.3): absorption in case of the upper probe transition, and amplification for the lower one. The reason is that due to the small decay rate γ_3, most population is trapped in state $|2\rangle$, such that the relevant population differences in Eqs. (3.37) have opposite sign. For small $|\Omega_{31}|$, Eqs. (3.38) yield $\hat{\varrho}_{11}^{(0)} > \hat{\varrho}_{22}^{(0)} > \hat{\varrho}_{33}^{(0)}$, which explains the absorptive properties in Fig. 3.3. However, the first inequality is not obvious and can only be deduced by an exact knowledge of K_6.

Before we come to the discussion of the cross terms, we would like to note that, of course, there are also differences between the direct terms of the two systems. We already discussed the AC Stark shift that occurs only in the loop system. But the closed-loop system also offers more degrees of freedom than the incoherently pumped system, most importantly Δ_1. The role of the control field detuning Δ_1 is shown in Fig. 3.4. In this figure, we plot the expansion coefficients of the direct terms in the coherence over the probe field detunings Δ_2 and Δ_3 for $\Delta_1 = 2\gamma$. The detuning Δ_1 essentially determines the position of one of the maxima of the imaginary part of the response function. Increasing Δ_1 moves the peak to higher frequencies, while decreasing it moves it to lower frequencies. For example, in Fig. 3.4, the corresponding maxima can be seen close to $\Delta_2 = 2\gamma$.

3.4.2 The cross terms

Let us now come to the most important difference between the two systems: The coherences of the closed-loop system have cross terms, while the coherences of the incoherently pumped system do not. However, as found in Sec. 3.3.1, the cross terms only contribute to the magnetic and electric response for $\Delta = 0$, i.e. for $\omega_p = \omega_c/2$.

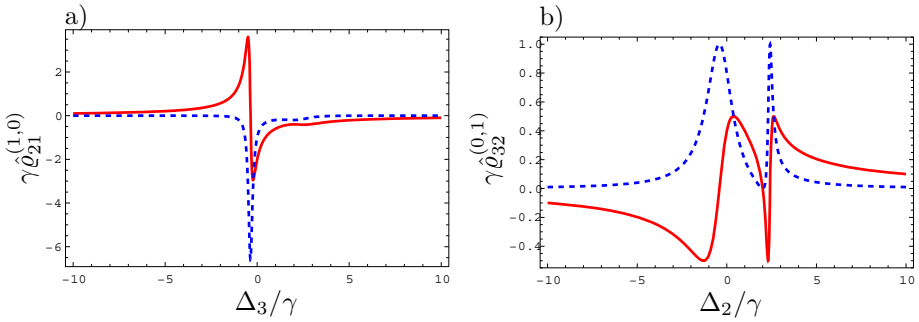

Figure 3.4: Real (red solid line) and imaginary part (blue dashed curve) of the expansion coefficients a) $\hat{\varrho}_{21}^{(1,0)}$ and b) $\hat{\varrho}_{32}^{(0,1)}$ in Eqs. (3.18). The curves are drawn for $\Delta_1 = 2\gamma$ in the closed-loop system. The coefficients are scaled by γ. The parameters are as in Fig. 3.2(a), except for the non-vanishing detuning of the control field.

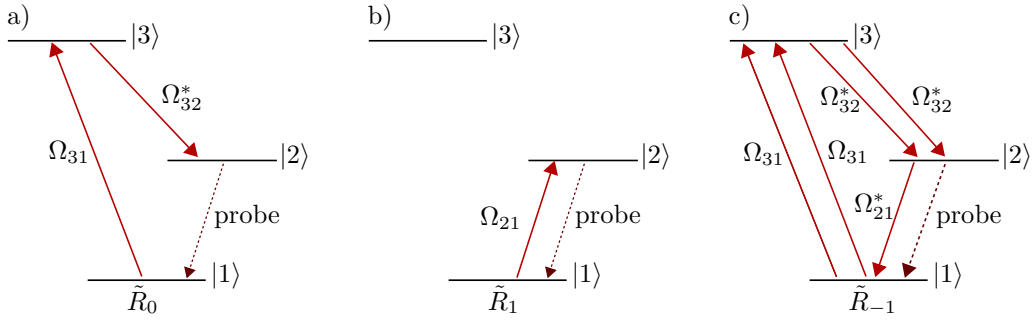

Figure 3.5: Interpretation of the different scattering processes that contribute to $\tilde{\varrho}_{21}$ in the case of $\Delta = 0$. a) $\tilde{R}_0$ contributes to the cross term in $\tilde{\varrho}_{21}$, and thus to the chirality $\tilde{\xi}_{HE}$. b) $\tilde{R}_1$ contributes to the direct term, i.e. to the magnetic susceptibility. c) $\tilde{R}_{-1}$ is of higher order in either one of the probe field Rabi frequencies and therefore negligible in our calculation.

The following comparison serves as basis for the conclusion which will be drawn in the discussion section regarding the enhancement of the magnetic response.

The mathematical origin of the cross terms can be identified from the derivation of the coherences in Section 3.3.1. The relevant response of the system to the probe field is given by the contributions of the respective probe transition coherences oscillating in phase with the incident probe field. According to this criterion, for $\Delta \neq 0$, only one of the terms in Eq. (3.26) contributes to each probe field coherence. In contrast, for $\Delta = 0$, all terms in Eq. (3.26) contribute to this response. The additional terms lead to the cross terms discussed here. In principle, also other terms contribute in this case, but they are of higher order in the probe field Rabi frequencies and can therefore be neglected in linear response theory.

How can we interpret the different contributions $\tilde{R}_k$ ($k \in \{-1, 0, 1\}$) to Eq. (3.26)

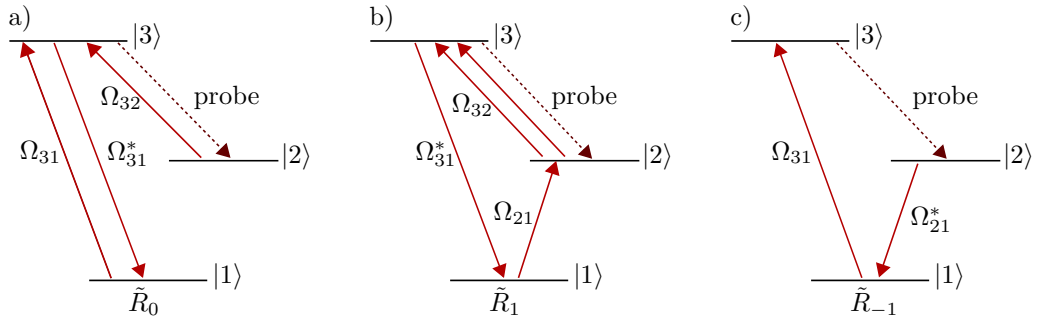

Figure 3.6: Interpretation of the different scattering processes that contribute to $\tilde{\varrho}_{32}$ in the case of $\Delta = 0$. a) $\tilde{R}_0$ contributes to the direct term in $\tilde{\varrho}_{32}$, and thus to the electric susceptibility. b) $\tilde{R}_1$ is of higher order in either one of the probe field Rabi frequencies and can therefore be neglected. c) $\tilde{R}_{-1}$ contributes to one of the cross terms, i.e., to one of the chirality coefficients.

physically? An explicit calculation reveals their dependence on the probe and control field Rabi frequencies. The control field Rabi frequencies appear for two different reasons. First, the populations depend on the control field Rabi frequencies. But second, the Rabi frequencies also indicate the physical process described by the respective terms. The obtained combinations of the different Rabi frequencies lead to an interpretation of $\tilde{R}_k$ as depicted in Figs. 3.5 and 3.6. For example, $\tilde{R}_0$ contributing to $\tilde{\varrho}_{21}$ is shown in Fig. 3.5(a). This term arises from the scattering of the control field off of transition $|1\rangle \rightarrow |3\rangle$ and the probe field off of transition $|3\rangle \rightarrow |2\rangle$ into the probe transition $|2\rangle \rightarrow |1\rangle$, which contributes to the magnetic response.

We now turn to a numerical study of the cross terms. In Fig. 3.7, we plot $\hat{\varrho}_{21}^{(0,1)}$, multiplied by a factor of γ to achieve unitless quantities. $\hat{\varrho}_{32}^{(1,0)}$ is not shown, as it is virtually identical for the chosen parameters. It is important to note that in Fig. 3.7, the cross terms are plotted over the variable σ which is defined as $\sigma = \frac{1}{2}(\Delta_3 - \Delta_2) = \omega_2 - \frac{1}{2}(\omega_3 + \omega_1)$. This new variable can be interpreted as the energy shift of state $|2\rangle$ with respect to the average energy of $|1\rangle$ and $|3\rangle$. Hence, in a plot against σ, effectively state $|2\rangle$ is moved. In this way, the probe field frequency remains fixed such that the multiphoton resonance condition $\Delta = 0 \Leftrightarrow \omega_p = \omega_c/2$ is fulfilled for all values of σ. For $\sigma = 0$, $|2\rangle$ lies in the very middle of $|1\rangle$ and $|3\rangle$.

It turns out that apart from the phases of the dipole moments, the chiralities in Eqs. (3.17) depend on the phase $\psi - 2\phi + \vec{K}\vec{r}$ arising from the closed interaction loop, where $\vec{K} = (\vec{k}_c - 2\vec{k}_p)$ is the so-called wave vector mismatch. For the plot in Fig. 3.7, we set all involved phases to zero. This does not affect our final conclusion regarding the enhancement of the magnetic response, since it will only be based on the magnitude of the cross terms. If in an experiment the difference between the absolute field phases $\psi - 2\phi$ is not fixed, then the chiralities average to zero.

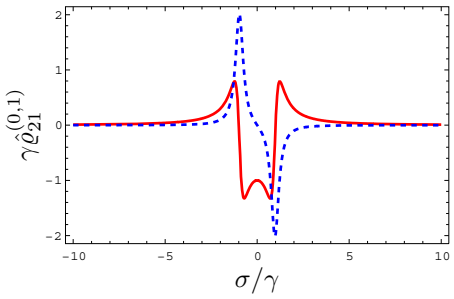

Figure 3.7: Real (red solid line) and imaginary part (blue dashed) of the expansion coefficient $\hat{\varrho}_{21}^{(0,1)}$ in the closed-loop system [see Eqs. (3.18)]. $\hat{\varrho}_{32}^{(1,0)}$ is not shown, since it is virtually identical to the shown results. The coefficients correspond to cross terms and determine $\tilde{\xi}_{HE}$ and $\tilde{\xi}_{EH}$, respectively. The plotted coefficients are phase-dependent; in this figure all phases are set to zero. The variable $\sigma = (\Delta_3 - \Delta_2)/2 = \omega_2 - (\omega_3 + \omega_1)/2$ denotes the shift of the eigenfrequency of $|2\rangle$ with respect to the average frequency of $|1\rangle$ and $|3\rangle$. Then, for all values of σ, the multiphoton resonance condition $\Delta = 0$ is fulfilled for a fixed probe field frequency ω_p.

While absolute phase control is very difficult to achieve, relative phase control has been accomplished experimentally [33]. In related systems, the phase dependence of the cross terms can be made independent of the probe field phase, as will be discussed in Sec. 3.5. The observed phase dependence is a characteristic of closed loop systems, and has been observed in related systems as well [41, 18]. The phase can be calculated by following the interaction loop, and counting phases of fields that de-excite the atom and phases of fields that excite the atom throughout this loop path with opposite sign.

Due to the dependence of the chiralities on $\vec{K}\vec{r}$, a further condition for the enhancement arises, namely, that the so-called wave vector mismatch should vanish, i.e. $\vec{K} = 0$. This condition on the relative propagation directions of the different fields for the enhancement to take place can be fulfilled, for example, for co-propagating fields [41].

3.4.3 Enhancement of the magnetic response

We are now in the position to evaluate the magnitude of the magnetic response. For this, we examine the different contributions in Eq. (3.21b). In particular, we compare the two contributions to the magnetization, which except for the common prefactor are given by

$$M_1 = d_{32}\mu_{21}\,\mathcal{E}_p\,e^{i\Phi}\,\hat{\varrho}_{21}^{(0,1)}\,, \tag{3.40a}$$

$$M_2 = \mu_{21}^2\,\mathcal{B}_p\,\hat{\varrho}_{21}^{(1,0)}\,. \tag{3.40b}$$

Here, M_1 refers to the cross term contribution that only contributes at $\Delta = 0$ and M_2 denotes the direct term.

First, Figs. 3.2 and 3.7 show that in the closed loop system,

$$|\hat{\varrho}_{21}^{(1,0)}| \approx |\hat{\varrho}_{21}^{(0,1)}| \,. \tag{3.41}$$

Thus, the magnitude of the two expansion coefficients is comparable. The size of the involved transition dipole moments can be estimated according to Eqs. (2.44) and therefore

$$\mu_{21}/d_{32} \sim \alpha c \,, \tag{3.42}$$

where μ_B is the Bohr magneton, e the elementary charge, a_0 the Bohr radius, α the fine-structure constant and c the vacuum speed of light. Finally,

$$\mathcal{B}_p = \frac{1}{c}\mathcal{E}_p \,. \tag{3.43}$$

With Eqs. (3.42) and (3.43), we thus arrive at

$$|M_1| \approx \alpha^{-1}|M_2| \,. \tag{3.44}$$

This means that at multiphoton resonance, the magnetic response of the closed-loop system is enhanced by a factor of α^{-1} due to the scattering of the electric probe field component into the magnetic probe transition (described by $\tilde{R}_0$ in Fig. 3.5). A similar argument shows that the direct terms of the incoherently pumped and the closed loop system are comparable in magnitude, such that the closed-loop system in multiphoton resonance also allows an enhancement of the magnetic response by α^{-1} as compared to the incoherently pumped system.

3.5 Discussion

We have seen that the direct response, which describes the polarization [magnetization] created by the electric [magnetic] probe field component, is of the same order of magnitude in all three cases considered in Sec. 3.3. Only at multiphoton resonance, the response of the closed-loop system in addition contains a term corresponding to the scattering of the electric probe field component into the magnetic probe field transition. In this section, we could show that this scattering effectively enhances the magnetic response by one inverse power of the fine structure constant α^{-1}, and thus clearly identify the mechanism leading to the enhanced magnetic response.

Of course, the reverse process of scattering the magnetic field into the electric probe field mode can also occur. However, Eqs. (3.21) show that this does not lead to an enhancement of the electric response, since, mathematically speaking,

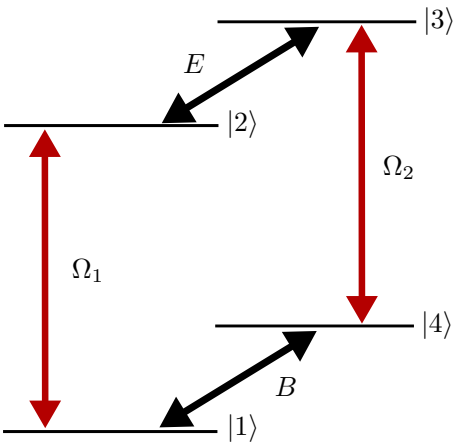

Figure 3.8: Example level scheme for magnetic response enhancement independent of the probe field frequency. Ω_1 and Ω_2 (in red) are coherent coupling fields with frequencies ω_1 and ω_2, respectively. E and B are the electric and magnetic component of the probe field with frequency ω_p (black). Here, the closed loop path contains an absorption and an emission of a probe field photon such that the multiphoton detuning $\Delta = \omega_1 - \omega_2$ can be satisfied for arbitrary probe field frequencies.

$|d_{32}^2\,\vec{E}_p| \sim \alpha^{-1}|d_{32}\,\mu_{32}\,\vec{B}_p|$. Physically speaking, the coupling of the magnetic probe field component to a magnetic transition is smaller than the coupling of the electric probe field component to an electric transition by a factor of α.

The multiphoton resonance condition restricts the magnetic enhancement in the system discussed here to a single probe field frequency. Extended closed-loop systems can be constructed in such a way that a complete loop contains an excitation on the electric probe transition and a de-excitation on the magnetic probe transition, or vice versa [17, 18]. A simple example for this is shown in Fig. 3.8. In such a system, the multiphoton resonance condition does not depend on the frequency of the probe field, such that it can be fulfilled for arbitrary probe field frequencies by suitably choosing the coupling field frequencies. The physical interpretation identified in our analysis directly carries over to these extended systems.

While the parametric enhancement by α^{-1} is universal, other closed-loop systems could in principle lead to a modification of the relative magnitude of the different expansion coefficients in Eq. (3.41). If this ratio can be altered favorably, then the enhancement can be even higher. It remains to be seen, however, whether there is a physical mechanism that enables one to change this ratio to a great extent.

3.6 Non-chiral closed-loop system

Having discussed the closed-loop system that couples to both the magnetic and the electric probe field component thoroughly, we now turn to a similar system, namely to a closed-loop system in which the probe field on transition $|2\rangle \rightarrow |3\rangle$ has been replaced by a control field. This means that, now, only the magnetic component of the probe field couples to our system. One advantage of this system over the systems considered in Sec. 2 is the bigger number of adjustable system parameters each of which can be changed to achieve a suitable shape for the magnetic susceptibility. Also, the investigation of this system is motivated by the hope that replacing a weak control field in a closed-loop configuration by a strong control field gives rise to a higher response on the magnetic probe transition $|1\rangle \rightarrow |2\rangle$.

This replacement changes the derivation of our results only slightly: We do not obtain an electric response, since the electric probe field does not couple to the system anymore. Therefore, the electric susceptibility $\tilde{\chi}_e$ and the chirality coefficient $\tilde{\xi}_{HE}$ of Eq. (3.12) vanish. If the electric probe field does not couple, transition $|2\rangle \rightarrow |3\rangle$ must either be of a frequency far away from the probe field frequency or a magnetic transition. In both cases, the magnetic probe field component cannot induce an electric response at the probe field frequency. Therefore, also the chirality coefficient $\tilde{\xi}_{EH}$ of Eq. (3.12) vanishes.

Besides that, the applied transformation according to Eq. (3.4) remains the same, i.e. $X = \Delta_1|1\rangle\langle 1| + \Delta_2|2\rangle\langle 2|$ in Eq. (3.4). However, note that now, $\Delta_1 = \omega_3 - \omega_1 - \omega_c$ and $\Delta_2 = \omega_3 - \omega_2 - \omega_{c,2}$, where $\omega_{c,2}$ is the frequency of the control field coupling to transition $|2\rangle \rightarrow |3\rangle$. With this notation, the equations of motion (3.6) do not change. However, note that the step from Eq. (3.28) to (3.29) in which we neglected the parts of $\hat{\varrho}_{21}$ that are of higher than first order in Ω_{32} is not performed anymore, since Ω_{32} now belongs to a strong control field. Therefore, the term in $\hat{\varrho}_{21}$ containing $\tilde{R}_{-1}$ cannot be neglected now. Also, $\tilde{R}_0$ (see Fig. 3.5 a)) and $\tilde{R}_{+1}$ (see Fig. 3.5 b)) change, since we take into account all orders of Ω_{32}. Still, keep in mind that the terms $\tilde{R}_0$ and $\tilde{R}_{-1}$ only contribute in case of multiphoton resonance, as they only oscillate at the probe field frequency in this case. Now, the multiphoton detuning which is still given by Eq. (3.7) evaluates to

$$\Delta = \omega_c - \omega_{c,2} - \omega_p \,, \tag{3.45}$$

and therefore the case of multiphoton resonance is given by

$$\omega_p = \omega_c - \omega_{c,2} \,. \tag{3.46}$$

As laid out in Sec. 3.3.1, $\tilde{\varrho}_{21}$ has the form given in Eq. (3.28), in which, again, one probe field frequency is replaced by the frequency $\omega_{c,2}$ of the second control field.

Therefore,

$$\begin{aligned}\hat{\varrho}_{21} = \quad & e^{-i(\omega_c-\omega_p-\omega_{c,2})t}\tilde{\varrho}_{21} \\ = \quad & e^{-i(\omega_c-\omega_p-\omega_{c,2})t}\,[\tilde{R}_0]_4 + \,[\tilde{R}_1]_4\Omega_{21} + \,e^{-2i(\omega_c-\omega_{c,2}-\omega_p)t}\,[\tilde{R}_{-1}]_4\Omega_{12} \\ = \quad & e^{-i(\omega_c-\omega_p-\omega_{c,2})t}\,[\tilde{R}_0]_4 + \,\Omega_{21}\left([\tilde{R}_1]_4 + \,e^{2i\phi_\Omega-2i(\omega_c-\omega_{c,2}-\omega_p)t}\,[\tilde{R}_{-1}]_4\right)\,.\end{aligned} \tag{3.47}$$

Here, ϕ_Ω denotes the phase of the Rabi frequency Ω_{12} and thus

$$\phi_\Omega = -\phi - \vec{k}_p\vec{r} - \phi_{21}\,. \tag{3.48}$$

As before, the quantities in this equation are determined by Eqs. (3.1) and (3.20).

Eq. (3.47) shows that $[\tilde{R}_1]_4$ determines the coherence of the magnetic probe transition and therefore the magnetic susceptibility (see Eq. (3.17)) if there is no multiphoton resonance. For $\omega_p = \omega_c - \omega_{c,2}$, the case of multiphoton resonance, $[\tilde{R}_0]_4$ and $[\tilde{R}_{-1}]_4$ both contribute to the magnetic response. However, $[\tilde{R}_0]_4$ does not include any probe field Rabi frequencies anymore. Thus, the contribution of this term is only caused by the control fields used to prepare the medium and not by the probe field. Therefore, we detect a response also when we switch off the probe field which is caused by the control fields.

Although $[\tilde{R}_{-1}]_4$ yields a response to the probe field at multiphoton resonance, a response to the control field superimposes both this contribution and the contribution of $[\tilde{R}_1]_4$ which we have at all frequencies. For an experimental realization or possible applications, this is supposedly unfavorable, since the response to the incident probe signal would be disturbed. Therefore, we concentrate on the case that the multiphoton condition of Eq. (3.46) is not fulfilled ($\Delta \neq 0$). This is easy to realize, since one can simply choose the control field frequencies in such a way that the probe field frequency only fulfills the multiphoton condition at a frequency very different from the near-resonant frequencies we consider.

Numerical results

For $\Delta \neq 0$, only $[\tilde{R}_1]_4$ contributes and we obtain the susceptibilities of Fig. 3.9. Again, we choose a particle density of $N = 1\ \mathrm{m}^{-3}$. In a), we assumed electric control field transitions and therefore chose the parameters $\gamma_1 = \alpha^{-2}\gamma$, $\gamma_2 = \alpha^{-2}\gamma$, $\gamma_3 = \gamma$ and $\lambda = 600\,\mathrm{nm}$. Moreover, $r_1 = r_2 = r_3 = 0$, $\Delta_1 = 0$, $\Delta_2 = -24\alpha^{-2}\gamma$, $|\Omega_{31}| = 37\alpha^{-2}\gamma$ and $|\Omega_{32}| = 18\alpha^{-2}\gamma$. b) shows the case of magnetic control field transitions, i.e. of a system with $\gamma_1 = \gamma_2 = \gamma_3 = \gamma$ and $\lambda = 600\,\mathrm{nm}$. Also,

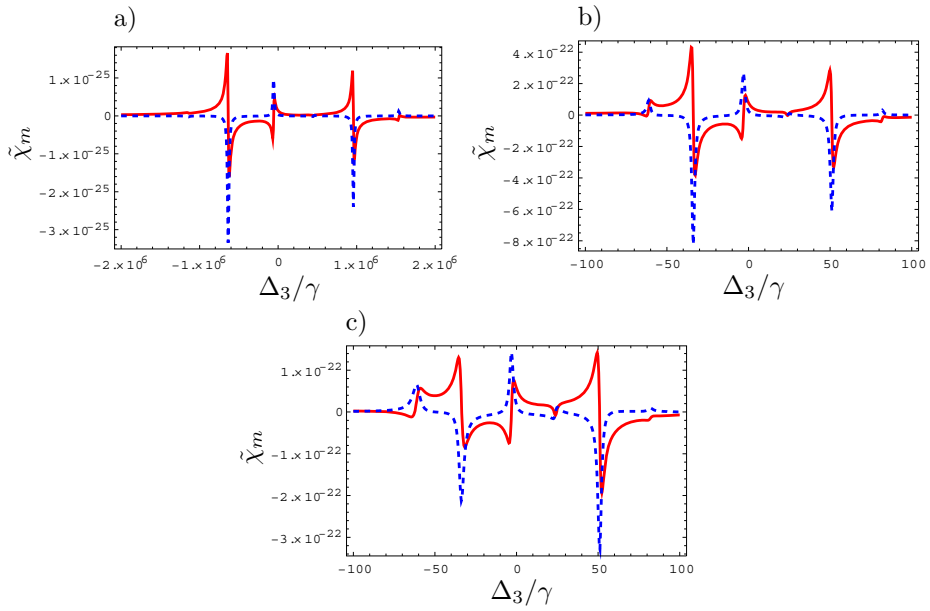

Figure 3.9: The magnetic susceptibility in the given closed-loop system has a rich structure for the chosen parameters. We plotted the susceptibility for a particle density of $N = 1m^{-3}$ and in a) for a system with two electric control field transitions, in b) with two magnetic control field transitions and in c) for a nitrogen system. The values for the detunings and the control field Rabi frequencies were adapted to the different decay rates in a), b) and c).

$r_1 = r_2 = r_3 = 0$, $\Delta_1 = 0$, $\Delta_2 = -24\gamma$, $|\Omega_{31}| = 37\gamma$ and $|\Omega_{32}| = 18\gamma$. Finally, the susceptibility of the nitrogen-like system of Fig. 3.9 c) was calculated with the parameters $\gamma_1 = 3.92\gamma$, $\gamma_2 = 1.86 \cdot 10^{-3}\gamma$, $\gamma_3 = \gamma$ and $\lambda = 520.1705\,\text{nm}$. Similarly as before, $r_1 = r_2 = r_3 = 0$, $\Delta_1 = 0$, $\Delta_2 = -24\gamma$, $|\Omega_{31}| = 37\gamma$ and $|\Omega_{32}| = 18\gamma$.

Fig. 3.9 shows a rich structure. Also, there are a few interesting points. These are, for the nitrogen parameters, $\Delta_3 \approx -13\gamma$, $\Delta_3 \approx 24\gamma$ and $\Delta_3 \approx 71\gamma$. At these detunings, we obtain a negative real part and a vanishing imaginary part. However, at $\Delta_3 \approx 24\gamma$, the shape of the susceptibility is not as optimal as at the other points. The real part only reaches values of $\text{Re}(\tilde{\chi}_m) \approx -9 \cdot 10^{-23}$. Such a comparably small absolute value of the real part demands a high particle density, since what we aim for is a large permeability which is connected to the magnetic susceptibility by Eq. (1.1b). Also, the range of frequencies over which the real part is negative and the imaginary part is small is comparably narrow.

However, let us have a closer look at $\Delta_3 \approx -13\gamma$ and $\Delta_3 \approx 71\gamma$. At these detunings, the real part of the magnetic susceptibility is negative. At the same point, the imaginary part vanishes and has a small gradient, such that the absorption stays

small in a range of few γ around the considered points. Also, these points appear for all three different sets of system parameters in Fig. 3.9 a), b) and c). These points are good candidates for negative refraction.

Also, as in Sec. 2, the system with only magnetic transitions yields the highest absolute values for the magnetic susceptibility, while the size of the magnetic susceptibility in the nitrogen-like system is only slightly smaller. In Sec. 2, the difference between the susceptibilities of these two systems was much bigger. Thus, in Sec. 4, we will consider the closed-loop system with nitrogen parameters, since it describes a real, existing atomic species, yields a high response and therefore is a good candidate for negative refraction and a possible experimental realization.

Chapter 4

The index of refraction in atomic two-component media

4.1 Theoretical preparation

So far, we have considered the electric and, in particular, the magnetic response of a two-component medium. We know how to calculate the electric and magnetic susceptibilities $\tilde{\chi}_e$ and $\tilde{\chi}_m$ of each species of atoms, respectively, at the probe field frequency (see Secs. 2.1.2 and 3.2.3). Also, permittivity ε_r and permeability μ_r are given by

$$\varepsilon_r = \tilde{\chi}_e + 1 \,, \tag{4.1a}$$
$$\mu_r = \tilde{\chi}_m + 1 \,. \tag{4.1b}$$

In a homogeneous, i.e. one-component medium, we can combine permittivity and permeability to the index of refraction by Eq. (1.2), which we recall here, since this equation is the core of the following section:

$$n^2 = \varepsilon_r \mu_r \,. \tag{4.2}$$

This equation can be found in any standard book of electrodynamics, e.g. [19]. The equation leads to two solutions for the index of refraction, namely

$$n = \pm\sqrt{\varepsilon_r \mu_r} \,, \tag{4.3}$$

of which only one is causal and the other one belongs to a superluminal signal velocity. In the following, we will call one solution n_-, namely $n_- = -\sqrt{\varepsilon_r \mu_r}$, while

the other solution will be denoted by $n_+ = \sqrt{\varepsilon_r \mu_r}$. To choose the right solution here will be the topic of Sec. 4.1.2. Before we do that, we have to take a closer look at Eq. (4.2), the equation that combines electric and magnetic response. This equation holds in the case of a single-component medium yielding both a magnetic and an electric response. In contrast, we deal with two components of a medium that each yield a magnetic and an electric response respectively. How do we have to combine the susceptibilities of both components to a total susceptibility in this case ? In other words, does Eq.(4.2), with ε_r being the permittivity of one component and μ_r the permeability of the other component, still hold for such a setup ?

4.1.1 Combining two atomic media

Let us consider a medium consisting of two components, species A and species B. Both components are charge free and nonconducting. According to Eqs. (3.9), the electric polarization in the two-component medium is given by

$$\vec{P}(\vec{r},t) = \frac{1}{c}\int_{-\infty}^{\infty} \xi_{EH}(\tau)\, \vec{H}(\vec{r},t-\tau)\, d\tau + \varepsilon_0 \int_{-\infty}^{\infty} \chi_e(\tau)\, \vec{E}(\vec{r},t-\tau)\, d\tau\,. \tag{4.4}$$

On the other hand, microscopically, the polarization can be obtained by Eq. (3.13),

$$\vec{P} \;=\; N\vec{p}\,, \tag{4.5}$$

where N is the particle density and $\vec{p}$ is the mean polarization per atom [23]. In the same way one can calculate the polarization of a two component medium, since Eq. (4.5) can be written in an explicit way as

$$\vec{P} = \frac{1}{V}\sum_{i=1}^{a+b} \vec{p_i}\,, \tag{4.6}$$

where a and b are the numbers of atoms of species A and B, respectively. V is the volume our two-component medium occupies and $\vec{p_i}$ is the mean electric dipole moment of the atom labelled i. It can be calculated as the expectation value of the electric dipole operator $\vec{d_i}$ of atom i as

$$\vec{p_i} = \mathrm{Tr}(\varrho \vec{d_i})\,. \tag{4.7}$$

Since the atoms are identical within their own species, the mean electric dipole moment of each atom of species A is the same. We can therefore call it $\vec{p}_A$ and deal analogously with species B. Therefore,

$$\vec{P} = \frac{1}{V}\sum_{i=1}^{a+b}\vec{p}_i = \underbrace{\frac{a}{V}\,\vec{p}_A}_{\vec{P}_A} + \underbrace{\frac{b}{V}\,\vec{p}_B}_{\vec{P}_B} \tag{4.8}$$

The electric susceptibilities of species A and B, $\chi_{e,A}$ and $\chi_{e,B}$ are defined in the same way as the total electric susceptibility χ_e, but with the polarizations $\vec{P}_A$ and $\vec{P}_B$ of the two species respectively instead of the total polarization $\vec{P}$. Thus, we finally obtain

$$\begin{aligned}
& \frac{1}{c}\int_{-\infty}^{\infty}\xi_{EH,A}(\tau)\,\vec{H}(\vec{r},t-\tau)\,d\tau + \varepsilon_0\int_{-\infty}^{\infty}\chi_{e,A}(\tau)\,\vec{E}(\vec{r},t-\tau)\,d\tau \\
& + \frac{1}{c}\int_{-\infty}^{\infty}\xi_{EH,B}(\tau)\,\vec{H}(\vec{r},t-\tau)\,d\tau + \varepsilon_0\int_{-\infty}^{\infty}\chi_{e,B}(\tau)\,\vec{E}(\vec{r},t-\tau)\,d\tau \\
= \quad & \vec{P}_A + \vec{P}_B = \vec{P} \\
= \quad & \frac{1}{c}\int_{-\infty}^{\infty}\xi_{EH}(\tau)\,\vec{H}(\vec{r},t-\tau)\,d\tau + \varepsilon_0\int_{-\infty}^{\infty}\chi_e(\tau)\,\vec{E}(\vec{r},t-\tau)\,d\tau\,.
\end{aligned} \tag{4.9}$$

This implies

$$\chi_e = \chi_{e,A} + \chi_{e,B}\,. \tag{4.10}$$

This additivity also holds for the Fourier transformed quantities $\tilde{\chi}_e$, $\tilde{\chi}_{e,A}$ and $\tilde{\chi}_{e,B}$, since we can write Eq. (4.9) in terms of Fourier transformed quantities as in Eq. (3.12). Analogously, this additivity can be derived for the magnetic susceptibility $\tilde{\chi}_m$.

Since $\epsilon_r = 1 + \tilde{\chi}_e$ and $\mu_r = 1 + \tilde{\chi}_m$, we finally have

$$n^2 = \epsilon_r\mu_r = (1+\tilde{\chi}_e)\cdot(1+\tilde{\chi}_m) \tag{4.11}$$

where both susceptibilities can be obtained by adding the susceptibilities of component A and B (see Eq. (4.10)). In a gas in which species A only yields an electric, species B a magnetic response, we simply have e.g. $\chi_e = \chi_{e,A}$ and $\chi_m = \chi_{m,B}$, since $\chi_{e,B} = \chi_{m,A} = 0$. This is the case in our configuration.

Note that in Eq. (4.11), the susceptibilities depend on different detunings, e.g. $\chi_e = \chi_e(\Delta_e)$ and $\chi_m = \chi_m(\Delta_m)$. Here, Δ_e is the detuning of the electric probe field component with respect to the probe transition in the electrically coupling medium. Analogously, Δ_m is the detuning of the magnetic probe field component with respect to the magnetic probe transition of the other species of atoms. To plot the index

of refraction over the probe field frequency (or a detuning including the probe field frequency), we have to use

$$\Delta_e = \Delta_m + \omega_{i_e} - \omega_{j_e} - (\omega_{i_m} - \omega_{j_m}) \,. \tag{4.12}$$

Here, $\omega_{i_e} - \omega_{j_e}$ is the transition frequency of the probe transition of the electrically coupling atoms, $\omega_{i_m} - \omega_{j_m}$ is the transition frequency of the probe transition of the magnetically coupling atoms. If we use this relation in Eq. (4.11), the index of refraction only depends on Δ_e, the probe field detuning of one of the two species.

4.1.2 Finding the right solution for the refractive index

Now, we know how to calculate the index of refraction. However, we still have to determine the physical solution of Eq. (4.3). There are several criteria for negative refraction in the literature [42]. However, these criteria can only be employed in special cases that are given by the signs of μ_r and ε_r and some of them only work for passive media. In contrast, we introduce two algorithms that are based on basic physical properties of the index of refraction: continuity.

Continuity with respect to system parameters

Systems that do not contain any incoherent pump rates or coherent fields, so-called passive systems, naturally have to be absorbing, since the population will necessarily decay to the lowest state with time. Then, however, the system must be absorbing, since there is no population inversion. Let us recall that the imaginary part of the index of refraction determines the absorptive behavior of the medium: A negative imaginary part implies gain, a positive imaginary part stands for absorption. Therefore, passive systems must have a refractive index with a positive imaginary part. Since the two solutions of Eq. (4.3) have imaginary parts with opposite signs, one can unambiguously find the physical solution for a passive system.

We now take advantage of this knowledge: Increasing all coherent and incoherent pump rates from zero to certain final values steadily turns our system from a passive to an active system. In the following, let us combine these parameters that determine the "passivity" of our two-component system, i.e. the incoherent and coherent pump rates, to the vector $\vec{x}$. Then, for $\vec{x} = \vec{0}$, the system is passive. The index of refraction not only depends on the frequency, i.e. the probe field detuning Δ_α, but also on these parameters: $n = n(\Delta_\alpha, \vec{x})$. Now, a slight change of $\vec{x}$ from $\vec{x}_0$ to $\vec{x}_0 + d\vec{x}$ should also only change n slightly. More precisely, $|n(\Delta_\alpha, \vec{x}_0) - n(\Delta_\alpha, \vec{x}_0 + d\vec{x})|$ can become arbitrarily small for arbitrarily small $\|d\vec{x}\|$. This holds for each $\Delta_\alpha \in \mathbb{R}$ and physical values of $\vec{x}_0$: the refractive index is continuous with respect to $\vec{x}$ [18].

Now, we pick an arbitrary, but fixed detuning Δ_α. For each detuning, we proceed as follows: We select the physical solution at $\vec{x} = \vec{0}$ (passive system), which can be determined by the fact that the imaginary part has to be positive. Then, we change $\vec{x}$ from $\vec{x} = \vec{0}$ continuously to the parameter values $\vec{x}_f$ for which we want to obtain the physical solution. While changing $\vec{x}$, $n(\Delta_\alpha, \vec{x})$ changes continuously. At $\vec{x}_f$, we then take the solution to which the physical solution at $\vec{x} = \vec{0}$ evolved. In such a way, the physical solution for the index of refraction can be found for any value of the detuning Δ_α and arbitrary parameter sets $\vec{x}_f$, unless there is no physical solution due to instabilities (see Sec. 4.1.4).

The principle of the approach is illustrated in Fig. 4.1. The solution $n_- = -\sqrt{\varepsilon_r \mu_r}$ is plotted in red, solution $n_+ = \sqrt{\varepsilon_r \mu_r}$ in green. At $\vec{x} = \vec{0}$, as the two solutions, we obtain the green and red circle. However, n_- — the red circle — is the physical solution, since it has a positive imaginary part. We then change $\vec{x}$ continuously, which causes the corresponding solutions for the index of refraction to move along the plotted green and red line. When we arrive at $\vec{x}_f$, the physical solution is still given by n_-. This point is marked by a red square.

In the discussed figure, we chose a system built up of a two-component system coupling electrically and an upper microwave system for the species that couples magnetically to the probe field. A deeper discussion of this system will follow in Sec. 4.2.2. For now, we will use it to demonstrate the used methods and the occurring problems.

Continuity with respect to the detuning

A second algorithm that we can apply to find the physical solution for the index of refraction and its dependence on the detuning at a fixed, arbitrary parameter set $\vec{x}_f$ is based on the fact that the index of refraction is a continuous function with respect to frequency and detuning, respectively.

The principle of this algorithm is depicted in Fig. 4.2. To start, we calculate all roots of $\mathrm{Re}(n_-)$. We could also take n_+, as $n_+ = -n_-$ both have the same roots. Let us call them $\delta_1, \delta_2, ... \delta_f$, where f is the total number of roots. We label them in such a way that $\delta_1 < \delta_2 < \ ... \ < \delta_f$. Now, we know that for the physical solution of the index of refraction we have the boundary condition $n(\Delta_\alpha, \vec{x}) \to 1$ for $|\Delta_\alpha| \to \infty$. Thus, for detunings $\Delta_\alpha < \delta_1$, we pick the very solution out of n_+ and n_- that has a positive real part.

Then, we proceed to determine the physical solution in the detuning range $\delta_1 < \Delta_\alpha < \delta_2$. There, we simply select the solution out of n_+ and n_- that has a negative real part. In this way, we proceed until we have reached δ_f. Therefore, the physical solution has a negative imaginary part in areas $\delta_k < \Delta_\alpha < \delta_{k+1}$, where k is an integer, but odd number.

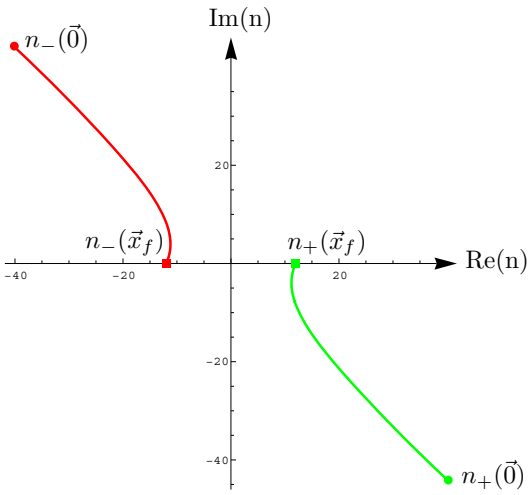

Figure 4.1: The physical solution for the index of refraction in a passive system ($\vec{x} = \vec{0}$) can be identified based on the principle we depict here. Since the imaginary part of the index of refraction has to be positive in such a case, the physical solution in our case is $n_-(\vec{0})$. The solution that we obtain by changing $\vec{x}$ from $\vec{0}$ to $\vec{x}_f$ continuously is $n_-(\vec{x}_f)$. As an example, we chose the configuration of Sec. 4.2.2, an electrically coupling two-level system and a magnetically coupling upper microwave system. The plotted indices of refraction have been obtained for a probe field detuning of the magnetic component of $\Delta_\alpha = -9\gamma$.

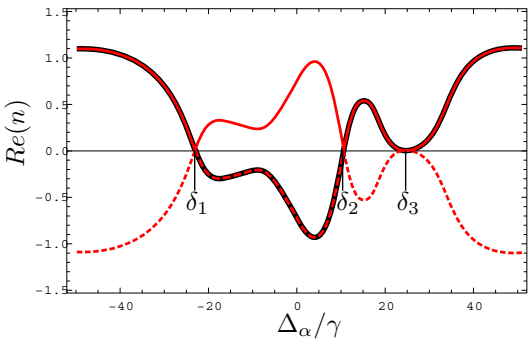

Figure 4.2: A second possibility to determine the physical solution of the index of refraction (black) out of the two solutions $n_- = -\sqrt{\mu_r \varepsilon_r}$ (dashed, red) and $n_+ = \sqrt{\mu_r \varepsilon_r}$ (continuous, red) is based on continuity in detuning direction. We show only real parts. The curves are fictional and only serve illustration purposes.

Let us explain the idea of this algorithm: Suppose that we choose the other solution, say we choose the solution with positive real part in the range $\delta_1 < \Delta_\alpha < \delta_2$. Then, the imaginary part would not be continuous at δ_1 — as long as it does not happen to be also zero at δ_1. However, if both imaginary part and real part of the index of refraction are zero at one detuning, we speak of a so-called branch point of the complex root function. These branch points cause instabilities of the medium (see Sec. 4.1.3 and 4.1.4). Therefore, we will restrict ourselves to parameter sets for which these branch points do not appear. Thus, these points cannot make the algorithm fail.

However, it is possible that the algorithm fails at roots of the real part of n with multiplicities higher than one. Such a point is shown in Fig. 4.2 at δ_3. If we assume that δ_3 is a root with multiplicity two, the algorithm still works, since this root will be counted twice and therefore we choose the same sign at $\Delta_\alpha > \delta_3$ as at $\delta_2 < \Delta_\alpha < \delta_3$. However, if the multiplicity is an odd number, the solution with the wrong sign will be picked. To avoid these possible problems, one could take the continuity of the imaginary part at the roots of the real part into account. However, we test all — in view of negative refraction — interesting results that we obtain by the described algorithm by hand. To do so, we verify that the boundary condition $n(\Delta_\alpha, \vec{x}) \to 1$ for $|\Delta_\alpha| \to \infty$ and the continuity of real and imaginary part are fulfilled. At no point, we found that our algorithm failed. Also, it is considerably faster than the one described in the previous paragraph, since we do not have to go through different values for $\vec{x}$ for every single detuning Δ_α. Therefore, to produce our results, we will use the algorithm described in this section.

4.1.3 Effects of branch points on the algorithms

We can now apply one of the to described algorithms - preferably the second one described in Sec. 4.1.2, as it is faster - to determine the index of refraction. The value of the index of refraction at $\Delta_\alpha = -9\gamma$ for $\vec{x} = \vec{x}_f$ in Fig. 4.1 seems to be exactly what we are looking for. It has a vanishing imaginary part and a negative real part. However, we encounter some difficulties there and also for other parameter sets. For these critical parameter sets, our two algorithms produce different and in both cases obviously non-physical outputs shown in the following section. These problems are related to so-called branch points of the index of refraction which imply physical instabilities of the medium, as will be discussed in Sec. 4.1.4. It is therefore not our algorithms that fail, but there rather is no physical solution for the index of refraction in Fourier space [43, 44]. Before we come to the discussion of the mentioned branch points, let us first describe the occurring problems for both algorithms.

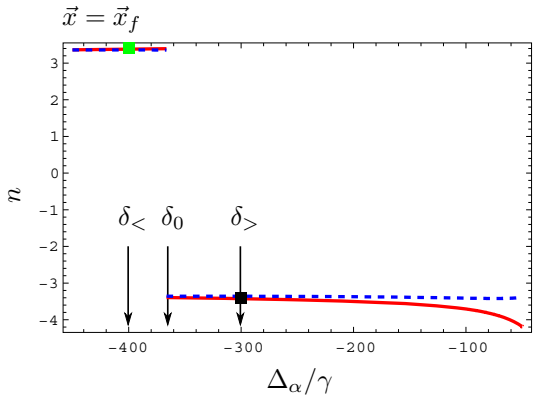

Figure 4.3: The solution for the index of refraction (real part: continuous red line, imaginary part: dashed blue line) at $\vec{x} = \vec{x}_f$ obtained by the first algorithm of Sec. 4.1.2 shows a discontinuity at some detuning δ_0. The squares mark the detunings $\delta_<$ and $\delta_>$ for which we plotted the dependence of the index of refraction on $\vec{x}$ in 4.5.

Continuity with respect to system parameters

The first algorithm described in Sec. 4.1.2 uses the continuity in $\vec{x}$-direction. However, strictly following the described algorithm for $\vec{x} = \vec{x}_f$ in our exemplary system leads to the plot shown in Fig. 4.3. The figure shows the imaginary part of the refractive index as a dashed, blue line, the real part as a solid, red line. This plot shows a discontinuity at $\Delta_\alpha = \delta_0$. In principle, to fix the discontinuity, one could switch the sign of the index of refraction for $\Delta_\alpha > \delta_0$, thereby choosing the respective other solution of n_- and n_+. However, since we obtained the plot through continuity arguments in $\vec{x}$-direction, the plot fulfills the boundary condition $n(\Delta_\alpha, \vec{x}) \to 1$ for $\Delta_\alpha \to \infty$. If we now switch signs for $\Delta > \delta_0$, this boundary condition is no longer fulfilled. Therefore, we cannot fix the algorithm in this way.

Since we do not have a discontinuity at $\vec{x} = \vec{0}$, but one at $\vec{x} = \vec{x}_f$, there has to be a value $\vec{x}_c$, that $\vec{x}$ takes on when we change it from $\vec{0}$ to $\vec{x}_f$, at which the discontinuity appears for the first time. Fig. 4.4 shows plots of the obtained solutions for two values $\vec{x}_0$ and $\vec{x}_0 + d\vec{x}$. Both lie close to the point $\vec{x}_c$ at which the discontinuity appears and $\|\vec{x}_0\| < \|\vec{x}_c\| < \|\vec{x}_0 + d\vec{x}\|$. At $\vec{x}_0$, the plot is still continuous, at $\vec{x}_0 + d\vec{x}$, it is not.

For clearness, we illustrate in Fig. 4.5 the development of the discontinuity in the complex plane that we already used in Fig. 4.1. If we plot the physical solution for the index of refraction at $\vec{x} = \vec{0}$ as a circle in the complex plane, we can draw a line that illustrates how it changes when changing $\vec{x}$. As mentioned, this line ends in the physical solution at $\vec{x}_f$, marked by a square in Fig. 4.5. We can do this at

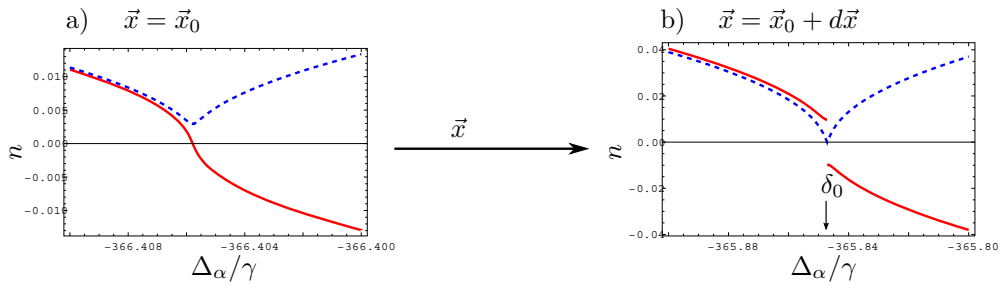

Figure 4.4: If we plot the solution for the index of refraction obtained by the first algorithm of Sec. 4.1.2 at the two specially chosen values $\vec{0}$ (in a)) and $\vec{x} + d\vec{x}$ (in b)) of $\vec{x}$, we can see how the at δ_0 discontinuity is created. As usual, real parts are plotted with a continuous red line, imaginary parts with a dashed blue line.

two different detunings $\delta_<$ (green) and $\delta_>$ (black) that obey $\delta_< < \delta_0 < \delta_>$, where δ_0 is the point of discontinuity in Fig. 4.3. The squares also mark the corresponding points in Fig. 4.3. One can see that, while the physical solutions at $\vec{x} = \vec{0}$ of both detunings (circles) do not differ much in real and imaginary part, the solutions for $\vec{x}_f$ (squares) have totally opposite real and imaginary parts.

In short, the claim of continuity in $\vec{x}$-direction leads to discontinuities in detuning/frequency direction.

Continuity with respect to the frequency

Can we perhaps use the other algorithm, i.e. the second one described in Sec. 4.1.2 to obtain a physically correct solution without discontinuities for $\vec{x} = \vec{x}_f$? As it turns out, we cannot, since for $\vec{x} = \vec{x}_f$ the real part of (n_- has only one root which is shown in Fig. 4.6. Therefore, if we assume that the real part of the physical solution changes its sign at the root, we cannot fulfill the boundary condition $n(\Delta_\alpha, \vec{x}) \to 1$ for $|\Delta_\alpha| \to \infty$ (see Fig. 4.6). If we assume that the real part does not change its sign, the corresponding imaginary part is discontinuous. This problem occurs for any odd number of roots of $\mathrm{Re}(n_-)$.

If we do not fulfill the boundary condition for $\Delta_\alpha \to \infty$, we also violate continuity in $\vec{x}$-direction for high positive detunings, since the physical solution at $\vec{x} = \vec{0}$ fulfills the boundary condition. Therefore, we can say that here, the claim of continuity in detuning or frequency direction leads to a discontinuity in $\vec{x}$-direction.

Let us now come to an explanation of the discontinuity in Fig. 4.3 and the non-fulfillment of the boundary conditions in Fig. 4.6 which can be interpreted as a discontinuity in $\vec{x}$-direction as mentioned.

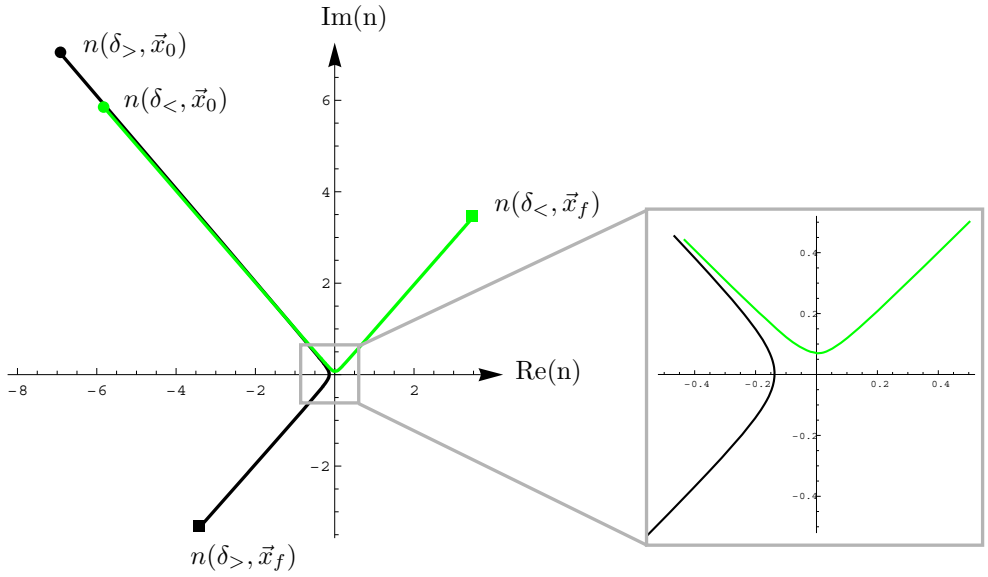

Figure 4.5: We show a plot of the physical solution at a fixed detuning as obtained by the first algorithm of Sec. 4.1.2 and how it changes when we change $\vec{x}$, analogously to Fig. 4.1. However, in this figure, the two lines correspond to the physical solutions - or, at least, what the algorithm returns us - at different detunings $\delta_<$ (green line) and $\delta_>$ (black line) that obey $\delta_< < \delta_0 < \delta_>$. The circles mark the start points ($\vec{x} = \vec{0}$), the squares mark the end points ($\vec{x} = \vec{x}_f$).

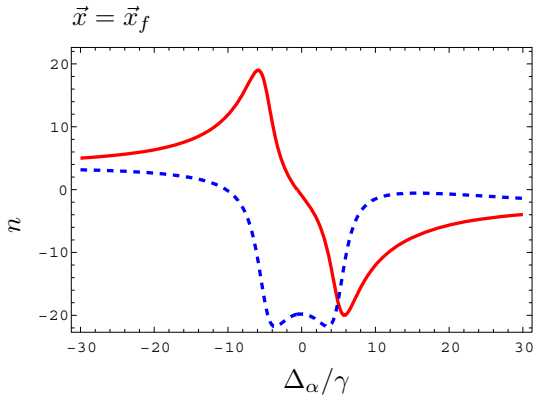

Figure 4.6: The second algorithm of Sec. 4.1.2 results in a solution for the index of refraction as plotted here (real part: continuous red line, imaginary part: dashed blue line). However, if one continues this plot to detunings approaching $+\infty$, one can see that the boundary condition $n(\Delta_\alpha, \vec{x}) \to 1$ is not fulfilled there.

4.1.4 Branch points

As Johannes Skaar points out in [43] that so-called branch points, in our case the branch points of the complex root function, can cause problems when one wants to determine the refractive index. First, we will demonstrate how the branch points create our problem shown in Figs. 4.4 and 4.6. Then, we will describe two ways to solve the issue, one of which we will use to obtain results for negative refraction.

Let us first clarify what a branch point is. In [45], a branch point is defined as " an isolated singular point b of an analytic function f(z) of one complex variable z such that the analytic continuation of an arbitrary function element of $f(z)$ along a closed path which encircles b yields new elements of $f(z)$". Let us explain this in our own words: In our case, where $f(z) = \sqrt{z}$, $z = n^2 \in \mathbb{C}$, is the complex square root, the only branch point is $z = 0$. We can characterize it by following fact: We draw a circle $c(t) = r \cdot e^{i(t+t_0)}$ of arbitrary small radius r around our branch point $z = 0$. Here, t_0 is arbitrary. Therefore, the starting point $c(0)$ is also arbitrary. We now begin at this starting point, where f has the value $f(c(t = 0)) = \sqrt{r}e^{it_0/2}$. Now, let us change t from 0 to 2π to close our circle, causing $f(c(t))$ to change continuously when changing t. For $t = 2\pi$, we are at the starting point again, i.e. $c(t = 0) = c(t = 2\pi)$. However, for $t \to 2\pi$, $f(c(t))$ approaches the value $f(c(t)) \to -\sqrt{r}\, e^{it_0/2}$ and not the value it had at the starting point $f(c(t = 0)) = \sqrt{r}\, e^{it_0/2}$. This is the very character of a branch point. A closed curve around it leads from one functional value to a different one, although end and starting point are the same (see also Fig. 4.7, where the branch point is marked by a black circle).

As shown, the point $z = n^2 = 0$ has this property with respect to the complex root function. However, we need the complex root in order to calculate the index of refraction (see Eq. (4.3)). In order to speak about branch points, we now go from real detunings Δ_α to complex detunings. In a further step, let us switch from detunings to probe field frequencies. Both are connected via

$$\Delta_\alpha = \omega_{i_0} - \omega_{j_0} - \omega_p \,, \tag{4.13}$$

where ω_{i_0} and ω_{j_0} denote the eigenenergies of the upper state $|i_0\rangle$ and the lower state $|j_0\rangle$ of the probe transition, respectively. Therefore, by "complex plane", we refer to the plane built up by the real and the imaginary parts of ω_p.

In passive systems ($\vec{x} = \vec{0}$), $n(\omega_p)$ only has branch points in the lower half of the complex plane which is implied by causality and the Kramers-Kronig relations [43]. However, in active systems, there can be branch points z_i with $\mathrm{Im}(z_i) > 0$. This is also the case for our exemplary combination of a two-level scheme and an upper microwave scheme at $\vec{x} = \vec{x}_f$ we used in Figs 4.1, 4.3, 4.4, 4.5 and 4.6. Therefore, there has to be a value $\vec{x}_1$ of $\vec{x}$ with $0 < \|\vec{x}_1\| < \|\vec{x}_f\|$ at which a branch point z_1 lies on the real frequency axis and therefore $\mathrm{Im}(z_1) = 0$. As it turns out, this is exactly

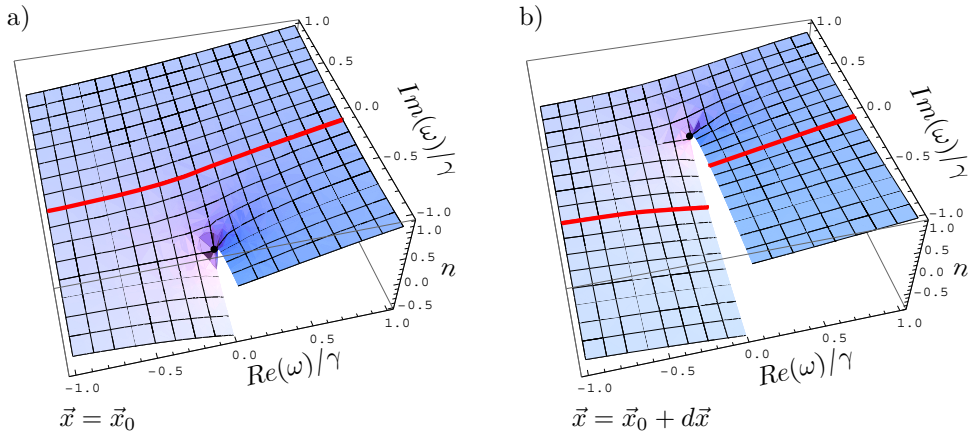

Figure 4.7: For illustration purposes, we show the real part of an exemplary index of refraction n. We chose the branch cut that is due to the root function to be parallel to the imaginary axis to illustrate the encountered problem. Note that the red line is reflected at the axis of ordinates with respect to Fig. 4.4, since we show the frequency plane. In Fig. 4.4, we showed the detuning axis, which is related to the real frequency by a factor of minus one (and some additive constant) according to Eq. (4.13). The refractive index is given at the parameters $\vec{x}_0$ in a) and at $\vec{x}_0 + d\vec{x}$ in b). The black circles mark the branch point.

the case for the value of $\vec{x} = \vec{x}_c$ for which the discontinuity appears - somewhere between $\vec{x}_0$ and $\vec{x}_0 + d\vec{x}$ in Fig. 4.4. Thus, it is not our algorithms that fail. In fact, there is no physical, continuous solution for the index of refraction.

One obtains a good notion of how the branch points cause the outputs of Figs. 4.3 and 4.6 by the function shown in Fig. 4.7. The figure shows the real part of an exemplary index of refraction in the complex frequency plane. In a), at $\vec{x} = \vec{x}_0$, the branch point — marked by a black circle — has a negative imaginary part. The red line shows the refractive index along the real axis, which is what we see in Fig. 4.4 a). When we change $\vec{x}$ from $\vec{x}_0$ to $\vec{x}_0 + d\vec{x}$, the branch point moves in the direction of the positive imaginary axis, such that in Fig. 4.7 b), it has a positive imaginary part. Every point of the red line has changed continuously when changing $\vec{x}$. However, the visible cut (the so-called branch cut) that starts in the branch point has introduced a discontinuity — or, if one chooses another sign of the index of refraction when crossing the cut, a violation of the boundary condititions.

We have now found why branch points prevent our algorithms from succeeding. However, the physical interpretation of a branch point lying in the upper half of the frequency plane is not yet clear. As pointed out in [44], singularities and odd-order zeros of n^2 with positive imaginary part which, in fact, are branch points of $\sqrt{n^2}$ imply absolute instabilities of the medium. An absolute instability is a point in space

at which the electromagnetic fields grow infinitely large due to gain. Naturally, this can only occur in active media, since passive media never exhibit gain. Also, since we only examine our system in linear order of the probe field, saturation effects cannot occur.

This motivates a way proposed in [43] to deal with the critical branch points theoretically. For active systems, we can have

$$\left\|\vec{E}(\vec{r},t)\right\| \to \infty \text{ for } t \to \infty \,, \tag{4.14}$$

$\vec{E}(\vec{r},t)$ being the electric probe field component. Therefore, the Fourier transform

$$\tilde{E}(\vec{r},\omega) = \int_{-\infty}^{\infty} \vec{E}(\vec{r},\tau) e^{i\omega\tau} d\tau \tag{4.15}$$

of $\vec{E}(\vec{r},t)$ is not finite. For a better readability, we left out the vector arrow for the Fourier transformed electric field here. Since the Fourier transform diverges, we cannot use it in the derivation of the electric (and also the magnetic) susceptibility anymore. Usually, the Fourier transform comes into play when we rewrite the polarization

$$\vec{P}(\vec{r},t) \propto \int_{-\infty}^{\infty} \chi_e(\tau)\, \vec{E}(\vec{r},t-\tau)\, d\tau \tag{4.16}$$

as

$$\vec{P}(\vec{r},t) \propto \int_{-\infty}^{\infty} \tilde{\chi}_e(\omega)\, \tilde{E}(\vec{r},\omega) e^{-i\omega t}\, d\omega \tag{4.17}$$

in terms of the Fourier transformed electric susceptibility $\tilde{\chi}_e$ and the Fourier transformed electric field $\tilde{E}(\vec{r},\omega)$. In our derivation in Sec. 3, one can find this step from Eq. (3.9) to Eq. (3.12) for the particular case of a monochromatic probe field.

The fact that the Fourier transform diverges due to the diverging electric field in time domain motivates the transition to Laplace transforms instead of Fourier transforms. The Laplace transformed electric field $\hat{E}(\vec{r},\omega)$ is defined as

$$\hat{E}(\vec{r},\omega) = \int_{0}^{\infty} \vec{E}(\vec{r},\tau) e^{i\omega\tau} d\tau \,, \tag{4.18}$$

where $\omega \in \mathbb{C}$. Note that we left out the vector arrow of the Laplace transformed electric field for the sake of a better readability. Now, a negative imaginary part of

ω damps the diverging electric field for $t \to \infty$, if $\mathrm{Im}(\omega)$ is large enough. In other words, there is a $\sigma \in \mathbb{R}$ such that for every $\mathrm{Im}(\omega) < \sigma$ $\hat{E}(\vec{r}, \omega)$ is finite.

Note that if the Fourier transform does not diverge, σ can be chosen to be zero. Then, along the real axis, i.e. for $\mathrm{Im}(\omega) = 0$, Fourier and Laplace transform coincide. One only has to assume that the electric field at point $\vec{r}$ vanishes for $t < 0$ (compare Eqs. (4.18) and (4.18)). This assumption is easy to fulfill, as the time axis can be defined in such a way that the electric field has not reached point $\vec{r}$ at times $t < 0$.

Therefore, Fourier and Laplace transform are closely connected. An explicit evaluation shows that as a consequence Eq. (4.17) does not change its form when going from Laplace to Fourier transforms. Only the tildes change into hats in Eq. (4.17) and thus we have to work with Laplace transformed susceptibilities now. Therefore, we can calculate the index of refraction as usual according to Eqs. (4.1) and (4.3).

According to Skaar, it has several consequences that Eq. (4.3) now is to be understood in Laplace and not in Fourier space anymore. To transform the index of refraction in this equation back to time space, one has to apply the inverse Laplace transform, which is defined as

$$n(t) = \frac{1}{2\pi} \int_{i\sigma-\infty}^{i\sigma+\infty} e^{-i\omega t} \hat{n}(\omega) d\omega \, . \tag{4.19}$$

Note that $\hat{n}$ in this equation is the index of refraction appearing in Eq. (4.3) and not $n(t)$, since - as mentioned - Eq. (4.3) holds in Fourier and Laplace space, respectively. Also, the notation we used in Eq. (4.19) denotes an integration over a path that is given by a line parallel to the real ω-axis at a distance σ in the upper half of the complex plane (see path C_1 in Fig. 4.8). σ has to be chosen in such a way that there is no branch point or singularity ω_0 with $\mathrm{Im}(\omega_0) > \sigma$. Graphically speaking, the integration path in Eq. (4.19) has to be chosen such that all branch points or singularities lie "below" it. Again, one can see that for no branch points in the upper half, σ can be chosen to be zero. Then, the integration path coincides with the real axis and our Laplace transform has reduced to a Fourier transform.

However, this is only the case if there are no branch points and singularities in the upper half of the complex plane. Still, also in the case of a branch point (or singularity) ω_0 in the upper half plane, one can shift the integration path C_1 partially to the real axis as shown in Fig. 4.8. According to the residue theorem, we can move the original integration path C_1 as depicted by the arrows. However, since the function is not analytical in the branch point ω_0, we cannot use the residue theorem to move the integration path across the branch point without changing the value of the integral. Therefore, we obtain the new integration path C_2.

In this context, it becomes clear why there are problems if one restricts oneself to

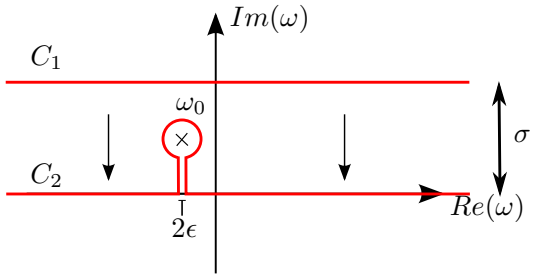

Figure 4.8: Due to the residue theorem, the original integration path can be moved from C_1 to C_2, such that parts of it coincide with the real axis. However, we cannot move the integration path across the branch point ω_0, since the function $n(\omega)$ that is integrated is not analytical in ω_0.

the real axis and thus to Fourier transforms. The path integral in Eq. (4.19) along C_2 can be decomposed into three parts: one part from $\omega = -\infty$ along the real axis to $\omega = Re(\omega_0) - \epsilon$ (labelled I_1), a second part leading from there around ω_0 back to the real axis (I_2) and a third part along the real axis from $\omega = Re(\omega_0) + \epsilon$ to $\omega = \infty$ (I_3). With the above explanation of the chosen integration path, we write Eq. (4.19) as

$$n(t) = \frac{1}{2\pi}\Big(\underbrace{\int_{-\infty}^{Re(\omega_0)-\epsilon} e^{-i\omega t}\hat{n}(\omega)d\omega}_{I_1} + \underbrace{\int_{\cap} e^{-i\omega t}\hat{n}(\omega)d\omega}_{I_2} + \underbrace{\int_{Re(\omega_0)+\epsilon}^{\infty} e^{-i\omega t}\hat{n}(\omega)d\omega}_{I_3}\Big)\,. \quad (4.20)$$

For $\epsilon \to 0$ it is now evident that part I_2 is not accounted for when working with Fourier transforms. Therefore, we obtain discontinuities of $n(\omega)$ on the real axis. These are the discontinuities we encountered when using the algorithm based on continuity in $\vec{x}$-direction.

Although with Laplace transforms we now have an appropriate tool to handle the cases of instabilities, i.e. branch points or singularities with positive imaginary part, mathematically, the physical interpretation is still difficult. If there are instabilities, the electromagnetic fields in time-domain are only valid until the linear response model is valid. This means that if the fields reach the threshold for gain saturation, the linear model fails. It is important to note that then, there is no physical interpretation for the index of refraction in the (Laplace-)transformed domain anymore.

For these reasons, we will avoid the cases of branch points in the upper half of the complex frequency plane and therefore we will restrict ourselves to the domain of parameters for which our medium is stable. Thus, we can still work with the Fourier

transform and the index of refraction has a physical meaning.

Since the only branch point of the complex root is zero, i.e. $0+i\cdot 0$, Eq. (4.2) shows that the branch points of n can be divided into branch points caused by a vanishing permittivity ε_r and into branch points caused by the permeability μ_r being zero. It is very helpful to note that if one of the two systems of our two-component medium is a two-level system, the permeability/permittivity of this system does not contain any branch points with positive imaginary part in frequency space. This can be seen at the coherence in a two-level system, which is given by

$$\tilde{\varrho}_{21} = \Omega_{21} \frac{2i\left(\tilde{\varrho}_{11}^{(0)} - \tilde{\varrho}_{22}^{(0)}\right)}{r+\gamma+2i\Delta} \tag{4.21}$$

in terms of the populations in zeroth order of the probe field Rabi frequency

$$\tilde{\varrho}_{11}^{(0)} = \frac{\gamma}{r+\gamma}\,, \tag{4.22}$$

$$\tilde{\varrho}_{22}^{(0)} = \frac{r}{r+\gamma}\,. \tag{4.23}$$

Here, $|2\rangle$ is the excited state, $|1\rangle$ the ground state, r the incoherent pump rate $|1\rangle \rightarrow |2\rangle$, γ the decay rate and Ω_{21} the probe field Rabi frequency. Note that the imaginary part of the magnetic susceptibility is the same as the imaginary part of the permeability (see Eq. (4.1)). Therefore, let us consider the magnetic susceptibility. According to Eq. (2.18), it is proportional to the coherence of Eq. (4.21) with a frequency-independent proportionality factor. The same holds for the electric susceptibility.

An explicit calculation shows that the imaginary parts of the only root ω_r and the only singularity ω_s of μ_r are given by

$$Im(\omega_r) = Im(\omega_s) = \frac{1}{2}(\gamma + r) \tag{4.24}$$

and therefore never negative, since $\gamma, r > 0$. The same holds for the permittivity ε_r of a two-level system with an electric dipole transition.

4.2 Results

Finally, we are in the position to calculate the index of refraction for different combinations of two species of atoms. For that, we can use the magnetically coupling

systems we examined in Secs. 2 and 3.6 and their optimized susceptibilities. In that section, we optimized the susceptibilities towards small imaginary part and negative real part.

For the electrically coupling species, we use a two-level system. The magnetically coupling system will be a two-level system as well, first. In this combination of two two-level systems, negative refraction can occur, as we will see, but only for a particular frequency difference between the frequencies of the magnetic and the electric probe transition. After that, we take an upper microwave system as magnetically coupling component. There, we find negative refraction at zero absorption, although the system turns out to be instable for the optimized parameters of Sec. 2. Lastly, we consider a closed-loop system with a magnetic probe transition. This will also emerge as suitable system for negative refraction, since it shows zero absorption at a negative real part of the refractive index.

We did not mention yet that, in principle, one should also take into account the difference between local and external fields. On the one hand, the electromagnetic fields in Eq. (3.9) are external fields. On the other hand, the fields in the Hamiltonian, see, e.g., Eq. (2.21b), which are the fields that the atoms "feel" in the end, are local fields. Up to now, we considered them to be the same. The local fields that interact with the atoms are a superposition of the externally applied fields (Eq. (2.3) or Eq. (3.1), respectively) and internal fields. The internal fields, in turn, are created by polarization/magnetization effects of the other atoms. Altogether, the external electric field $\vec{E}$ in Eq. (3.9) for which the linear response is calculated can be connected to the local field $\vec{E}_{loc}$ that appears in the Hamiltonian of Eq. (2.21b) by the Lorentz-Lorenz relation [46]

$$\vec{E}_{loc} = \underbrace{\vec{E}}_{\text{external}} + \underbrace{(\frac{1}{3} + s)\frac{1}{\varepsilon_0}\vec{P}}_{\text{internal}} \tag{4.25}$$

and analogously in the magnetic case. Here, the internal contribution contains two terms. These are due to the Lorentz-Lorenz model in which one includes all neighboring particles in a sphere around the considered atom, while particles outside the sphere are taken account of in a macroscopic treatment. The $s/\varepsilon_0\vec{P}$-term describes the near field of the neighboring particles within the sphere. Here, s is a constant that has to be chosen in dependence of the structure and symmetry of the given medium. For cubic symmetry and in the case of an isotropic medium, this constant vanishes and therefore the field of the neighboring atoms cancels. The other term $\vec{P}/(3\varepsilon_0)$ takes into account the field caused by the polarization of the particles outside the sphere.

Eq. (4.25) be employed to correct for local fields in - at least - two ways: We can apply a so-called local-field correction (LFC) in which Eq. (3.9) is written in terms

of local fields and then the local fields are replaced with the help of Eq. (4.25). Also, we can already replace the local fields in the Hamiltonian which leads to non-linear Bloch equations (NOBE). For an application of these methods and a more detailed description, see [18].

These corrections become important in dense gases which can be defined as gases that contain more than one particle in a cubic wavelength, i.e.

$$N\lambda^3 \gg 1\,. \tag{4.26}$$

In our case, the wavelength is optical and either $\lambda = 520.1705\,\mathrm{nm}$ or $\lambda = 600\,\mathrm{nm}$. The latter wavelength implies a particle density of $N \gg 5 \cdot 10^{18}\,m^{-3}$ at which the gas has to be considered as being dense.

We do not go into detail further, since we do not apply any local field corrections here. This has several reasons: First, we focused on the general principle of a two-component medium and the implications for negative refraction. Second, as found in [18], LFCs are not sufficient, but the use of NOBE prevents an easy interpretation.

4.2.1 A pair of two-level systems

The simplest combination of two level schemes is to take a two-level system for both species. Since the two-level system is not a complex system and does not contain many parameters, it should be easier to find a suitable two-level system for an experimental realization than a system with a larger number of levels. Also, as explained in Sec. 4.1.4, two-level systems do not exhibit any branch points and instabilities, respectively. Moreover, the typical Lorentzian susceptibility of a two-level system shown in Fig. 2.4 also has frequency ranges for which the real part of the index of refraction is negative.

Here, we chose the following parameters: $\gamma_e = \alpha^{-2}\gamma$ and $\gamma_m = \gamma$ are the decay rates of the electric and the magnetic probe transition, respectively. We also need the wavelengths of both probe transitions λ_e and λ_m to calculate the magnetic and the electric dipole moment according to Eqs. (2.43) and (2.34). Since the detunings of the electric and magnetic probe field component with respect to the corresponding transitions are related via Eq. (4.12), the wavelengths of both transitions are coupled via

$$\lambda_m = 2\pi c\,\frac{\lambda_e}{\Delta_m - \Delta_e + 2\pi c/\lambda_e}\,. \tag{4.27}$$

Up to now, we expressed Δ_m and Δ_e in units of γ. Therefore, in principle, we also have to express λ_e and λ_m in terms of γ. Since we want to choose optical

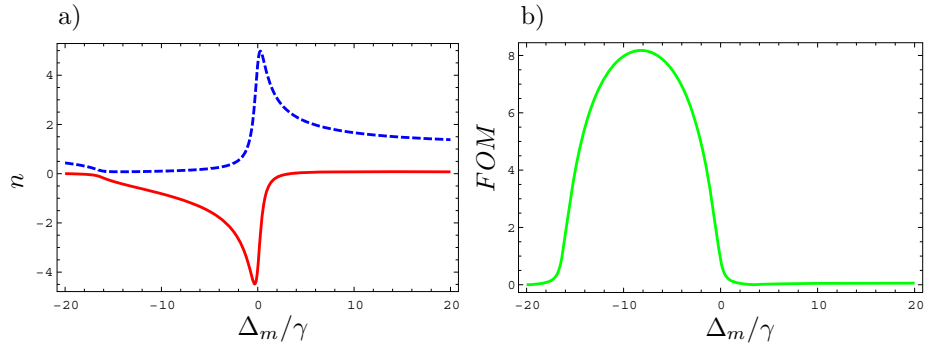

Figure 4.9: *(Pair of two-level systems)* In a), we show the real (red, continuous) and the imaginary part (blue, dashed) of the index of refraction for a composite system of two species of atoms that can both be described by a two-level system. In b), we plotted the corresponding figure of merit which we defined as FOM = $|Re(n)/Im(n)|$.

wavelengths, we now have to fix γ to a typical value. However, $2\pi c/\lambda_e \approx 3 \cdot 10^{15}\, s^{-1}$ for $\lambda_e = 600\,\text{nm}$. Also, $\Delta_m - \Delta_e$ is typically on the order of the natural linewidth of the electric transition (MHz). Therefore, it can be neglected and $\lambda_e \approx \lambda_m$ can be assumed when calculating the magnetic and the electric transition dipole moment. We chose $\lambda_e = \lambda_m = 600\,\text{nm}$. Of course, a much bigger $\Delta_m - \Delta_e$ could be possible in an experimental realization, since two atomic species with transition frequencies that lie closer might be unavailable. Then, of course, one has to use the full Eq. (4.27) and plug in the experimental parameters.

Moreover, the particle densities of the two components are chosen as $N_e = N_m = 10^{21}\,\text{m}^{-3}$. To optimize the results with respect to their figure of merit FOM = $|\text{Re}(n)/\text{Im}(n)|$, we set $r_e = x_1\gamma$, $r_m = x_2\gamma$ and $\Delta_m - \Delta_e = x_3\gamma$. We then vary x_1, x_2 and x_3 within the limits $0 < x_1 < 50\,\alpha^{-2}$, $0 < x_2 < 50$ and $-20\,\alpha^{-2} < x_3 < 20\,\alpha^{-2}$ with increment $dx_1 = \alpha^{-2}$, $dx_2 = 1$ and $dx_3 = \alpha^{-2}$. To find good figures of merit, we searched the ranges of the index of refraction with negative real part in steps of 1 in detuning direction.

We obtained the best figures of merit at points of negative real part for $x_1 = x_2 = 0$ and $x_3 = 8\alpha^{-2}$. The index of refraction for these parameters is shown in Fig. 4.9. Note that $x_1 = x_2 = 0$ implies a passive system. At $\Delta_m \approx -8.21\gamma$, we obtain FOM ≈ 8.17 and $n = -1.02 + i \cdot 0.12$. In experiment, the highest figures of merit nowadays are FOM ≈ 3 [47]. Therefore, our results are comparably good.

Here, negative refraction occurs in a range $-19.8\gamma < \Delta_m < 3.4\gamma$, while the figure of merit is larger than one in a range $-16.3\gamma < \Delta_m < -0.1\gamma$. In this range, the imaginary part of the refractive index is quite constant. Therefore, all frequency components of a pulse with a bandwidth in frequency space smaller than roughly

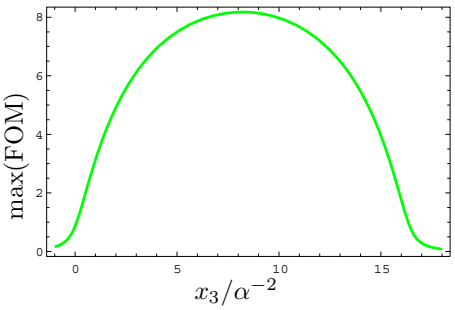

Figure 4.10: *(Pair of two-level systems)* We plot the maximum figure of merit in the negatively refracting frequency range over the shift between the two probe transitions $x_3/\alpha^{-2} = (\Delta_m - \Delta_e)/(\gamma\alpha^{-2})$.

16γ travelling through the medium would experience the same absorption. Also, the index of refraction reaches a real part of -1 at $\Delta_m = -8.4\gamma$. Therefore, the perfect lens proposed by Pendry could be realized in our case.

A drawback of the presented scheme is the fact that one has to find two species of atoms in which the magnetic and the electric probe transition have a particular distance in frequency space, namely $\Delta_m - \Delta_e = 8\alpha^{-2}\gamma$. To find out, how restrictive this condition is, we change $\Delta_m - \Delta_e$ and search for the maximal FOM for each value of $\Delta_m - \Delta_e$. Since we are only interested in negative refraction, we search for this maximum only at detunings for which the real part of the refractive index is negative. Thus, we obtain Fig. 4.10 which shows the maximal FOM in dependence of parameter $x_3/\alpha^{-2} = (\Delta_m - \Delta_e)/(\alpha^{-2}\gamma)$. Our calculations showed that the negative refraction vanishes for approximately $x_3 > 19.7\alpha^{-2}$ or $x_3 < -3.3\alpha^{-2}$.

One can see that for a range of approximately $0 < (\Delta_m - \Delta_e)/\gamma < 16\alpha^{-2}$, the maximum FOM is one or larger. Even for $\Delta_m - \Delta_e = 0$, one obtains negative refraction, however with at most FOM ≈ 0.9. Therefore, one does not strictly need to realize our optimized parameters. Indeed, it is possible to deviate from the optimal difference of magnetic and electric probe transition frequency by 16 times the natural linewidth of a typical electric transition.

4.2.2 Upper microwave system, two-level system

In Sec. 2.3.1, we examined the upper microwave system thoroughly and optimized its magnetic susceptibility towards a negative real and a small imaginary part for a particular detuning. Thus, let us now consider a configuration in which an upper microwave system couples to the magnetic probe field component and a two-level system couples to the electric probe field component. First, we assume the upper

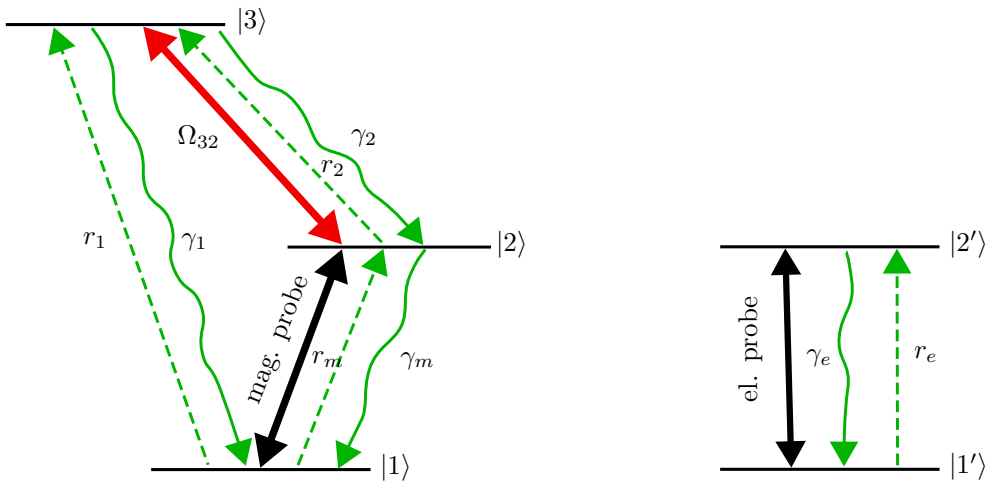

Figure 4.11: First, we take a magnetically coupling upper microwave system and an electrically coupling two-level system. The notation of the parameters we use is illustrated in the figure above.

microwave system to consist of three magnetic transitions as in Sec. 2.3.1. In the next subsection, we will consider the nitrogen parameters.

We label all quantities referring to the electric probe transition in the two-level system with a subindex e. In the upper microwave system, we adopt the notation of Sec. 2.3.1. However, the magnetic probe transition will be labelled with the subindex m. For illustration purposes, we show this notation in Fig. 4.11.

Magnetic transitions

In the case of three magnetic dipole transitions, we use the typical parameters of Sec. 2.3.1 — $\gamma_1 = \gamma$, $\gamma_2 = \gamma$, $\gamma_m = \gamma$ — and for the two-level system $\gamma_e = \alpha^{-2}\gamma$. Also, we assumed probe transition wavelengths of $\lambda_e = \lambda_m = 600\,\mathrm{nm}$ and particle densities of $N_e = 10^{21}\mathrm{m}^{-3}$, $N_m = 10^{23}\mathrm{m}^{-3}$. If we set $r_e = r_1 = r_2 = 0$, $\Delta_2 = 0$, $r_m = x_1\gamma$ and $|\Omega_{32}| = x_2\gamma$, we reproduce the parameters of Fig. 2.6 a) for a choice of $x_1 = 2$, $x_2 = 5$.

These are also the parameters we used for demonstrating the problems of the branch points in Figs. 4.1, 4.3, 4.4, 4.5 and 4.6. Fig. 4.1 seems to be promising, since the physical solution for the index of refraction at $\vec{x} = \vec{x}_f = (x_1, x_2) = (2, 5)$ and a probe field detuning of $\Delta_m \approx -9\gamma$ has a vanishing imaginary part and a negative real part. However, we already pointed out that, for these parameters, one obtains branch points in the upper half of the complex frequency plane.

The parameter area for which we obtain critical branch points (see Sec. 4.1.4) is

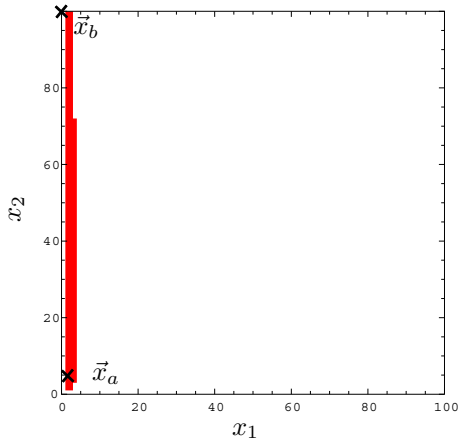

Figure 4.12: *(Upper microwave system with only magnetic transitions, two-level system)* For our two-component system that we used to demonstrate the problems of the branch points in Sec. 4.1.3, one can clearly see that $\vec{x}_a$ (which is $\vec{x}_f$ of Sec. 4.1.3) lies in the area of branch points with positive imaginary part. Optimizing the figure of merit yields best results in an area of negative refraction at $\vec{x}_b = (0, 100)$. At most, we reach FOM ≈ 1.1 there.

illustrated in Fig. 4.12 which has to be understood in the following way: Each point $\vec{x} = (x_1, x_2)$ of the plane corresponds to a different set of system parameters. In fact, as given before, the first coordinate x_1 is proportional to the strength of the incoherent pump rate on the magnetic probe transition, the second coordinate x_2 is proportional to the strength of the coherent control field. Therefore, $(x_1, x_2) = (0, 0)$ implies a passive system. Every point (x_1, x_2) that corresponds to a set of parameters which causes branch points with positive imaginary parts and thus instabilities is colored red. Since we tested for branch points with an increment of 1 in every coordinate direction, the figure has a resolution of 1 along each axis. Also, a singularity at ω_s with $\mathrm{Im}(\omega_s) > 0$ would pose the same problems as a branch point in the upper half plane. However, we did not encounter any singularities with the mentioned property for any value of $\vec{x}$ in the plane of Fig. 4.12. Therefore, there is no "red area" for the singularities.

Let us return to the parameters $(x_1, x_2) = (2, 5)$ which we marked with a black cross and labelled $\vec{x}_b$ in Fig. 4.12. One can see what we already pointed out in Sec. 4.1.3, in which we used these parameters to illustrate the branch points: $\vec{x}_b$ lies within the red area and the system is instable. Therefore, we cannot use the optimized susceptibility of Fig. 2.6 a).

Since we cannot use the optimized magnetic susceptibility, there is also no point in using systems with optimized electric susceptibilities, such as the ones in [20], instead of the two-level system. This does not move the critical branch points from

the upper half to the lower half of the frequency plane, as the branch points are caused by μ_r here and therefore by the magnetic upper microwave system. In fact, a two-level system seems to be a better choice, as it does not introduce further critical branch points and thus instabilities.

However, we can still vary x_1 and x_2 between 0 and 100, respectively, with a respective increment of 1 to find the best figure of merit at negative refraction. In this way, we find a figure of merit of FOM ≈ 1.1 at most. This is the case at $(x_1, x_2) = (0, 100) = \vec{x}_b$ at a detuning of $\Delta_\alpha \approx -1578\gamma$.

We also find that negative refraction with FOM > 1 can only be realized for parameter sets with $x_1 = 0$ in this scheme. For $x_1 = 0$ and $0 < x_2 < 100$, we obtain figures of merit slightly bigger than 1 which grow when $x_2 \to 100$. As we will see in the following subsection, this behavior can also be found when we choose other system parameters.

Nitrogen

Parameter set 1 - For the parameters $\gamma_m = \gamma$, $\gamma_1 = 3.92\gamma$, $\gamma_2 = 1.86 \cdot 10^{-3}\gamma$ and $\lambda_m = 520.1705$ nm in the upper microwave configuration of the magnetically coupling system, we obtain a nitrogen-like system [27] as in Sec. 2.3.1. For the two-level system coupling to the electric probe field component, we still have $r_e = 0$, $\gamma_e = \alpha^{-2}\gamma$ and, this time, $N_e = 10^{21}\,\mathrm{m}^{-3}$. Also, in the upper microwave system, we set $N_m = 10^{23}\mathrm{m}^{-3}$, $r_2 = r_1 = 0$, $r_m = x_1\gamma$, $\Delta_2 = 0$ and $|\Omega_{32}| = x_2\gamma$. This is identical to the choice of pump rates and coherent field strengths in the last subsection and reproduces the optimized susceptibility in Fig. 2.7 a) for $(x_1, x_2) = (5, 10)$.

We plot a figure of the same kind as in the last section whose axes are, again, given by x_1 and x_2 (Fig. 4.13). The values of $\vec{x} = (x_1, x_2)$, for which there are branch points in the upper half of the frequency plane and thus instabilities, are colored red — once more with a resolution of 1 in each direction. Again, we do not encounter any singularities in the upper half of the frequency plane.

The parameters $(x_1, x_2) = (5, 10)$ that reproduce our optimized susceptibility — labelled $\vec{x}_c$ — unfortunately lie in this colored, instable area (see Fig. 4.13).

As in the last subsection, we therefore look for the best FOM at detunings for which negative refraction occurs in dependence of (x_1, x_2). We also search in the same range $(0 < x_1, x_2 < 0)$ and with the same increment ($dx_1 = 1$, $dx_2 = 1$) as before. Again, we find the best results for $(x_1, x_2) = (0, 100)$ which we labelled $\vec{x}_d$ in Fig. 4.13. There, for a detuning of $\Delta_m \approx -1000\gamma$, we find values of FOM ≈ 1.05.

Also, we found that negative refraction with FOM > 1 occurs in this system for arbitrary values of x_2 — within the range $0 < x_2 < 100$ we considered — but only small values of x_1, more precisely $x_1 < 3$. This is a similar behavior to the one we

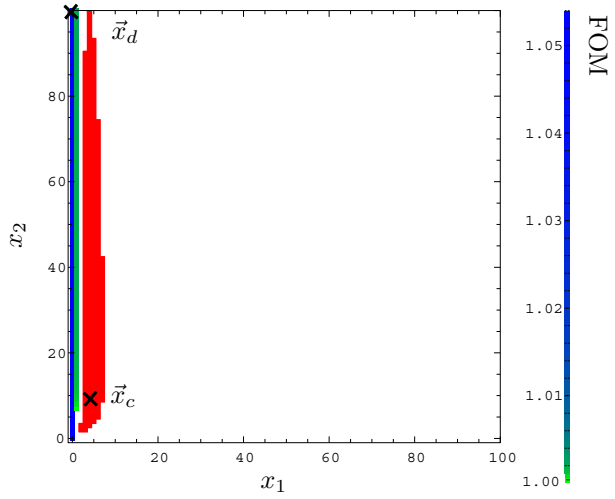

Figure 4.13: *(Upper microwave system with nitrogen parameters, two-level system)* The plane of values for (the two-dimensional) $\vec{x}$ shows areas in which we obtain branch points (red). The optimized magnetic susceptibilities of Fig. 2.7 a) through d) lie in this area (black cross labelled with $\vec{x}_c$). In blue/green, we mark parameter points at which negative refraction with a FOM > 1 is possible. The shade of green/blue at point (x_1, x_2) gives the maximum FOM in an area of negative refraction that one encounters when calculating the FOM at different detunings in steps of $d\Delta_m = \gamma$. Which shade of blue/green corresponds to which FOM is given by the scale to the right of the figure.

found in the last subsection. To illustrate the parameter ranges at which one finds negative refraction with FOM > 1, we did not only color the forbidden points red in Fig. 4.13. Here, we also colored points (x_1, x_2) without critical branch points in shades going from green to blue according to the scale next to the figure. This color gives the maximum FOM (at negative refraction) that one can find at any detuning for the parameters given by (x_1, x_2). We do not consider figures of merit smaller than 1. This illustrates the parameter range in which to find negative refraction. As mentioned, it is striking that this area is given by small values of x_1.

Let us therefore have a closer look at the refractive index in detuning space for the parameters $\vec{x}_c = (0, 100)$ (see Fig. 4.14) . Between $\Delta_m \approx -1079\gamma$ and $\Delta_m \approx -100\gamma$, the system refracts negatively and the imaginary part has about the same absolute value as the real part which results in FOM ≈ 1. In the complex plane, we have branch points at the detunings $\delta_0/\gamma \approx -1079 + 0.5i$ and $\delta_1/\gamma \approx 9 + 2i$ (not shown here). Note that none of the branch points lies in the upper half of the complex *frequency* plane, since frequency and detuning are connected via a minus sign according to Eq. (4.13).

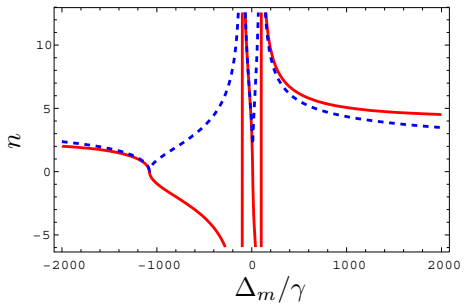

Figure 4.14: *(Upper microwave system with nitrogen parameters, two-level system)* The plane of values for (the two-dimensional) We show real (red, continuous) and imaginary (blue, dashed) part of the refractive index at $x_1 = 0$, $x_2 = 100$. At $\Delta_m \approx -1079\gamma$ and $\Delta_m \approx 9\gamma$, the real part becomes zero.

At the roots of the real part of the index of refraction, namely at $\Delta_m \approx -1079\gamma$ and $\Delta_m \approx 9\gamma$, the refractive index does not seem to be smooth. However, if one zooms in onto these points, one can see that the refractive index is differentiable. The similarity of the refractive index at these points and in Fig. 4.4 a) and the proximity of the branch points to these seemingly non-smooth points on the real detuning axis allows for the following conclusion: The shape of the index of refraction at these points is caused by the close branch points. Moving the branch points closer to the real axis would cause a steeper slope of the real part and, when the branch point crosses the real axis, a discontinuity.

This motivates the conjecture that it is easier to find negative refraction close to parameters which yield branch points with positive imaginary part (in the frequency plane) and therefore instabilities. This assumption can be justified heuristically by the following fact: The real part of the complex root function and its analytical continuation has a sign change in the proximity of the branch point. If one chooses the branch cut as in Fig. 4.7, this sign change occurs at the branch cut. Since the index of refraction is also calculated via a complex root function, this means that we are quite likely to encounter negative refraction there. The following results support this rule of thumb.

Parameter set 2 - Having found a similar behavior of the upper microwave system with only magnetic transitions and the nitrogen-like system, we now investigate the nitrogen-like configuration for the parameters of the optimized susceptibility in Fig. 2.7 e). These are $r_1 = x_1\gamma$, $r_2 = r_m = 0$, $\Delta_2 = x_2\gamma$, $|\Omega_{32}| = x_2\gamma$. With these parameters, we obtain the optimized susceptibility of Fig. 2.7 e) for $x_1 = 6$, $x_2 = 10$. Also, we choose particle densities of $N_e = 10^{21}$ m^{-3} and $N_m = 10^{23}$ m^{-3}.

However, for $x_1 = 6$, $x_2 = 10$, we obtain branch points of the index of refraction in the upper half of the complex frequency plane. This can be seen by Fig. 4.15 in

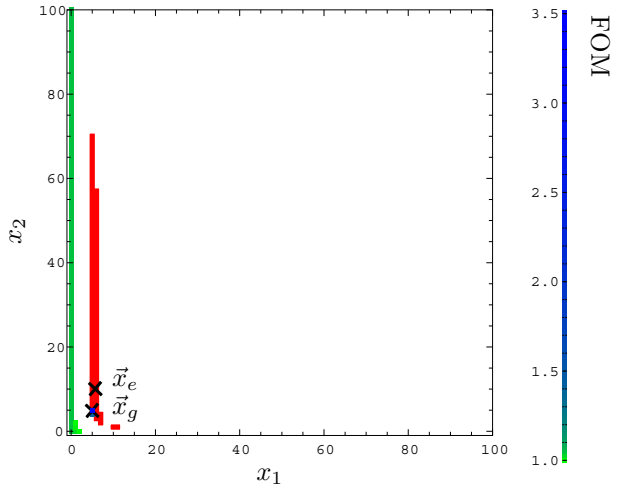

Figure 4.15: *(Upper microwave system with nitrogen parameters, two-level system)* The plane of values for (the two-dimensional) $\vec{x}$ shows areas in which we obtain branch points (red). Unfortunately, the optimized magnetic susceptibility of Fig. 2.7 e) lies in it (black cross labelled with $\vec{x}_e$). The best value we obtain for another parameter set is plotted in Fig. 4.16 and labelled $\vec{x}_g = (x_1, x_2) = (5, 5)$.

which we marked $\vec{x}_e = (6, 10)$ by a black cross. Singularities do not appear in the upper half of the frequency plane.

Still, we can vary x_1 and x_2 in the white area of Fig. 4.15 to find a suitable figure of merit and negative refraction. The search for good results in the range of $0 < x_1, x_2 < 100$ with an increment of $dx_1 = dx_2 = 1$, avoiding the area of critical branch points, yields FOM ≈ 3.5 for $x_1 = x_2 = 5$. In Fig. 4.15, this point has been labelled $\vec{x}_g$. Strikingly, $\vec{x}_g$ lies close to the instable, red area. If we assume that a small change in x_1 and x_2 changes the position of the branch points in the frequency plane only slightly, one can conclude that for $\vec{x} = \vec{x}_g$, there is a branch point close to the real frequency/detuning axis in the complex plane. This is what we formulated as a rule of thumb before.

The refractive index for these parameters can be seen in Fig. 4.16 a), while b) shows the figure of merit. A figure of merit of 3.5 is good when compared to current experiments in metamaterials [47]. Note that the figure of merit reaches the value at a narrow peak, a fact that favors pulses with a small frequency bandwidth.

The position of $\vec{x}_g$ in Fig. 4.15 and the fact that a close branch point in the frequency plane seems to yield good results motivates the following method to increase the FOM. Since our algorithm worked with an increment of $dx_1 = dx_2 = 1$, it is possible that we obtain higher FOMs when we change, e.g., x_1 to approach the red parameter area of critical branch points in steps smaller than one. Let us denote by ξ_1 the

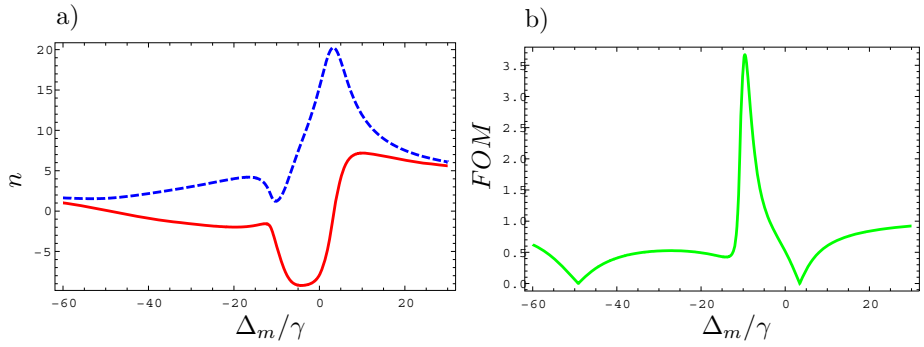

Figure 4.16: *(Upper microwave system with nitrogen parameters, two-level system)* a) The plot shows the real (red, continuous) and the imaginary (blue, dashed) part of the index of refraction at $x_1 = x_2 = 5$ in the combined system of upper microwave and two-level system. b) The figure of merit (FOM), defined as FOM = $|\mathrm{Re}(n)/\mathrm{Im}(n)|$, reaches approximately a value of 4.

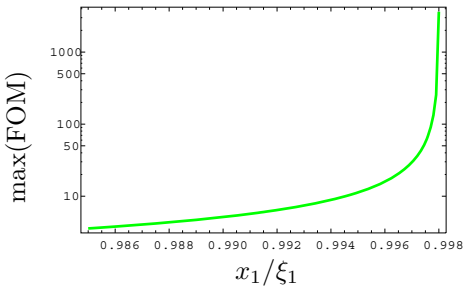

Figure 4.17: *(Upper microwave system with nitrogen parameters, two-level system)* We approach the parameter area of instabilities by changing x_1 — while $x_2 = 5$ — and calculate the highest FOM that we obtain at negative refraction (see axis of ordinates).

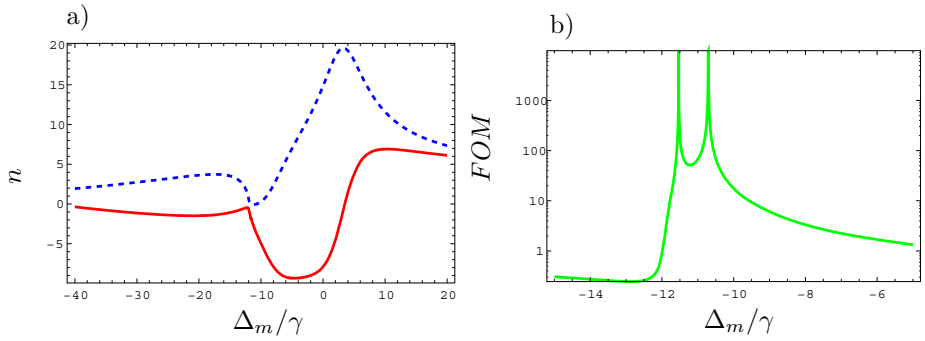

Figure 4.18: *(Upper microwave system with nitrogen parameters, two-level system)* a) We plotted the real (red, continuous) and the imaginary (blue, dashed) part of the index of refraction at $x_2 = 5$, $x_1 = 0.9985\,\xi_1$. b) The FOM diverges due to the vanishing absorption at two points. Note the logarithmic scale of the FOM-axis.

smallest value for which the parameters $\vec{x} = (x_1, x_2) = (\xi_1, 5)$ cause a branch point in the upper half of the frequency plane. Graphically speaking, this is the x_1-coordinate at which we cross the border to the red area in Fig. 4.15 when increasing x_1 from $(5, 5)$ (and it has an approximate value of $\xi_1 \approx 5.074$).

When we change x_1 from 5 to ξ_1 and calculate the highest FOM that occurs in a detuning range of negative refraction, we obtain Fig. 4.17. For approximately $x_1/\xi_1 = 0.9985$, the imaginary part of the refractive index becomes zero at $\Delta_m \approx -10.5\gamma$ and $\Delta_m \approx -11.5\gamma$, while the real part reaches $n = -3.7$ and $n = -2.0$ as one can see in Fig. 4.18 a). Then, the FOM diverges (see Fig. 4.18 b)). This means vanishing absorption at negative refraction. The branch point that crosses the real detuning/frequency-axis for ξ_1 lies directly below $\Delta_m \approx -10.5\gamma$ in the complex frequency plane.

Since the FOM-axis in Fig. 4.18 b) is logarithmic, the FOM increases quickly with x_1. If we prepare the presented system in an experiment with the given parameters and then increase x_1, i.e. the incoherent pump rate r_1, from $x_1 = 5$, the absorption at $\Delta_m \approx -10.5\gamma$ and $\Delta_m \approx -11.5\gamma$ decreases. Therefore, we are able to realize negative refraction at low losses. In an experiment, one would have to fix x_1 and therefore r_1 with a high precision, since $x_1 > \xi_1$ would cause the medium to be instable. This makes an experimental realization more difficult.

One can see in Fig. 4.18 a) that at the point of vanishing absorption, the real part is also close to zero. The next system that we present behaves similar as the one we considered in this section. However, at zero absorption, the real part of the refractive index will not be as close to zero as the one in Fig. 4.18 a) and therefore the parameter range in which instabilities occur is not as close.

4.2.3 Closed-loop system, two-level system

Finally, let us consider a two-component system made up of a magnetically coupling species of atoms in a closed-loop configuration and an electrically coupling species with a two-level energy level scheme. As can be seen by Fig. 3.9, the magnetic susceptibility of the closed-loop scheme shows a rich structure.

Again, we label all quantities referring to the electric probe transition in the two-level system with a subindex e. In the closed-loop system, we adopt the notation of Sec. 3 (see Fig. 3.1 a)). As before, the magnetic probe transition will be labelled with the subindex m.

We consider a nitrogen-like closed-loop system. Therefore, we have the parameters $\gamma_m = \gamma$, $\gamma_1 = 3.92\gamma$, $\gamma_2 = 1.86 \cdot 10^{-3}\gamma$, $r_1 = r_2 = r_m = 0$, $\lambda_m = 520.1705\,\mathrm{nm}$, $\Delta_1 = 0$, $|\Omega_{31}| = x_1\gamma$, $N_m = 10^{23}\mathrm{m}^{-3}$, $\Delta_2 = -24\gamma$, $|\Omega_{32}| = x_2\gamma$ and $\gamma_e = \alpha^{-2}\gamma$, $\lambda_e = 520.1705\,\mathrm{nm}$, $N_e = 1.5 \cdot 10^{20}\mathrm{m}^{-3}$ for the electrically coupling system.

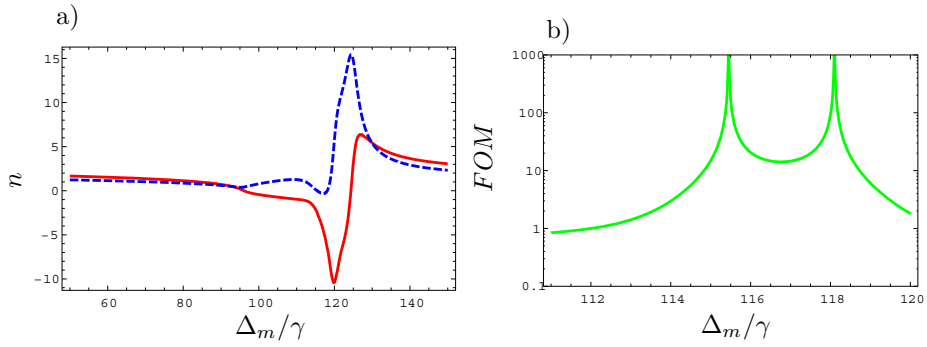

Figure 4.19: *(Closed-loop system with nitrogen parameters, two-level system)* The index of refraction (see a)) of a closed-loop system coupling electrically and a two-level system coupling magnetically has a vanishing imaginary part (blue, dashed) at $\Delta_m \approx 115\gamma$ and $\Delta_m \approx 118\gamma$ for the parameters given in the text. At these points, we also have a negative real part (red, continuous). Therefore, the FOM in b) diverges at two points. Note the logarithmic scale of the FOM-axis in b).

The optimized susceptibility of Sec. 3.6 — see Fig. 3.9 c) for the nitrogen parameters — corresponds to $(x_1, x_2) = (37, 18)$ which we call $\vec{x}_h$ in Fig. 4.20. In the same way as we have done it for the system in the last subsections, this figure shows the forbidden parameter areas in red. It can be seen that the parameter set $\vec{x}_h$ causes critical branch points as it lies in such an area.

The shades of green/blue in Fig. 4.20 again give the maximum FOM at the corresponding parameter values for (x_1, x_2). The best FOM is obtained at $\vec{x} = \vec{x}_k = (x_1, x_2) = (62, 75)$. However, there, the FOM is not only FOM ≈ 70000, but at a certain detuning, it even diverges. Note that this is not unphysical, since it is

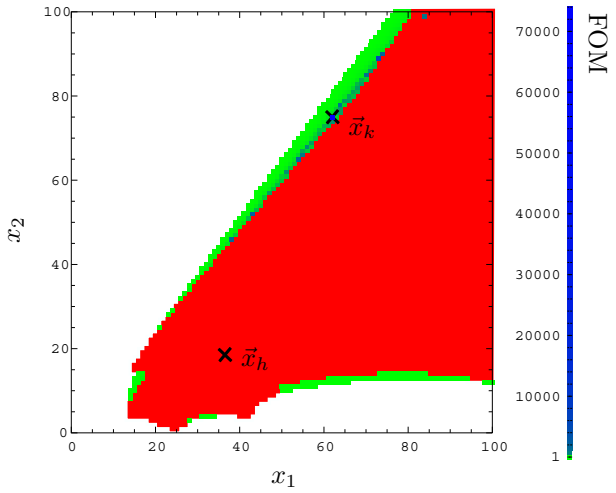

Figure 4.20: *(Closed-loop system with nitrogen parameters, two-level system)* x_1 and x_2 are connected to system parameters according to $|\Omega_{31}| = x_1\gamma$, $|\Omega_{32}| = x_2\gamma$ in the closed-loop system combined with a two-level system. For system parameters in the red area, the system has branch points in the upper half of the frequency plane and is instable.

simply caused by zero absorption at this detuning, i.e. a vanishing imaginary part of the refractive index which is the denominator of the FOM. The divergence is not reflected by the blue/green color scale of Fig. 4.20, since the maximum FOM that is indicated by green/red colors in this figure has been obtained by calculating the FOM for different detunings is steps of $d\Delta_m = 1$. With this stepwidth, one misses the point of divergence and only obtains FOM ≈ 70000 in its proximity. However, for illustration purposes, this stepwidth is sufficient. The fact that, again, the best results are obtained for parameters close to parameters that cause instabilities might deliver a rule of thumb at which parameters one has to look for high FOMs in other systems.

A look at the index of refraction in detuning space, as shown in Fig. 4.19 a), reveals that there are even two points of zero imaginary part. Fig. 4.19 b) shows the corresponding FOM. We also find that the real parts of the refractive index are $n = -6.4$ and $n = -2.5$ at the points of vanishing absorption. They are stronglier negative than the ones in Fig. 4.18 a). Therefore, the closed-loop system seems to be a better candidate than the upper microwave system. However, in the closed-loop system, we need two control fields. Therefore, the more suitable shape of the real part is at the expense of a more complicated experimental setup.

Shapes of the refractive index similar to the one in Fig. 4.19 a) can also be found for other parameters, namely the ones colored in darker blue in Fig. 4.20. Thus,

the combination of a magnetically coupling closed-loop system and an electrically coupling two-level system provides many possibilities for negative refraction at zero absorption.

Chapter 5

Conclusion

5.1 Summary

In this thesis, we found negative refraction with vanishing absorption in two-component media. The use of two-component media was motivated by the fact that suitable real atoms might be easier to find than for single-component approaches and that, in one of the two species, one can apply control fields such that they form a closed interaction loop with the probe transition. To achieve negative refraction, we first optimized the magnetic susceptibility of several different systems towards zero imaginary and negative real part, as motivated by Veselago [1] (Sec. 2) . For all presented systems, we succeeded in finding parameters that produce a negative real and zero imaginary part of the magnetic susceptibility. To this end, we used a strong control field to introduce a Rabi splitting in the susceptibility and incoherent pump rates to change the absorptive behavior of our system. In Sec. 4, we found that the optimized systems for the magnetic component exhibit branch points with positive imaginary part in the frequency plane and thus instabilities. Therefore, we optimized the combined systems to achieve the aforementioned results for the index of refraction.

To investigate a possible mechanism for an enhancement of the magnetic response by a factor of α^{-1}, we compared a closed-loop and a similar, but incoherently pumped system (Sec. 3). We found an enhancement in the first system and could clearly attribute it to the electric probe field component scattering into the magnetic probe transition. This result opens the road for a further enhancement of the response by increasing the involved expansion coefficient of the coherence. Also, the large number of parameters in the closed loop system motivated an optimization of a slightly changed version of this system and led to its use in the last section.

In the last section (Sec. 4), we tested several two-component configurations for

negative refraction at low absorption. We found that a negative real part of the index of refraction occurs in such rather simple systems as media made up of two different species that can each be described by a two-level scheme. For particle densities of $N_e = N_m = 10^{21}\,\mathrm{m}^{-3}$ for the two respective components, we achieve $FOM = |\mathrm{Re}(n)/\mathrm{Im}(n)| \approx 8$ for a particular value for the frequency shift between electric and magnetic probe transition. However, we are not confined to this particular value and reach reasonable figures of merit also for frequency shifts that are several spectral linewidths (of an electric dipole transition) larger or smaller.

Moreover, we obtained vanishing absorption and, at the same frequency, a negative real part of the refractive index in two different systems. The first system was a combination of a magnetically coupling nitrogen-like upper-microwave system and a two-level system. The second of these systems was given by a combination of a nitrogen-like closed-loop system for the magnetic response and, again, a two-level system for the electric response. To realize negative refraction, one needs, in the first system, particle densities of $N_e = 10^{21}\,\mathrm{m}^{-3}$ and $N_m = 10^{23}\,\mathrm{m}^{-3}$ for the electrically coupling species and the magnetically coupling species, respectively. We find $n = -3.7$ and $n = -2.0$ at two frequencies of vanishing absorption. In the second system, the closed-loop system, we require $N_e = 1.5 \cdot 10^{20}\,\mathrm{m}^{-3}$ and $N_m = 10^{23}\,\mathrm{m}^{-3}$ and find $n = -6.4$ and $n = -2.5$. The density of the magnetically coupling species are comparable to other proposals ($N \approx 10^{23}\,\mathrm{m}^{-3}$ in [18], $N \approx 5 \cdot 10^{22}\,\mathrm{m}^{-3}$, but with a finite FOM, in [17]). For the electrically coupling species, the density is rather small. In the combination of closed-loop and two-level system, we obtain a real part of the refractive index of a higher absolute value at the point of zero absorption than in the upper microwave system. First, this implies a stronger effect that one can measure. Second, the parameter range at which instabilities occur is not as close (see Sec. 4.2.2) and therefore the experimental parameters do not have to be fixed with such a high precision. Therefore, the closed-loop system seems to be slightly more suitable for an experiment.

Strikingly, the best results for the figure of merit were produced by parameters close to parameters that cause the system to be instable (see Figs. 4.13, 4.15 and 4.20).

5.2 Outlook

Having summarized the results of this thesis, there are still many questions that need to be addressed in order to realize negative refraction in atomic two-component — and also single-component — media and to gain a deeper understanding of the mechanisms involved.

We chose to optimize the magnetic susceptibility towards negative real and vanishing imaginary part, motivated by the findings of Veselago [1]. However, there are also

other ways in which the susceptibilities can be optimized (see Fig. 2.1) as it has been done in [18]. In our case, the optimized magnetic susceptibilities caused branch points in the upper half of the complex plane and thus instabilities. Therefore, we had to search for other parameters to achieve negative refraction with low losses. For susceptibilities optimized towards other values, this might not be the case.

Then, there is also the possibility to take better use of the mechanism of enhancement we investigated in Sec. 3. On one hand, a medium in a closed-loop configuration of strong control fields and only one probe field transition presumably induces a strong response on the probe transition. However, we have seen that the investigated scattering process only contributes to the response at the probe field frequency for the case of multiphoton resonance, i.e. for one single frequency. On the other hand, systems with two probe transitions as in Fig. 3.8 that render the enhancement process independent from the probe field frequency contain one more weak probe field in the interaction loop. This latter scheme has already been considered in [17, 18]. Still, it might be possible to find a configuration that combines the advantages of both possibilities: a strong response on the probe transition caused by a control field loop and frequency-independence of this mechanism. In any case, there still remain many new configurations — especially chiral systems — to be investigated.

Also, since the results for the index of refraction in the forbidden parameter area, in which the system is instable, seemed so promising, one can look for ways to deal with these instabilities. In theory, this can be done by Laplace transforms. Of course, physically instable systems are not suitable for an experimental realization. However, there might be ways to prevent the electromagnetic field from growing infinitely large such as saturation effects of higher than first order in the probe field that we did not consider. A further examination of these instabilities is desirable.

Finally, to realize schemes as the ones presented experimentally, one first needs suitable candidates. Also for the two-component system, it turned out that these are not easy to find, since many conditions have to be fulfilled: We need a magnetic and an electric dipole probe transition at approximately the same frequency — in two different species of atoms, respectively — a level scheme with optical transitions and not too many other levels to which the population in the used levels could decay to. For example, a level $|0\rangle$ below the levels of the upper microwave scheme in Fig. 2.3 would cause population of the levels $|1\rangle$, $|2\rangle$ and $|3\rangle$ to decay to it. Thus, our scheme would lose population. One could use repump lasers that pump the population to level $|3\rangle$ again. However, this would complicate the experimental setup and is only feasible for not too many levels of the kind of $|0\rangle$.

The most suitable element for the magnetically coupling upper microwave or closed-loop system we found is nitrogen, in which the first and the second excited state can decay to the ground state via optical transitions. For the electrically coupling two-level system, one can also take a two-level system with a slightly different transition

frequency and add a third level. Between the third and one of the two other levels a strong control field can then couple. This creates a Rabi splitting, i.e. an AC Stark shift, to change the transition frequency to coincide with the frequency of the magnetic probe transition.

Other suitable elements with a rather simple level structure, optical transitions and not too many other levels to which the population can decay are:

- Oxygen, with a ground state triplet to which the next-highest state can decay via M1- or E2-transitions. These transitions have wavelengths of 630.2 nm, 636.6 nm and 639.4 nm, the latter being only an E2-transition.

- Scandium, which could possibly be the electrically coupling counterpart to oxygen. It has electric dipole transitions from the $3d4s(^3\mathrm{D})4p\ ^4\mathrm{F}^\circ$- and $3d4s(^3\mathrm{D})4p\ ^4\mathrm{D}^\circ$-quadruplet to the upper state of the ground state dublet at wavelengths such as 630.6 nm and 636.2 nm .

- Magnesium, again for the magnetically coupling component, since it has optical M1-transitions from the third-lowest multiplet to the second-lowest multiplet. More precisely, these are transitions from the $3s3p\ ^1\mathrm{P}^\circ$-singulet, to the $3s3p\ ^3\mathrm{P}^\circ$-triplet states of 757.3 nm, 758.5 nm and 760.8 nm. Below this level, there is only the ground state to which the mentioned triplet and singulet states can decay electrically. Therefore, repumping should be employed.

- Carbon which is slightly beyond the edge of the visible spectrum would be a candidate with its M1-transitions from the $2s^2 2p^2\ ^1\mathrm{D}$-singulet to the ground state triplet, ranging from 980.8 nm to 958.0 nm.

- Also already slightly in the infrared, phosphorus has two M1-transitions from the $3s^2 3p^3\ ^2\mathrm{D}^\circ$-doublet states to the ground state at 878.8 nm and 880.0 nm.

The wavelengths were given in air according to [27].

Another point is the incorporation of local field corrections as described in Sec. 4.2 which should be taken into account for $N\lambda^3 \gg 1$, i.e. $N \gg 5 \cdot 10^{18}\ \mathrm{m}^{-3}$ for $\lambda = 600\ \mathrm{nm}$. Since this criterion is not hard, we might well be in the regime in which corrections are necessary. This is also implied by preliminary calculations of local-field corrected susceptibilities in which we only correct the field in the results (and not already in the Hamiltonian).

Besides negative refraction, materials with a permeability significantly different from unity, in particular gases, are an interesting field of research. This is especially due to the fact that usually, the magnetic response is small and thus the permeability approximately one.

Although or particularly since some effort is still needed to realize negative refraction in an atomic (two-component) gas for the first time, interesting new insights in this field are to be expected. Thereby, it is not only the counter-intuitive, new properties of negatively refracting materials, but also the wide range of possible applications that fuel the research in this direction.

Bibliography

[1] V. G. Veselago, Sov. Phys. Usp **10**, 509 (1968).

[2] R. A. Shelby, D. R. Smith, and S. Schultz, Science **292**, 77 (2001).

[3] D. R. Smith, W. J. Padilla, D. C. Vier, S. C. Nemat-Nasser, and S. Schultz, Phys. Rev. Lett. **84**, 4184 (2000).

[4] J. B. Pendry, A. J. Holden, D. J. Robbins, and W. J. Stewart, IEEE Trans. Microwave Theory Tech. **47**, 2075 (1999).

[5] E. Cubukcu, K. Aydin, E. Ozbay, S. Foteinopoulou, and C. M. Soukoulis, Nature **423**, 604 (2003).

[6] A. A. Houck, J. B. Brock, and I. L. Chuang, Phys. Rev. Lett. **90**, 137401 (2003).

[7] C. M. Soukoulis, S. Linden, and M. Wegener, Science **315**, 47 (2007).

[8] S. Zhang, W. Fan, N. C. Panoiu, K. J. Malloy, R. M. Osgood, and S. R. J. Brueck, Phys. Rev. Lett. **95**, 137404 (2005).

[9] A. Grbic and G. V. Eleftheriades, Phys. Rev. Lett. **92**, 117403 (2004).

[10] J. B. Pendry, Phys. Rev. Lett. **85**, 3966 (2000).

[11] J. B. Pendry, D. Schurig, and D. R. Smith, Science **312**, 1780 (2006).

[12] U. Leonhardt, Science **312**, 1777 (2006)

[13] D. Schurig, J. J. Mock, B. J. Justice, S. A. Cummer, J. B. Pendry, A. F. Starr, and D. R. Smith, Science **314**, 977 (2006).

[14] V. M. Shalaev, Nature Photonics **1**, 41 (2007).

[15] M. O. Öktel and O. E. Müstecaplioglu, Phys. Rev. A **70**, 053806 (2004).

[16] Q. Thommen and P. Mandel, Phys. Rev. Lett. **96**, 053601 (2006).

[17] J. Kästel, M. Fleischhauer, S. F. Yelin, and R. L. Walsworth, Phys. Rev. Lett. **99**, 073602 (2007).

[18] P. P. Orth, J. Evers, and C. H. Keitel, arXiv:0711.0303 (2007).

[19] J. D. Jackson, *Classical Electrodynamics* (Wiley, New York, 1998).

[20] M. Fleischhauer, C. H. Keitel, M. O. Scully, C. Su, B. T. Ulrich, and S.-Y. Zhu, Phys. Rev. A **46**, 1468 (1992).

[21] B. Jungnitsch and J. Evers, arXiv:0804.3552 (submitted)

[22] J. B. Pendry, Science **306**, 1353 (2004).

[23] M. O. Scully and M. S. Zubairy, *Quantum Optics* (Cambridge University Press, Cambridge, 1997).

[24] Z. Ficek and S. Swain, *Quantum Interference: Theory and Experiments* (Springer, Berlin, 2005).

[25] M. G. Floquet, Ann. Sci. Ec. Normale Super. **12**, 47 (1883).

[26] R. Loudon, *The Quantum Theory of Light*, (Oxford University Press, Oxford, 2000).

[27] Yu. Ralchenko, A. E. Kramida, J. Reader, and NIST ASD Team (2008). *NIST Atomic Spectra Database* (version 3.1.5), [Online]. Available: http://physics.nist.gov/asd3 [2008, June 24]. National Institute of Standards and Technology, Gaithersburg, MD.

[28] S. J. Buckle, S. M. Barnett, P. L. Knight, M. A. Lauder, and D. T. Pegg, Opt. Acta **33**, 2473 (1986).

[29] D. V. Kosachiov, B. G. Matisov and Y. V. Rozhdestvensky, J. Phys. B **25**, 2473 (1992).

[30] W. E. van der Veer, R. J. J. van Diest, A. Dönszelmann, and H. B. van Linden van den Heuvell, Phys. Rev. Lett. **70**, 3243 (1993).

[31] S. A. Babin, S. I. Kablukov, U. Hinze, E. Tiemann, and B. Wellegehausen, Opt. Lett. **26**, 81 (2001).

[32] W. Maichen, F. Renzoni, I. Mazets, E. Korsunsky, and L. Windholz, Phys. Rev. A **53**, 3444 (1996).

[33] E. A. Korsunsky, N. Leinfellner, A. Huss, S. Baluschev, and L. Windholz, Phys. Rev. A **59**, 2302 (1999).

[34] E. A. Korsunsky and D. V. Kosachiov, Phys. Rev. A **60**, 4996 (1999).

[35] A. J. Merriam, S. J. Sharpe, M. Shverdin, D. Manuszak, G. Y. Yin, and S. E. Harris, Phys. Rev. Lett. **84**, 5308 (2000).

[36] G. Morigi, S. Franke-Arnold, and G.-L. Oppo, Phys. Rev. A **66**, 053409 (2002).

[37] S. Kajari-Schroder, G. Morigi, S. Franke-Arnold, and G.-L. Oppo, Physical Review A **75**, 013816 (2007).

[38] A. F. Huss, R. Lammegger, C. N aeureiter, E. A. Korsunsky, and L. Windholz, Phys. Rev. Lett. **93**, 223601 (2004).

[39] V. S. Malinovsky and I. R. Sola, Phys. Rev. Lett. **93**, 190502 (2004).

[40] H. Shpaisman, A. D. Wilson-Gordon, and H. Friedmann, Physical Review A **71**, 043812 (2005).

[41] M. Mahmoudi and J. Evers, Phys. Rev. A **74**, 063827 (2006).

[42] P. Kinsler and M. W. McCall, arXiv:0806.1676v1

[43] J. Skaar, Phys. Rev. E **73**, 026605 (2006)

[44] B. Nistad and J. Skaar, arXiv:0712.3132v1

[45] E. D. Solomentsev, "branch point", in *Encyclopedia of Mathematics* by M. Hazewinkel, 10 Vols. (Kluwer Academic Publishers, Dordrecht, 1995)

[46] D. S. Jones, *The Theory of Electromagnetism* (Pergamon Press, Oxford, 1964).

[47] G. Dolling, C. Enkrich, M. Wegener, C. M. Soukoulis, and S. Linden, Opt. Lett **31**, 1800 (2006).

Danksagungen

Ich möchte mich an dieser Stelle gerne bei allen Personen bedanken, die zum Gelingen dieser Diplomarbeit beigetragen haben, insbesondere bei

- Prof. Christoph H. Keitel für die freundliche, vertrauensvolle Aufnahme in seine Gruppe und die Möglichkeit, unter exzellenten Bedingungen am Max-Planck-Institut für Kernphysik arbeiten zu können, sowie für die Möglichkeit der Teilnahme an der DPG-Jahrestagung 2008 in Darmstadt.
- Dr. Jörg Evers für die hervorragende Betreuung, von dem ich in unzähligen, sehr hilfreichen Gesprächen und Diskussionen viel gelernt habe und dies sowohl in fachlicher als auch durch seine professionelle, exakte Arbeit in methodischer Hinsicht. Ich habe von ihm sehr viel Unterstützung erfahren in allem, was auch nur ansatzweise mit meiner Diplomarbeit verbunden war. Jederzeit konnte ich ihm Fragen stellen und fühlte mich durch seine freundliche Art sehr gut aufgehoben in seiner Untergruppe.
- Prof. Thomas Gasenzer, der freundlicherweise die Zweitkorrektur meiner Diplomarbeit übernahm.
- Peter Brunner, den ich stets mit Computerfragen löchern konnte.
- Robert Fleischhaker, der immer bereit war, mir Tipps zu geben.
- Raoul Heyne, der an Urlaubstagen das ein oder andere Mal Dinge für mich am Institut erledigte.
- Eike Nicklas und Carlus Deneke für das Korrekturlesen und die nützlichen Tipps.
- meinen Zimmernachbarn Erik Lötstedt, Luling Jin, Carlus Deneke, Atif Shahbaz, Qurrat-ul-Ain, Tim-Oliver Müller und Benedikt Wundt, die stets zu einer freundlichen und positiven Atmosphäre beitrugen.
- allen Arbeitskollegen, die die Arbeit hier am Institut so angenehm machten, insbesondere Ben King und Hossein Ebadi.

- allen meinen Freunden, die mir meine Studienzeit unvergesslich machten.
- Julia Hupfeld, die sehr verständnisvoll war und immer voll hinter mir stand.
- bei meinen Eltern Birgit und Siegfried Jungnitsch, die mich stets vorbehaltlos in jeglicher Hinsicht unterstützten.

Erklärung:

Ich versichere, dass ich diese Arbeit selbständig verfasst und keine anderen als die angegebenen Quellen und Hilfsmittel benutzt habe.

Heidelberg, den ....

Unterschrift